2014

I. Toward Non-blinking Robust Vis and NIR Active Fluorophores: Controlled Fabrication and Applications of Thick-Shell CdSe/nCdS and Ge/nCdS (n>10) Nanocrystals II. Shape-Programmed Nanofabrication: Understanding the Reactivity of Dichalcogenide Precursors

Yijun Guo
Iowa State University

I. Toward non-blinking robust Vis and NIR active fluorophores: Controlled fabrication and applications of thick-shell CdSe/nCdS and Ge/nCdS (n>10) nanocrystals
II. Shape-programmed nanofabrication: Understanding the reactivity of dichalcogenide precursors

by

Yijun Guo

A dissertation submitted to the graduate faculty

in partial fulfillment of the requirements for the degree of

DOCTOR OF PHILOSOPHY

Major: Chemistry

Program of Study Committee:
Javier Vela, Major Professor
Ning Fang
Gordon Miller
Keith Woo
Aaron Sadow

Iowa State University

Ames, Iowa

2014

DEDICATION

To my Dad, my Mom and my Grandmother

TABLE OF CONTENTS

ACKNOWLEDGEMENTS

I am very thankful for having a lot of mentors, advisors, and friends who were always willing to share advice with me throughout my five years of study at Iowa State University. First, I would like to thank my major advisor, Prof. Javier Vela. He took me into his group as one of his first graduate students at Iowa State. I thank him for his confidence in me. I consider myself very lucky to have had the opportunity of learning how to conduct experiments and operate instruments directly from him. Thanks for helping me start on my research project. Thanks for showing me how to be a good researcher. Thanks for giving me the opportunities to present my research at different conferences. It has been really enjoyable to work with him.

Next, I would like to thank my committee members, Dr. Ning Fang, Dr. Gordon Miller, Dr. Keith Woo, and Dr. Aaron Sadow, for their guidance and support throughout my years of study and research. I found Dr. Miller's solid-state chemistry class valuable for my research. Dr. Fang offered me thoughtful insight about my research and also my career path. I would like to thank Prof. Fang and Prof. Smith for giving me the opportunity to collaborate with their groups. I enjoyed working with researchers from different fields and I learnt a lot from them.

In addition, I would also like to thank my labmates, Dr. Purnima Ruberu, Elham Tavasoli, Chia-Cheng Lin, Malinda Reichert, Sam Alvarado, Michelle Thompson, Patrick Dilsaver, Long Men, Himashi Andaraarachchi and Dr. Feng Zhu. I enjoyed having scientific discussions with them as well as the fun times outside the lab. I would also like to thank the

many undergraduates who worked with me: Rachel Abraham, Ran Zhu, Joshua Barclay, and Cody Hancock. Without their hard work, my work would not have been completed as fast.

Finally, I would like to give special thanks to my parents and grandmother. They were very supportive when I started thinking about pursuing my PhD in a foreign country. Thanks for your support and love that helped me through the ups and downs during these years. Without it, I could not have come this far.

ABSTRACT

Core/shell colloidal semiconductor nanocrystals are one of the most active areas of nanotechnology research. CdSe/nCdS core/shell heterostructures show remarkable suppressed fluroscence intermittency at the single-particle level. Although syntheses of thin-shelled core/shells have been reported in the past, reproducible syntheses for thick-shelled core/shells are less understood. Moreover, most of the core/shell reports are on CdSe/nCdS heterostructures, while other core materials –such as Ge– are absent from the literature.

In the first part of this thesis, we present a thorough investigation of thick-shelled nanocrystal synthesis. We successfully grow metal sulfide shells on two different cores: CdSe and Ge. We explored the effect that the concentration of amine, amine type, core size, cadmium precursor concentration, annealing time, injection-rate and surface priming have on the synthesis of core/shell heterostructures. Adopting a similar method that uses surface priming, we are also able to grow epitaxial cadmium sulfide and zinc sulfide shells on Ge cores. The obtained Ge/nMS heterostructures show a large emission enhancement in the near-infrared range. We discuss the optical behavior of thick-shelled CdSe/nCdS nanocrystals at the ensemble and single-particle levels. Through collaboration with analytical research groups, we study the applications of these core/shell nanocrystals in bio-imaging and tracking using total internal reflection microscopy and stimulated emission depletion microscopy.

Beyond spherical or spheroidal nanocrystals, anisotropic nanostructures such as nanorods and tetrapods are of particular interest in photocatalysis and energy harvesting. Controlling the size and morphology of more ophisticated structures such as these remains

difficult. Dichalcogenide precursors enable the isolation of metastable nanocrystalline phases with unusual composition and morphology. It remains unclear what factors play a determinant role in controlling the outcome of preparations that utilize these interesting family of precursors.

In the second part of this thesis, by studying a variety of commercially available dichalcogenides and the outcome of their reaction, and with the help of computational calculations, we demonstrate that the formation and degree of anisotropy of different nanocrystaline products can be traced back to the precise molecular structure and reactivity of the precursor used. We expect our results will not only lead to a larger throughput of these materials, but also lead to reliable syntheses of colloidal nanomaterials for customized applications.

CHAPTER 1

INTRODUCTION

General introduction

This thesis consists of two parts:

Part I. Synthesis, characterization and application of stable, robust visible and near-infrared emitting core/shell semiconductor fluorophores.

Part II. Experimental studies on the effect that the chemical reactivity of dichalcogenide precursors have on the syntheses of colloidal metal chalcogenide nanomaterials with different shapes for customized applications.

Highly stable, robust quantum dot fluorophores typically consist of two parts: A semiconductor core, which mainly controls the photoluminescence emission range, and a very thick shell that has a wider band gap. We selected CdSe and Ge as core materials and CdS and ZnS as shell candidates. We explored different reaction parameters, such as addition of amine, amine type, cation and anion ratio, and discussed their effect on shell growth. We demonstrated that with the optimized reaction conditions, CdSe/CdS, Ge/CdS and Ge/ZnS heterostructures with desired shell thicknesses could be synthesized. By employing scanning-angle total internal reflection fluorescence microscopy and stimulated emission depletion microscopy, we showed that the obtained core/shell quantum dots showed unique optical properties and were very useful for biological imaging and tracking.

Dialkyl dichalcogenide (R-E-E-R) precursors are highly versatile molecular precursors that are commonly used in colloidal metal chalcogenide synthesis. It is well known that the use of dialkyl dichalcogenide precursors can yield unusual compositions and morphologies. Unfortunately, it remains unclear what factors play a determining role in

controlling particle size, composition or morphology. Using a standard set of otherwise identical, optimized reaction conditions, we study the relationship between the reactivity of the dichalcogenide precursor and the anisotropy of the resulting nanostructures. We demonstrate that the formation and degree of anisotropy of different nanocrystalline products can be traced back to the precise molecular structure, bond dissociation energy and chemical reactivity of different molecular precursors used.

Semiconductor nanocrystals and their unique optical properties: Size, composition and shape-dependence

Semiconductor nanocrystals made of ZnS, CdS, CdSe, CdTe, PbSe, Ge, InAs, and HgSe have strong absorption extinction coefficients (cross sections, $\varepsilon \approx 10^5$-10^6 $M^{-1} \cdot cm^{-1}$),[1] narrow photoluminescence ranges ($\leq$ 25 nm), and size- and composition tunable band gaps (250-4000 nm).[2,3] Due to these attractive optical and electronic properties, semiconductor nanocrystals are ideal candidates for a variety of applications, such as bio-imaging,[4] bio-labeling,[5] photoelectronics,[6] photocatalysis,[7,8] and photovoltacis[9]. Colloidal semiconductor nanocrystals have an inorganic core surrounded by an insulating shell made of organic surfactants or polymers. This unique inorganic/organic hybrid structure not only provides colloidal stability, but also imparts greated stability against photobleaching and photo or chemical degradation compared to more traditional organic fluorophores.[10,11]

The electronic and optical properties of semiconductor nanocrystals are closely related to their size, morphology and composition. For example, thick-shelled CdSe/nCdS core/shell structures showed dramatically suppressed blinking at the single particle level.[12] Because of their ability of these materials to form and stabilize multiple electron-hole pairs,

anisotropic nanocrystals having nanorod and tetrapod shape are particularly interesting in solar energy harvesting and photocatalysis.[13,14] Being able to control a semiconductor nanocrystal's size, morphology and composition has long been a dream of synthetic chemists.

Quantum dot blinking

Semiconductor quantum dots have intrinsic fluorescence properties that hold advantages over organic fluorescent dyes such as broad absorption and narrow emission spectra and imcreased photo and chemical stability. Despite these advantages, the application of quantum dots in bioimaging and tracking has been limited by their single particle fluorescent intermittency, also called "blinking" behavior.[15] While a full explanation for blinking behavior has still to emerge,the most commonly accepted theory is that single particle fluorescent intermittency occurse due to the creation of dark (non-emissive), charged quantum dot states under continuous illumination (excitation).

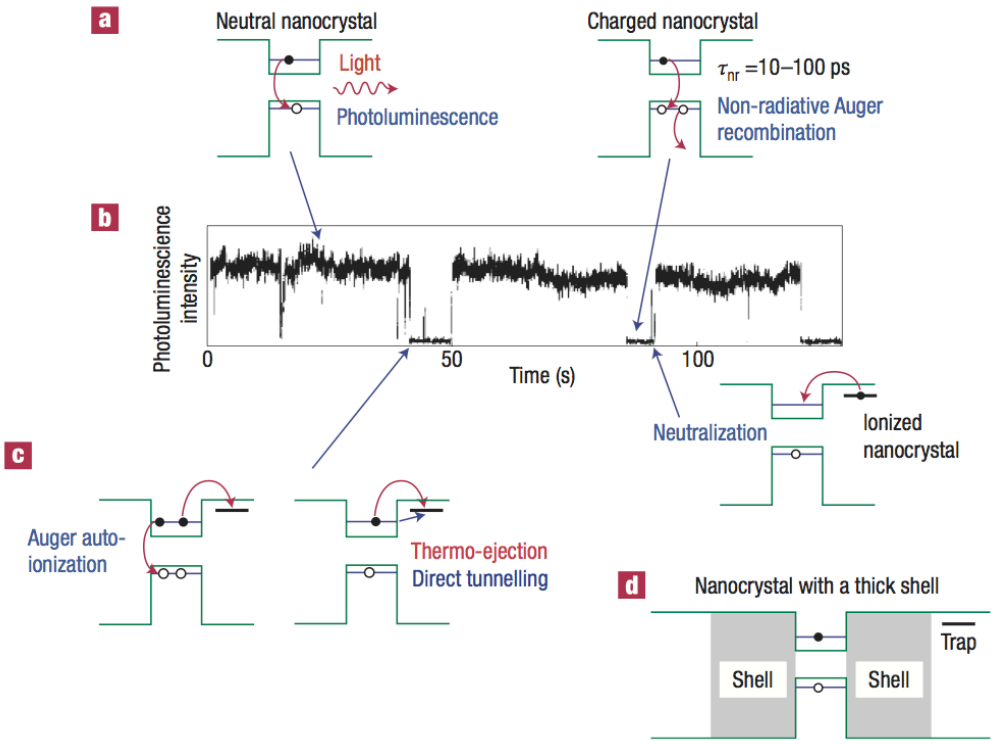

Figure 1. Random blinking of colloidal nanocrystals. a, Schematic diagram of neutral and charged nanocrystals. Optical excitation of the neutral nanocrystal leads to photoluminescence; excitation of the charged nanocrystal leads to fast non-radiative Auger recombination with decay time on the order of 10 – 100 ps. b, Typical fluorescence trajectory measured in a single CdSe nanocrystal of 2.1 nm radius. c, Processes leading to nanocrystal ionization and neutralization. d, Nanocrystal with a thick shell. Copyright 2008 Macmillan Publishers.

Under standard conditions, a neutral quantum dot absorbs a photon to generate an electron-hole pair, which later recombines to eject another photon, giving rise to photoluminescence (Figure 1). However, if the particle is charged, this triggers another nonradiative decay process called Auger recombination. This process is orders of magnitude faster compared to the radiative decay mentioned previously, resulting in complete photoluminescence quenching in charged nanocrystals.[16]

Two main approaches to blinking suppression

Many research groups have attempted to answer how particles get charged, how electrons get trapped, where electrons end up, and when and how electrons return to their ground state energy levels.[17,18] Related to quantum blinking, the practical question being asked most often is if this blinking behavior can be suppressed or even be completely eliminated.[19]

Since the consensus is that blinking occurs when particles get charged, the first approach is to suppress quantum dot ionization. Hohng, S. *et al.* reported binding of thiol ligands to quantum dot surface.[20] Due to their weakly basic nature, thiols can serve as a charge mediator or a charge compensator, donating electrons to surface electron traps, which renders them incapable of accepting electrons from the dot, hence suppressing blinking. However, this method has limitations. Due to highly reversible thiol binding, blinking resumes once excess thiol ligands are removed.

Another approach reported by Mahler *et al.* and Chen *et al.* is to form an inorganic insulating barrier, normally another semiconductor that has a wider band gap, around the cores.[12,21] In contrast to the first approach, this approach fully isolates the wave function of the quantum dot core from the quantum dot surface and the surface environment, creating a fundamentally unique epitaxial quantum dot system. Both groups saw irreversible blinking suppression upon metal sulfide shell growth on the quantum dot cores. The exact role of metal sulfide shell and the precise blinking suppression mechanism remain unknown.

Giant core/shell CdSe/nCdS quantum dots

Recently, Mahler *et al.* and Chen *et al.* reported thick-shell CdSe/nCdS (n>10) core/shell that showed unparalleled chemical robustness, photostability and significant modified blinking behavior.[12,21] Ever since, the blinking suppression mechanism and photophysics of these materials have attracted a lot of attention.

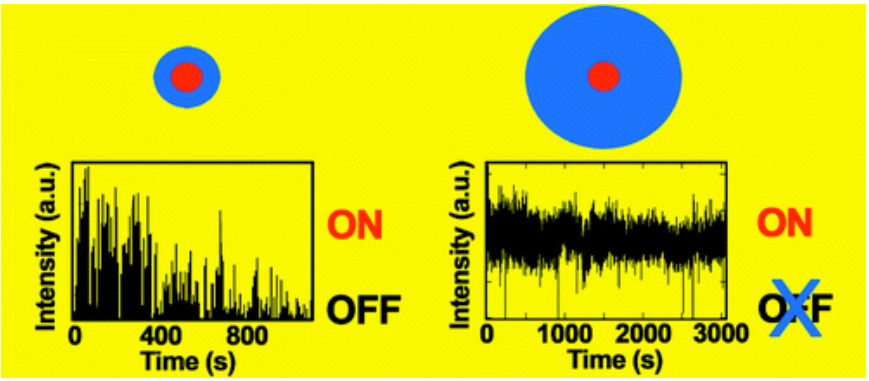

Figure 2. Blinking suppression with giant core/shell system. Copyright 2010 American Chemical Society.

These results were quickly expanded to other similar systems. CdSe/nCdS quantum dots with more than ten CdS monolayers showed nearly complete blinking suppression on milliseconds-to-minutes timescales.[22] Ternary CdZnSe/ZnSe core/shell quantum dots with thin shells also showed non-blinking behavior. It was suggested that the CdZnSe/ZnSe core/shell quantum dot has a radial composition gradient where CdZnSe changes into ZnSe. Unfortunately, detailed synthesis and structural characterization of these quantum dots were not reported.[23] We carried out a thorough investigation of thick-shelled CdSe/nCdS nanocrystal synthesis using short and accessible 15 min wait times between each precursor injection. We found that added secondary amine and low-core and precursor concentrations introduced at slow injection rates result in core/shells with desired shell thickness.

Near-IR emitting Ge quantum dots as a new type of fluorophore

Ideally, non-blinking quantum dots are chemically robust and stable under aqueous and aerobic conditions. They must also be active in a region that is useful to the imaging of relevant biological media, and where tissue and solutes are most transparent to optical excitation and fluorescence signals. In animals,this biological transparency window is 700 nm to 1200 nm. Best suited for this purpose are semiconductors with small band gaps (700 nm ≤ band gap ≤ 1200 nm). Unfortunately, two of the most commonly studied near-infrared (NIR) active QD materials, InP[24] and CdTe[25,26], are "soft" and chemically labile or unstable, even after the deposition of shells.[27,28] Such chemical instability severely hinders a systematic synthetic exploration of their core/shell chemistry, especially for cases where a very thick shell may be necessary, and makes the development of non-blinking QDs based on these materials very challenging.

Elemental germanium is very attractive as a core material for the synthesis of NIR emitting fluorophores.[29,30,31] Similar to elemental silicon, Ge is a relatively earth-abundant and robust material that has relatively low toxicity compared to heavy metal-based (Cd, Pb, As) semiconductors.[32] More importantly, compared to Si, Ge has a direct band gap and a strong absorption coefficient (large cross section or extinction coeffcient).[33] Thus, Ge is an ideal candidate for the development of highly biocompatible, NIR-emitting QDs. In this thesis, we discuss the synthesis of Ge/nCdS and Ge/nZnS core/shell structures with enhanced NIR photoluminescence.

Anisotropic semiconductor nanocrystals: Nanorods, tetrapods

Anisotropic semiconductor nanocrystals such as nanorods, tetrapods, nanotubes have great potential in photocatalysis,[7,8] photovoltaics[9] and other optoelectronic devices.[4,5,6] Understanding the atomic level nucleation and growth of these one-dimensional structures will lead to predictable, controllable anisotropic nanocrystal synthesis.

Molecular beam epitaxy[34] and metal-organic chemical vapor deposition[35] have been exploited to generate anisotropic nanocrystals. Commonly used synthetic routes toward colloidal anisotropic structures are extremely sensitive to reaction parameters such as reaction time, reaction temperature, precursor concentration, and ligand type and chain length. For nanorods, specific surface ligands – such as phosphonic acid – which have different binding affinity towards different semiconductor facets are essential.[36,37] For tetrapods, an even more complex system, seeded growth is usually required. Semiconductor nanoseeds are first synthesized and then introduced into another system which contains cation and anion precursors.[38,39] The original semiconductor seed then guides the growth direction, forming anisotropic nanostructures.

Using dichalcogenide precursors (R-E-E-R) can sometimes yield nanocrystals with unusual compositions and morphologies.[40,41,42] Two distinctively reactive C-E and E-E bonds makes the chemistry of these precursors even richer and more interesting than the commonly used phosphine chalcogenides. This part of the thesis explores using different dichalcogenides or a mixture of two different dichalcogenide precursors, without using any seeds or size-selection wash, to control the size and morphology of semiconductor nanocrystals.

Thesis organization

This thesis is comprised of two parts: Part I. Synthesis of II-VI and IV-VI core/shell semiconductors and investigation of their application on imaging; Part II. Experimentally study the reactivity of dichalcogenide precursors. Chapters 2, 3, and 5 contain material that has already been published, while Chapter 4 is submitted and under review at the time of writing. As the thesis covers a diverse range of topics from semiconductor synthesis to application, relevant literature is provided in the introduction to each chapter.

Chapter 2 describes the synthesis of CdSe/nCdS core/shell heterostructure nanoparticles. Chapter 3 describes using non-blinking quantum dot for imaging purpose via total internal reflection microscopy and stimulated emission depletion microscopy. This was done in collaboration with Prof. Fang, Prof. Smith and Prof. Petrich and their groups at Iowa State University. Chapter 4 focuses on the synthesis of Ge/nCdS, Ge/nZnS core/shell heterostructures and their enhanced photoluminescence properties. Chapter 5 is dedicated to the study of dichalcogenide precursors and how reactivity affects nanocrystal size and morphology. Another member of the Vela group, Mr. Samuel R. Alvarado performed all the DFT calculations used to determine bond dissociation energies, bond lengths and dihedral angles of the different dichalcogenide precursors.

References

[1] Kuno, M. *Phys. Chem. Chem. Phys.* **2008**, *10*, 620-639.

[2] Hochbaum, A. I.; Yang, P. *Chem. Rev.* **2010**, *110*, 527-546.

[3] Talapin, D. V.; Lee, J.-S.; Kovalenko, M. V.; Shevchenko, E. V. *Chem. Rev.* **2010**, *110*, 389-458.

[4] Bruchez, M.; Moronne, M.; Gin, P.; Weiss, S.; Alivisatos, A. P. *Science* **1998**, *281*, 2013−2016.

[5] Chan, W. C. W.; Nie, S. M. *Science* **1998**, *281*, 2016−2018.

[6] Klimov, V. I.; Ivanov, S. A.; Nanda, J.; Achermann, M.; Bezel, I.; McGuire, J. A.; Piryatinski, A. *Nature* **2007**, *447*, 441−446.

[7] W. A. Tisdale, K. J. Williams, B. A. Timp, D. J. Norris, E. S. Aydil and X.-Y. Zhu, *Science*, **2010**, *328*, 1543–1547.

[8] J. B. Sambur, T. Novet and B. A. Parkinson, *Science*, **2010**, *330*, 63–66.

[9] Schlamp, M. C.; Peng, X. G.; Alivisatos, A. P. *J. Appl. Phys.* **1997**, *82*, 5837−5842.

[10] Smith, A. M.; Nie, S. M.; *Acc. Chem. Res.* **2010**, *43*, 190-200.

[11] Park, J.; Joo, J.; Kwon, S. G.; Jang, Y.; Hyeon, T. *Angew. Chem., Int. Ed.* **2007**, *46*, 2-33.

[12] Chen, Y.; Vela, J.; Htoon, H.; Casson, J. L.; Werder, D. J.; Bussian, D. A.; Klimov, V. I.; Hollingsworth, J. A. *J. Am. Chem. Soc.* **2008**, *130*, 5026–5027.

[13] Nozik, A. *J. Chem. Phys. Lett.* **2008**, *457*, 3-11.

[14] Klimov, V. I. *J. Phys. Chem. B* **2006**,*110*,16827-16845.

[15] Nirmal, M.; Dabbousi, B. O.; Bawendi, M. G.; Malklin, J. J.; Trautman, J. K.; Harris, T. D.; Brus, L. E. *Nature*, **1996**, *383*, 802-804.

[16] Efros, A. L. *Nat. Mater.* **2008**, *7*, 612-613.

[17] Spinicelli, P.; Buil, S.; Quélin, X.; Mahler, B.; Dubertret, B.; Hermier, J.-P. *Phys. Rev. Lett.* **2009**, *102*, 136801-1–136801-4.

[18] Brovelli, S.; Schaller, R. D.; Crooker, S. A.; García-Santamaría, F.; Chen, Y.; Viswanatha, R.; Hollingsworth, J. A.; Htoon, H.; Klimov, V. I. *Nature Commun.* **2011**, *2*, 1-8.

[19] García-Santamaría; Brovelli, S.; Viswanatha, R.; Hollingsworth, J. A.; Htoon, H.; Scott A. Crooker; Klimov, V. I. *Nano Lett.* **2011**, *11*, 687-693.

[20] Hohng, S. Ha, T. *J. Am. Chem. Soc.* **2004**, *126*, 1324.

[21] Mahler, B.; Spinicelli, P.; Buil, S.; Quelin, X.; Heimier, J. P.; Dubertret, B. *Nat. Mater.* **2008**, *7*, 659-664.

[22] Vela, J.; Htoon, H.; Chen, Y.; Park, Y.-S.; Ghosh, Y.; Goodwin, P.; Werner, J.; Wells, N. P.; Casson, J. L.; Hollingsworth, J. A. *J. Biophoton.* **2010**, *3*, 706-717.

[23] Wang, X.; Ren, X.; Kahen, K.; Hahn1, M. A.; Rajeswaran, M.; Maccagnano-Zacher, S.; Silcox, J.; Cragg, G. E.; Efros, A. L.; Krauss, T. D. *Nature* **2009**, *459*, 686-689.

[24] Xie, R.; Battaglia, D.; Peng, X. *J. Am. Chem. Soc.* **2007**, *129*, 15432-15433.

[25] Gaponik, N.; Talapin, D. V.; Rogach, A. L.; Hoppe, K.; Shevchenko, E. V.; Kornowski, A.; Eychmuller, A.; Weller, H. *J. Phys. Chem. B* **2002**, *106*, 7177-7185.

[26] Wuister, S. F.; Swart, I.; van Driel, F.; Hickey, S. G.; Donega, C. M.; *Nano Lett.* **2003**, *3*, 503-507.

[27] Jasinskia, J.; Lepperta, V. J.; Lamb, S.-T.; Gibsonb, G. A.; Naukab, K.; Yangb, C. C.; Zhou, Z.-L. *Solid State Commun.* **2007**, *141*, 624-627.

[28] Cao, Y. W.; Banin, U. *J. Am. Chem. Soc.* **2000**, *122*, 9692–9702.

[29] Lee, D. C.; Pietryga, J. M.; Robel, I.; Werder, D. J.; Schaller, R. D.; Klimov, V. I. *J. Am. Chem. Soc.* **2009**, *131*, 3436–3437.

[30] Henderson, E. J.; Hessel, C. M.; Veinot, J. G. C. *J. Am. Chem. Soc.* **2008**, *130*, 3624-3632.

[31] Ruddy, D. A.; Johnson, J. C.; Smith, E. R.; Neale, N. R. *ACS Nano*, **2010**, *4*, 7459-7466.

[32] Lewinski, N.; Colvin, V. *Small* **2008**, *4*, 26-49.

[33] Veinot, J. G. C. *Chem. Commun.* **2006**, 4160-4168.

[34] Fuhrmann, B.; Leipner, H. S.; Höche , H.-R. *Nano Lett.* **2005**, *5*, 2524-2527.

[35] Omstead, T. R.; Jensen, K. F. *Chem. Mater.* **1990**, *2*, 39-49.

[36] Peng, X.; Manna, L.; Yang, W.; Wickham, J.; Scher, E.; Kadavanich, A.; Alivisatos, A. P. *Nature* **2000**, *404*, 59-61.

[37] Peng, Z. A.; Peng, X. *J. Am. Chem. Soc.* **2002**, *124*, 3343−3353.

[38] Kumar, S.; Nann, T. *Small*, **2006**, *2*, 316–329.

[39] Fiore, A.; Mastria, R.; Lupo, M. G.; Lanzani, G.; Giannini, C.; Carlino, E.; Morello, G.; De Giorgi, M.; Li, Y.; Cingolani, R.; Manna, L. *J. Am. Chem. Soc.* **2009**, *131*, 2274−2282.

[40] Norako, M. E.; Brutchey, R. L. *Chem. Mater.* **2010**, *22*, 1613–1615.

[41] Franzman, M. A.; Brutchey, R. L. *Chem. Mater.* **2009**, *21*, 1790–1792.

[42] Norako, M. E.; Greaney, M. J.; Brutchey, R. L. *J. Am. Chem. Soc.* **2012**, *134*, 23–26.

CHAPTER 2

UNIQUE CHALLGENS ACCOMPANY THICK-SHELL CdSe/NCdS (N>10) NANOCRYSTAL SYNTHESIS

Reprinted with permission from *J. Phys. Chem. C.*, **2012**, *116*, 2791.

Yijun Guo, Kyle Marchuk, Siddharth Sampat, Rachel Abraham, Ning Fang, Anton V. Malko, Javier Vela

Abstract

Core/shell semiconductor nanocrystals are one of the most active areas of nanotechnology research. In a core/shell, two or more semiconductors can be manipulated to produce unique optoelectronic properties. Thick-shell CdSe/nCdS (n≥10) nanocrystals were recently reported to show remarkably suppressed fluorescence intermittency or 'blinking' at the single particle level and slow rates of Auger decay. Unfortunately, while the synthesis of CdSe/nCdS nanocrystals is well developed up to n≤6 CdS monolayers (MLs), reliable syntheses of CdSe/nCdS nanocrystals with n≥10 MLs are lacking. Currently available procedures lead to homogeneous nucleation of CdS instead of heterogeneous nucleation of CdS epitaxially on CdSe, resulting in broad and multi-modal particle size distributions. Critically, the obtained core/shell sizes are well below those desired. In this paper, we investigate synthetic conditions specific to growth of such thick-shell materials (n≥10 and n≥20 MLs). We first use primary amine and excess cadmium precursor and show that these do not result in desired core/shell sizes. In contrast, added secondary amine and low concentration of CdSe cores and molecular precursors result in desired core/shell sizes. We observe that amine-induced partial etching of CdSe cores results in apparent shell thicknesses

that are slightly beyond those desired, especially for very thick shells (n≥20 MLs). We also explore the effect that thermal ripening and precursor injection rate have on the synthesis of these materials and present structural and optical characterization. We expect our new synthetic approach will lead to a larger throughput of these materials, increasing their availability for fundamental study and application.

Introduction

Core/shell colloidal semiconductor nanocrystals are one of the most active areas of nanotechnology research.[1,2] Semiconductor nanocrystals are among the best chromophores and fluorophores available thanks to their broad and intense absorption profile ($\varepsilon \approx 10^5$-10^6 $M^{-1}\cdot cm^{-1}$),[3-5] size- and composition-tunable band-gap (250-4000 nm), narrow (≤ 25 nm) and long-lived emission bands (20 ns CdSe,[6] 1 μs PbSe[7]) and high photo- and chemical-stability.[8-15] Colloidal semiconductor nanocrystals have the advantage of having a coating layer of ligands which makes them amenable to surface modification, as well as being readily dispersable in organic and aqueous solvents. In a core/shell architecture, two or more semiconductors can be manipulated to obtain improved or unique optoelectronic properties. Relative band alignment between materials comprising the core/shell can be used to confine the electron and hole wave functions together to the core in a 'type-I' configuration or independently from each other to core and shell in a 'type-II' configuration.[16-17] The pressure, or 'strain', exerted by the shell can also be used to tune the core's conduction band energy level.[18] The resulting degree of electron-hole overlap determines the photoluminescence (PL) and Auger exciton decay rates.[19-21]

For cadmium chalcogenides, early core/shell preparations relied on reaction between cores and organometallic shell precursors,[22-29] single-source precursors (SSPs),[30-31] or photodegradation of surface ligands.[32] Successive Ion Layer Adsorption and Reaction (SILAR), originally developed for thin-films, has become the method of choice to prepare core/shell and multishell nanocrystals.[33-39] Thermal Cycling-Single Precursor (TC-SP) has lead to core/shells with narrower size dispersions and better color purity.[40-41] Other approaches that can facilitate core/shell formation include minimizing the core-shell lattice mismatch, reducing stress-induced defects through grading,[42-43] and using chemical compatibility to build core/shells around structurally disparate materials.[44]

Very recently, thick-shell CdSe/nCdS ($n \geq 10$) core/shell nanocrystals were reported that showed remarkably suppressed fluorescence intermittency or 'blinking' at the single particle level.[45-46] This has spurred a wave of studies into the blinking suppression mechanism and photophysics of these materials.[4,47-51] Among questions that remain unanswered is whether the size of the CdSe core[52] as well as the nature of the core-shell interface (abrupt vs. graded)[53] play a role in determining the unique optical properties of these materials. These questions are of particular relevance and timeliness because radially graded alloy CdZnSe/ZnSe nanocrystals have been reported to display non-blinking behavior.[54]

To address these questions, reliable and reproducible syntheses are needed. Crystalline CdSe and CdS both exist in cubic (zinc blende) or hexagonal (wurtzite) form and their lattice mismatch is only 3.7% (zinc blende-zinc blende) or 3.9% (wurtzite-wurtzite). The synthesis of CdSe/nCdS nanocrystals is well developed up to a shell thickness of about six ($n \leq 6$) monolayers (MLs).[55] But only recently have there been reports on growth of ten

($n \leq 10$)[54] or more ($n \geq 10$) MLs.[57] Synthesizing such thick shell materials involves unique technical challenges. We have observed that large amounts of unreacted precursors after several SILAR injections lead to CdS homonucleation instead of heterogeneous nucleation epitaxially on CdSe, resulting in poor, broad, and multi-modal size distributions. Core/shell sizes obtained using available procedures are well below those desired.

Appearance of CdS homonuclei during growth of CdSe/CdS nanocrystals is difficult to detect by absorption and photoluminescence (PL) spectroscopies. Free CdS homonuclei and CdS shells share similar absorption features. Additionally, energy transfer from larger band gap CdS homonuclei to smaller band gap CdSe/CdS materials can render the former 'silent' by PL. Even more difficult to detect is presence of unreacted Cd and S precursors since they are spectroscopically silent except at bluer wavelengths (higher energies) than those where nanocrystals absorb. In this paper, we present a thorough investigation of CdSe/nCdS nanocrystals synthesis using the SILAR method, emphasizing growth of very thick CdS shells ($n \geq 10$ and even $n \geq 20$ MLs). We start by growing thick CdS shells on small, sub-2nm CdSe cores, selected as a test bed on the basis of their relative instability and propensity to dissolve at high temperature, and then extend the method to large, ca. 4.7 nm, CdSe cores. We present several control experiments to probe and document specific challenges associated with the synthesis of these materials including the effect that added primary and secondary amines and core and precursor concentration have on CdS homogeneous versus heterogeneous nucleation, ripening, and CdSe core etching.

Experimental Section

Materials. Cadmium oxide (CdO, 99.998%), sulfur (S_8, 99.999%), trioctylphosphine (TOP, 90%), and oleic acid (90%) were purchased from Alfa Aesar; selenium (Se, pellets, ≥99.999%), octadecyl amine (octadecyl-NH_2) (90%), and di-octylamine (98%) ((octyl)$_2$NH) from Sigma-Aldrich; 1-octadecene (ODE) (90%) and oleylamine (oleyl-NH_2) (80-90%) from Acros. Bis(2,2,4-trimethylpentyl)phosphinic acid (TMPPA) (CYANEX 272) was obtained from Cytec Industries, Inc. Procedures were performed under dry inert gas atmosphere (N_2 or Ar) in a glove box or a Schlenk line.

CdSe cores. *Small cores.* We synthesized small, sub-2nm, CdSe cores using a slightly modified literature procedure.[58]

0.16M TOPSe/ODE. Se (71.4 mg, 904 μmol), TOP (577 mg, 1.56 mmol), and ODE (4.00 g, 15.84 mmol) were stirred and heated until the mixture became optically clear.

Synthesis. CdO (15.0 mg, 117 μmol), TMPPA (304 mg, 1.05 mmol), and ODE (4.00 g, 15.84 mmol) were weighed in a 250 mL round bottom (R.B.) flask. The mixture was degassed under vacuum for 30 min at 80°C, refilled with Ar, and heated to 300°C for 6 hours until it became optically clear. The solution was heated to 325°C and 0.16M TOPSe/ODE (5.7 mL, 904 μmol) swiftly injected into the reaction flask. ~5 s after injection, the mixture was allowed to cool to room temperature (R.T.). This procedure reliably produced CdSe cores with a first absorption peak (1S) centered between 480-496 nm (in five runs: 480, 480, 496, 490, 485 & 488 nm).

Large cores. We synthesized large, ca. 4.7 nm, CdSe cores using a slightly modified literature procedure.[59]

2.1M TOPSe. Se (144 mg, 1.82 mmol) and TOP (797 mg, 2.15 mmol) were stirred and heated until the mixture became optically clear.

0.2M $Cd(oleate)_2$. CdO (318 mg, 2.48 mmol), oleic acid (3.09 g, 10.94 mmol), and ODE (7.11 g, 28.16 mmol) were placed in a R.B. flask, degassed under vacuum for 60 min at 80°C then refilled with Ar and heated to 240°C until the mixture become optically clear. Oleyl-NH_2 synthesis. Oleyl-NH_2 (5 mL, 15.14 mmol) was added to a R.B. flask, degassed under vacuum for 30 min at 80°C, then refilled with Ar.

Synthesis. Oleyl-NH_2 (5 mL, 15.14 mmol) or $(octyl)_2NH$ (5 mL, 16.55 mmol) was degassed under vacuum at 80°C for 30 min, then refilled with Ar. We added 2.1 M TOPSe (0.15 mL, 315 μmol), and the temperature increased to 300°C. After 5 min, 0.2 M $Cd(oleate)_2$ (1.5 mL, 300 μmol) was quickly injected, and the temperature adjusted to 280°C. Aliquots (<0.05 mL) were taken at different times analyzed by absorption and PL. After 10 min, the mixture was allowed to cool to RT.

Core purification. All CdSe cores were washed twice just prior to shell growth by precipitation with a 4:1v/v acetone-methanol mix. and centrifugation at 4,200 rpm for 10 min.

CdSe/nCdS core/shells. Precursors. 0.2M $Cd(oleate)_2$. This was prepared as described above for the synthesis of large CdSe cores. 0.2M $Cd(oleate)_2$-oleyl-NH_2. In a R.B. flask, CdO (640 mg, 4.98 mmol), oleic acid (6.18 g, 21.88 mmol) and ODE (4.39 g, 17.41 mmol) were degassed under vacuum for 60 min at 80°C then refilled with Ar and heated to 240°C until the mixture become optically clear. Freshly degassed oleyl-NH_2 (12.5 mL, 37.85 mmol) was added via syringe. The mixture was stirred at 60°C for 20 min. 0.1M $Cd(oleate)_2$-oleyl-NH_2. In a R.B. flask, oleyl-NH_2 (12.5 mL, 37.85 mmol) was degassed under vacuum for 30

min at 80°C. The amine was refilled with Ar and transferred via syringe into another R.B. flask containing 0.2M $Cd(oleate)_2$ (12.5 mL). The mixture was stirred at 60°C for 20 min. 0.1M $Cd(oleate)_2$-$(octyl)_2NH$. The procedure described above was repeated substituting the amine with $(octyl)_2NH$ (12.5 mL, 41.36 mmol).

0.2M S_8. S_8 (159 mg, 4.97 mmol) and ODE (19.73 g, 78.13 mmol) were degassed under vacuum for 30 min at 80°C then refilled with Ar and heated to 180°C. After 20 min, the mixture became optically clear and was allowed to cool to R.T. 0.1M S_8. S_8 (79.0 mg, 2.47 mmol) and ODE (19.73 g, 78.13 mmol) were degassed under vacuum for 30 min at 80°C then refilled with Ar and heated to 180°C. After 20 min, the mixture became optically clear and was allowed to cool to R.T.

Core solutions. Freshly made and washed CdSe cores (≤ 12 h) were dissolved in hexane (5 mL) (small, sub-2 nm cores) or toluene (5 mL) (large, ca. 4.5 nm cores). CdSe concentration was determined from the 1S peak using literature extinction coefficient data.3 Shell growth. An aliquot containing 1.5×10^{-7} mol for 19 μM initial concentration, or 7.5×10^{-8} mol of CdSe nanocrystals for 10 μM initial concentration, was transferred into a R.B. flask. The solvent was removed under vacuum at R.T. and ODE (4 mL, 12.5 mmol) and amine (3.001 g octadecyl-NH_2, 11.13 mmol; or 3.7 mL oleyl-NH_2, 11.20 mmol; or 3.8 mL $(octyl)_2NH$, 12.57 mmol) were added. The mixture was degassed under vacuum for 30 min at 80°C, refilled with Ar, and heated to the initial shell growth temperature. For small CdSe(1.9 nm) cores, growth temperature was 200°C for the first 1-2 MLs, 230°C between 3-6 MLs, and 240°C for >6 MLs.[53] For large CdSe(4.7 nm) cores, growth temperature was 235°C for the first 1-2 MLs and 245°C for >2 MLs.[53] Cd and S precursors were introduced in an alternating fashion using two programmable syringe pumps, each followed by a 15 min wait

period.[31] The Cd precursor was injected first. Shell growth was monitored by absorption and/or TEM by taking aliquots (≤ 0.05 mL) every other CdS theoretical monolayer (ML) starting at 4 MLs. The mixture was allowed to cool to R.T. 15 min after the last S injection.

Core/shell purification. Core/shells were washed three times by precipitation with a 1:1v/v acetone-methanol mixture and centrifugation at 4,200 rpm for 10 min.

Structural Characterization. *X-Ray Diffraction.* Powder X-ray diffraction (XRD) data were measured using Cu-Kα radiation on a Scintag XDS-2000 diffractometer.

Transmission Electron Microscopy. TEM of samples was conducted on carbon-coated copper grids using a FEI Technai G2 F20 Field Emission scanning transmission electron microscope (STEM) at 200 kV (point-to-point resolution <0.25 nm, line-to-line resolution <0.10 nm). Elemental composition was characterized by energy dispersive spectroscopy (EDS).

Particle analysis. Dimensions were measured manually and/or with ImageJ. Particle sizes were obtained for >50-100 particles. Average sizes are reported with ±standard deviations.

Optical characterization. *Ensembles.* Absorption spectra were measured with a photodiode array Agilent 8453 UV-Vis spectrophotometer. Solvent absorption was subtracted from all spectra. Steady state PL spectra were measured with a Horiba-Jobin Yvon Nanolog scanning spectrofluorometer with a photomultiplier detector. PL quantum yields (QYs) were measured following reported procedures.[46,61,62] Absorption and PL emission spectra of all samples were measured at least twice and the average QY was recorded.

Single particles. PL lifetimes. Nanocrystals were dispersed onto a quartz substrate from dilute hexane solution to a surface density of ~0.01/μm2. Samples were mounted on an

optical microscope translation stage and excited at 405 nm with 50 ps pulses through a 60×, 1.2 NA water immersion objective lens (Olympus), used to collect PL. The pulse-to-pulse separation (100-200 ns) was set much longer than PL decay to ensure complete exciton relaxation between laser pulses. PL was sent to a Perkin-Elmer avalanche photodiode (SPCM AQR-14) through a long-pass excitation/emission filter that rejected scattered laser light. Single photon counting was performed using PicoQuant Time Harp200 correlation hardware. Overall system's time resolution was 400 ps.

Blinking. Blinking statistics were collected on a prism-based total internal reflection fluorescence microscope (TIRFM).[63] Samples were excited with a 10 mW 488-nm argon continuous wave (CW) laser (Uniphase, San Jose, CA) and their PL filtered with a long pass 488 RazorEdge filter (Rochester, NY) and collected on an Andor iXon^{EM}+ 897 camera (Belfast; 512 x 512 imaging array, 16 μm x 16 μm pixel size). Exposure time was 50 ms with 100 gain in frame transfer mode. Nanocrystals were diluted in toluene. A 6 μL volume was deposited on a 22 mm^2 coverslip (Corning, NY) and immediately covered by a 18 mm^2 coverslip. Toluene was allowed to evaporate. The sample was then placed into the TIRFM and allowed to settle for 30 min to reduce sample drift during data acquisition. A total of 6000 frames (5 min) were collected per viewing area. ImageJ was used for background subtraction and recording of individual traces. Regions of interest (ROIs) around optically resolved nanocrystals were defined manually using the time series analyzer plugin. PL intermittency frequency and temporal length were derived for each individual nanocrystal.

Results and Discussion

In a typical CdSe/CdS core/shell growth experiment, enough Cd and S precursors are added to grow a CdS shell of a desired thickness, expressed as the theoretical or "calculated" number of CdS MLs. Assuming complete (100%) precursor conversions, the calculated core/shell particle size (diameter) is then compared with the experimentally "observed" particle size (diameter), commonly measured by TEM. The method of choice for CdSe/CdS core/shell growth uses SILAR conditions with cadmium-oleate ($Cd(oleate)_2$) and elemental sulfur (S_8) precursors and 1-octadecene (ODE) solvent.[45,46,55-57] Some reports use 60-180 min (3 h Cd, 1 h S, 4 h/ML),[46,57] and others use 10-15 min[45,55,56] annealing or "wait" times between injections. Long times may help ripen undesired CdS homonuclei, dissolving them in favor of heterogeneous epitaxial nucleation atop existing CdSe/CdS core/shells (Scheme 1a-c). However, long wait times result in 40 (1.7 days) and 80 h (3.3 days) to grow 10 and 20 CdS MLs, respectively. These long reaction times increase the odds that impurities (air, moisture) could affect shell growth. Short annealing times are more appealing to synthetic chemists, provided new synthetic conditions are found to increase the speed of ripening.

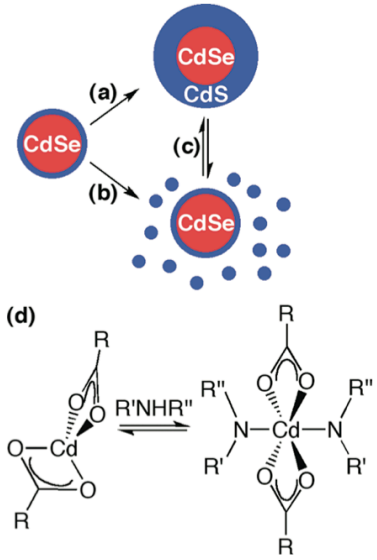

Scheme 1.

Table 1. Synthesis of Thick-Shelled CdSe/nCdS Nanocrystals.

#	CdSe core solution[a]			Cd sltn.		S sltn.	Cd:S ratio	Calc. (theory)	Observed (experimental)
	CdSe conc.	1S (size)	Amine (type)	Cd conc.	Amine (type)	S conc.		#MLs (c/s size)	#MLs (c/s size)
1	19μM	480nm (1.9nm± 0.2nm)	Octadecyl-NH_2 (1°) 1.5M	0.2M	none	0.2M	1:1	13.1MLs (9.6nm)	3.7MLs (4.1nm±1.3nm)
								23.5MLs (15.6nm)	5.3MLs (5.1nm±2.2nm)
2	19μM	480nm (1.9nm± 0.2nm)	oleylNH_2 (1°) 1.5M	0.2M	oleylNH_2 (1°) 1.5M	0.2M	1:1	11.9MLs (8.9nm)	3.0MLs (3.8nm±0.7nm)
								23.5MLs (15.6nm)	5.2MLs (5.0nm±1.1nm)
3	19μM	494nm (1.9nm± 0.2nm)	oleylNH_2 (1°) 1.5M	0.2M	oleylNH_2 (1°) 1.5M	0.2M	1.3:1	11.9MLs (8.9nm)	2.4MLs (3.4nm±0.6nm)
								23.5MLs (15.6nm)	3.1MLs (3.8nm±0.7nm)
4	10μM	488nm (1.9nm± 0.2nm)	oleylNH_2 (1°) 1.5M	0.1M	oleylNH_2 (1°) 1.5M	0.1M	1:1	11.9MLs (8.9nm)	4.2MLs (4.4nm±0.8nm)
								23.5MLs (15.6nm)	7.4MLs (6.3nm±1.0nm)
								35.1MLs (22.4nm)	8.3MLs (6.8nm±1.0nm)
5	10μM	484nm (1.9nm± 0.2nm)	$(octyl)_2NH$ (2°) 1.6M	0.1M	$(octyl)_2NH$ (2°) 1.7M	0.1M	1:1	7.2MLs (6.2nm)	5.2MLs (5.2nm±0.6nm)
								9.6MLs (7.6nm)	11.2MLs (8.7nm±1.0nm)
								11.9MLs (8.9nm)	14.4MLs (10.6nm±1.0nm)
								14.2MLs (10.2nm)	17.9MLs (12.6nm±1.2nm)
6	10μM	625nm (4.7nm± 0.6nm)	$(octyl)_2NH$ (2°) 1.6M	0.1M	$(octyl)_2NH$ (2°) 1.7M	0.1M	1:1	6.0MLs (8.2nm)	5.1MLs (7.7nm±0.8nm)
								8.0MLs (9.3nm)	8.1MLs (9.4nm±1.1nm)
								10.0MLs (10.5nm)	11.0MLs (11.1nm±2.2nm)
								12.0MLs (11.7nm)	13.4MLs (12.4nm±2.2nm)

[a]CdSe core solution: 4 mL ODE, 3.7-3.8 mL amine.

In our investigation, freshly washed CdSe cores were dissolved in ODE and amine (see below) and subjected to different SILAR[33] CdS shell-growth conditions using short 15 min annealing times and $Cd(oleate)_2$ and S_8 precursors (each in ODE or ODE-amine; see the Experimental Section and Table 1). Our experiments started with 19 μM solution of "small

” CdSe cores (1.9 ± 0.2 nm, 1S = 480-494 nm)[58] and high 1.5 M concentration of primary octadecyl amine. ODE solutions of Cd and S precursors did not contain amine (#1 Table 1 and Figure 1). Problems that plague thick-shell core/shell syntheses were immediately clear: Shell-growth (Scheme 1a) was accompanied by many small ca. 2 nm CdS homonuclei (Scheme 1b), and size distributions were large. Critically, core/shells never grew to desired CdS shell thicknesses. Small final particle sizes were observed by TEM. Attempts to grow 13.1 CdS MLs and 23.5 CdS MLs lead instead to 3.7 and 5.3 CdS MLs, respectively (#1 Table 1 and Figure 1). Instead of an ideal one-to-one correlation between desired and observed shell thicknesses, plotting calculated versus TEM-measured shell thicknesses (#CdS MLs) invariably gave a very small slope, m = 0.15 to 0.20.

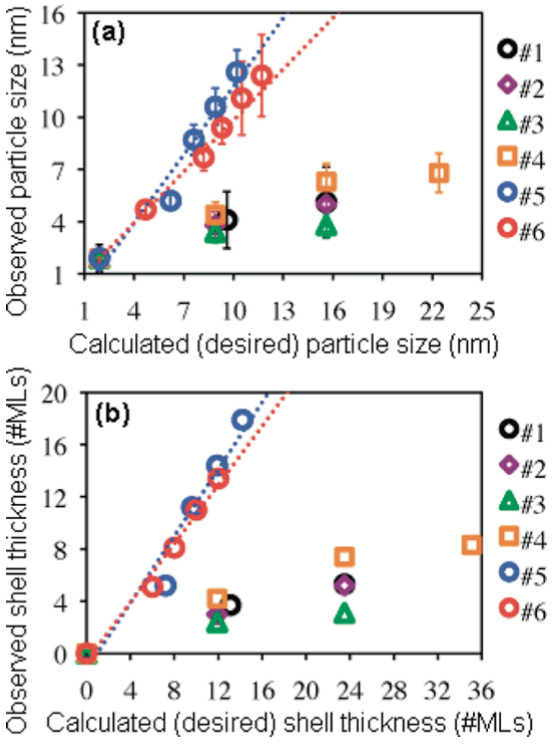

Figure 1. Experimentally observed versus calculated (desired) CdSe/ nCdS particle size (a) and shell thickness (b): From small CdSe (1.9 nm): 19 μM, 0.2 M Cd,S (1:1), no added amine (black circles, Table 1#1); 19 μM, 0.2 M Cd,S (1:1), 1.5 M 1° (oleyl)amine (violet diamonds, Table 1#2); 19 μM, 0.2 M Cd,S (1.3:1), 1.5 M 1° (oleyl)- amine (green triangles,

Table 1#3); 10 μM, 0.1 M Cd and S (1:1), 1.5 M 1° (oleyl)amine (orange squares, Table 1#4);10 μM, 0.1 M Cd,S (1:1), 1.6 to 1.7 M 2° (dioctyl)amine (blue circles, Table 1#5). From large CdSe (4.7 nm): 10 μM, 0.1 M Cd,S (1:1), 1.6 to 1.7 M 2° (dioctyl)amine (red circles, Table 1#6).

Adding primary amine. Initial failure to achieve desired shell-thicknesses and ubiquitous presence of small CdS homonuclei leads us to think a ripening additive could benefit shell growth. Ripening could dissolve CdS homonuclei in favor of epitaxial growth atop existing CdSe/CdS core/shells, leading to effective shell growth (Scheme 1c). Primary amines are known ripening agents.[55,58,59] Octadecyl-NH_2 was present in the starting CdSe core solution, but it was severely diluted during shell growth because neither precursor contained amine: Octadecyl-NH_2 concentration decreased by one order of magnitude during shell growth from 1.5 M to ca. 0.15 M, minimizing its ripening effect. We thus repeated the reaction while maintaining a recurrent stream of primary amine. We specifically added 1.5 M oleyl-NH_2 to Cd precursor. (See the Experimental Section and Table 1.) Particle size dispersions obtained this way were narrower; however, overall results were unsatisfactory as follows: Attempts to grow 11.9 and 23.5 CdS MLs lead instead to 3.0 and 5.2 CdS MLs, respectively (#2 Table 1 and Figure 1). For this set of conditions, the slope of desired versus observed CdS MLs plot remained 0.15 to 0.20.

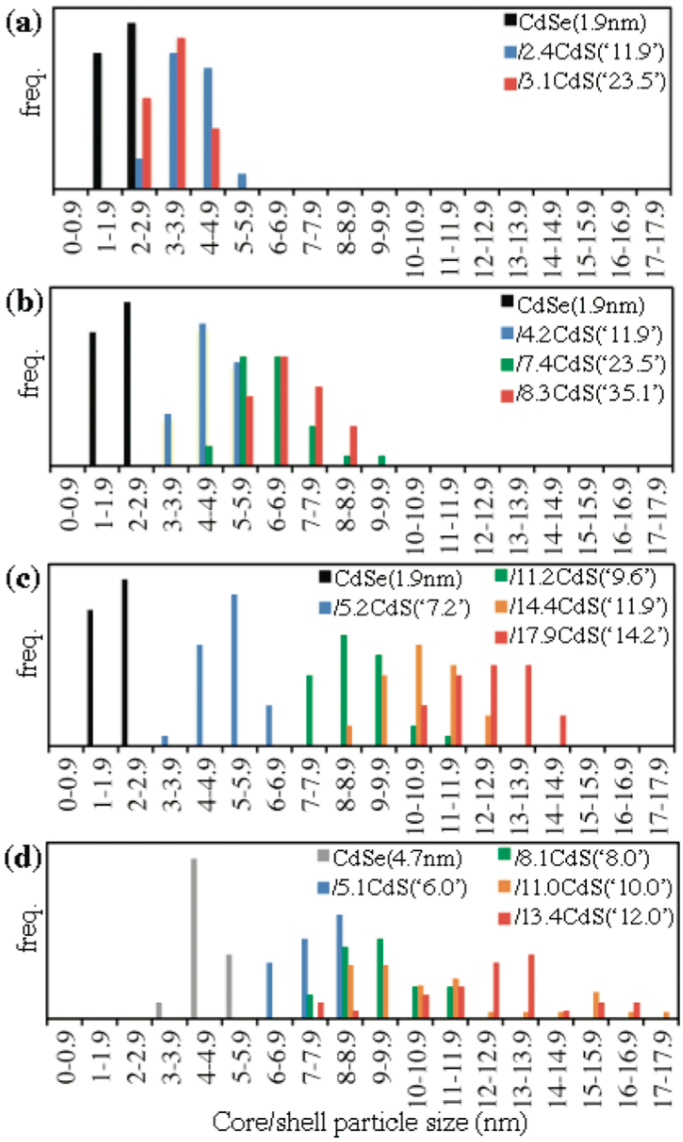

Figure 2. Selected particle size histograms: From small CdSe(1.9nm): (a) 19 μM, 0.2 M Cd,S (1.3:1), 1.5 M 1° (oleyl)amine (Table 1#3). (b) 10 μM, 0.1 M Cd,S (1:1), 1.5 M 1° (oleyl)amine (Table 1#4). (c) 10 μM, 0.1 M Cd,S (1:1), 1.6 to 1.7 M 2° (dioctyl)amine (Table 1#5). From large CdSe (4.7 nm): (d) 10 μM, 0.1 M Cd,S (1:1), 1.6 to 1.7 M 2° (dioctyl)amine (Table 1#6) (≥50-100 particles counted each case).

Adding excess cadmium. Recent studies used 30% excess Cd (1.3:1 Cd to S ratio) to make CdSe/nCdS core/shell nanocrystals with thin-to-medium shell thicknesses ($n \leq 6$).[55] Unfortunately, adding 30% excess Cd precursor did not produce very thick CdS shells ($n \leq 10$). Attempts to grow 11.9 and 23.5 CdS MLs lead instead to 2.4 and 3.1 CdS MLs,

respectively (#3 Table 1 and Figures 1 and 2a). A plot of observed versus desired CdS MLs had slope = 0.13, lower than the two methods above. Incomplete shell growth must be accompanied by large buildup of unreacted Cd and S precursors, saturating the solution and resulting in CdS homogeneous nucleation. CdS homonuclei may act as seeds for isocrystalline CdS shell growth, resulting in wide size distributions. This explains why when using 30% excess Cd apparent shell thicknesses measured by TEM for ≥10 MLs are less than the ≤6 MLs documented in the literature (see above and Table 1 #3).[55]

Lowering core and precursor concentrations. We reasoned that decreasing Cd and S precursor concentrations as well as initial CdSe (core) concentration could suppress homogeneous nucleation. Lower CdSe concentration would keep nanocrystals soluble for longer. Large nanocrystals tend to precipitate out of solution (e.g., shell-thicknesses n ≥ 14 MLs for CdSe (1.9 nm), n ≥ 10 MLs for CdSe (4.7 nm); ≥10 nm particle sizes at 19 mM CdSe). We attempted shell growth halving CdSe (10 μM) and Cd and S (0.1 M each) concentrations while supplying a recurrent stream of 1° oleyl-NH2 (#4 Table 1 and Figures 1 and 2b). This resulted in n ≥ 6 CdS MLs: Attempts to grow 11.9, 23.5, and 35.1 CdS MLs resulted in 4.2, 7.4, and 8.3 CdS MLs, respectively (#4 Table 1 and Figures 1 and 2b). A plot of observed versus desired CdS MLs had slope = 0.24, slightly higher than the other three methods above.

Primary versus Secondary Amines. While primary amines aid ripening, they could simultaneously coordinate to Cd and lower precursor reactivity;[46] the Crystal Structure Database contains several six-coordinate cadmium-carboxylate complexes with monodentate nitrogen ligands (Scheme 1d).[64-68] To probe this issue, we injected $Cd(oleate)_2$ to TOPSe/TOP/ODE in 1° oleylNH_2 or 2° $(octyl)_2NH$[46,69,70] at 300 °C and observed CdSe

growth at 280 °C. After 1 min, CdSe nanocrystals showed 1S = 606 nm (2.05 eV) in 1° oleyl-NH_2, and 1S = 631 nm (1.97 eV) in 2° $(octyl)_2NH$ (Figure 3). Clearly, CdSe made in 1° oleyl-NH_2 was smaller (ca. 4.7 nm) than in 2° $(octyl)_2NH$ (ca. 6.1 nm). It took 5 min for CdSe growth-rate to stabilize (to become constant) in 1° oleyl-NH_2 but under 1 min in 2° $(octyl)_2NH$ (growth may occur via ripening) (Figure 3). This indicates that $Cd(oleate)_2$ reacts much faster in secondary than primary amines.[46,69,70] Therefore, replacing 1° amine with bulkier 2° amine would suppress $Cd(oleate)_2$ coordination while maintaining ripening.[58]

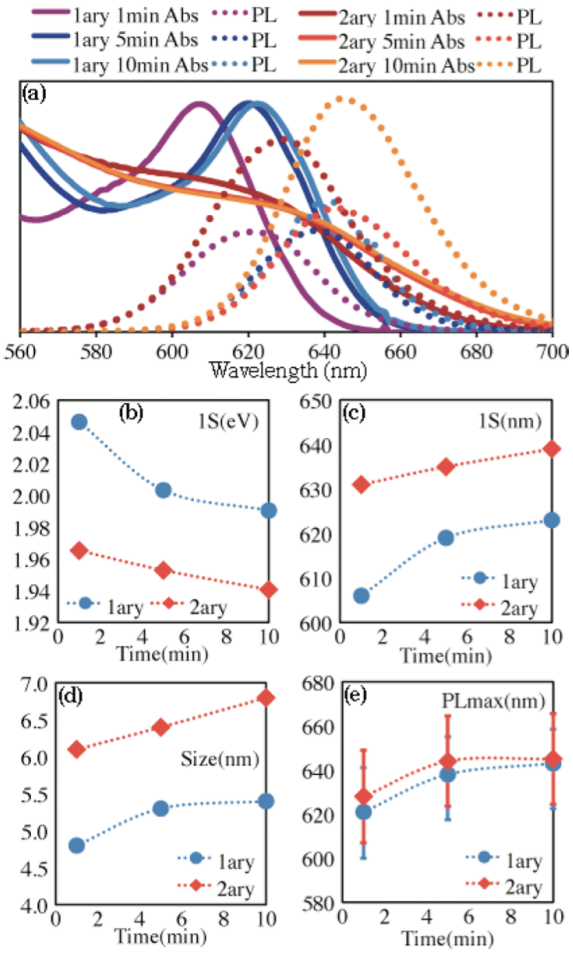

Figure 3. Synthesis CdSe nanocrystals in 1° (oleyl-) versus 2° (dioctyl-) amine: Time evolution of absorption and PL spectra (a), 1S peak (b,c), calculated size (d), and PLmax (±1/2fwhm) (e).

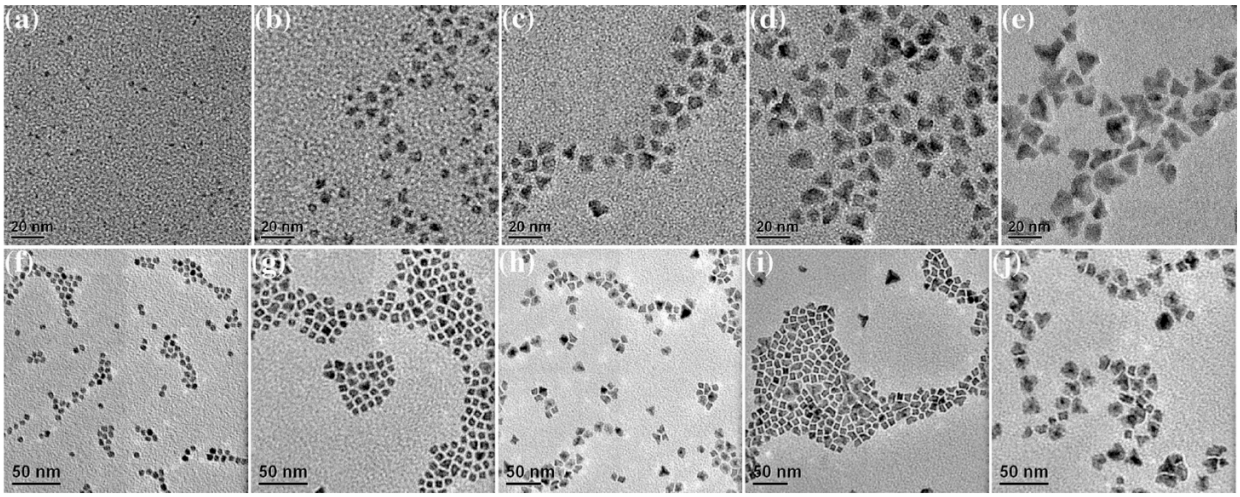

Figure 4. Thick-shell CdSe/nCdS nanocrystals: Top (Table 1#5): From small CdSe (1.9 ± 0.2 nm) (a), CdSe/5.2CdS (5.2 ± 0.6 nm) (b), CdSe/11.2CdS (8.7 ± 1.0 nm) (c), CdSe/14.4CdS (10.6 ± 1.0 nm) (d), and CdSe/17.9CdS (12.6 ± 1.2 nm) (e). Bottom (Table 1#6): From large CdSe (4.7 ± 0.6 nm) (f), CdSe/5.1CdS (7.7 ± 0.8 nm) (g), CdSe/8.1CdS (9.4 ± 1.1 nm) (h), CdSe/11CdS (11.1 ± 2.2 nm) (i), and CdSe/13.4CdS (12.4 ± 2.2 nm) (j).

Growing Thick (n ≥ 10) CdS Shells on Small CdSe (1.9 nm). We reattempted CdS shell-growth on small CdSe cores (10 μM) using 0.1 M Cd and S while supplying recurrent stream of 2° $(octyl)_2NH$ (introduced in CdSe and Cd solutions) (#5 Table 1 and Figures 1, 2c, and 3). This method is superior to all prior conditions: Preparations aimed at growing 7.2, 9.6, 11.9, and 14.2 CdS MLs resulted in 5.2, 11.2, 14.4, and 17.9 CdS MLs, respectively (#5 Table 1 and Figures 1, 2c, and 3). A plot of observed versus desired CdS MLs had slope = 1.28, much higher than other methods (and higher than unity, m > 1; see below).

Growing Thick (n ≥ 10) CdS Shells on Large CdSe (4.7 nm). Using superior conditions above, we attempted CdS shell growth on large CdSe (4.7 nm) (10 μM) using 0.1 M Cd and S while supplying recurrent stream of 2° (dioctyl)amine (introduced in CdSe and Cd solutions) (#6 Table 1 and Figures 1, 2d, and 3).[46,69,70] These conditions were successful: Preparations aimed at growing 6, 8, 10, and 12 CdS MLs resulted in 5.1, 8.1, 11.0, and 13.4

CdS MLs, respectively (#6 Table 1 and Figures 1, 2d, and 3). A plot of observed versus desired number of CdS MLs had slope = 1.12 (also m > 1; see below).

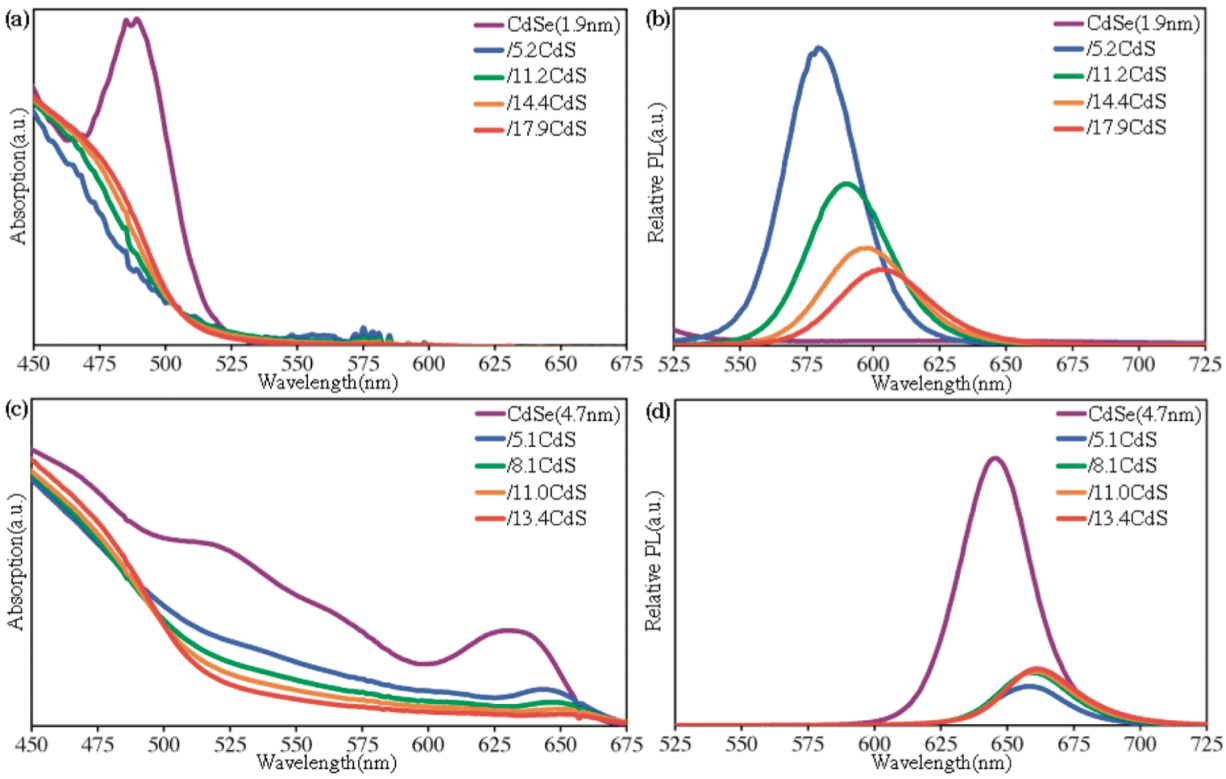

Figure 5. Absorption spectra (arbitrarily normalized) (a,c) and PL spectra (normalized by O.D. at λexc = 510 nm) (b,d) of thick-shell CdSe/nCdS nanocrystals based on small CdSe (1.9 nm) (a,b) and large CdSe (4.7 nm) (c,d).

Observed versus Desired Shell Thickness: Significance of Slope >1. We were puzzled after plotting observed versus desired CdS MLs yielded slopes >1. This occurred when growing thick (≥10 MLs) CdS shells on both small and large CdSe cores using optimum conditions. It is physically impossible for CdS shells to grow thicker than initially estimated given a CdSe core size assuming complete precursor conversion. We could have overestimated CdSe size or concentration (available extinction coefficient data vary somewhat);[3-5,60,71,72] however, more likely is CdSe could get etched in amine-rich medium before shell growth. CdSe etching was observed for different conditions[73,74] and reagents,[75-80]

including amines.[81] Etching before shell growth decreases CdSe core size, rendering precursor amounts larger than needed and resulting in shell thicknesses larger than estimated; this assumes that the CdSe material that is removed during the etching process exists in a yet unidentified inactive, unrecoverable form. Assuming that etching removes a constant number of MLs on small and large CdSe cores, that is, assuming that etching occurs to constant depth on any CdSe surface, this will be more significant for small CdSe (1.9 nm) than for large CdSe (4.7 nm) cores. In agreement with this idea, plotting observed versus desired shell thicknesses resulted in slope not only above unity (>1) but also higher for small (m = 1.28) than for large cores (m = 1.12) (Figure 1a).

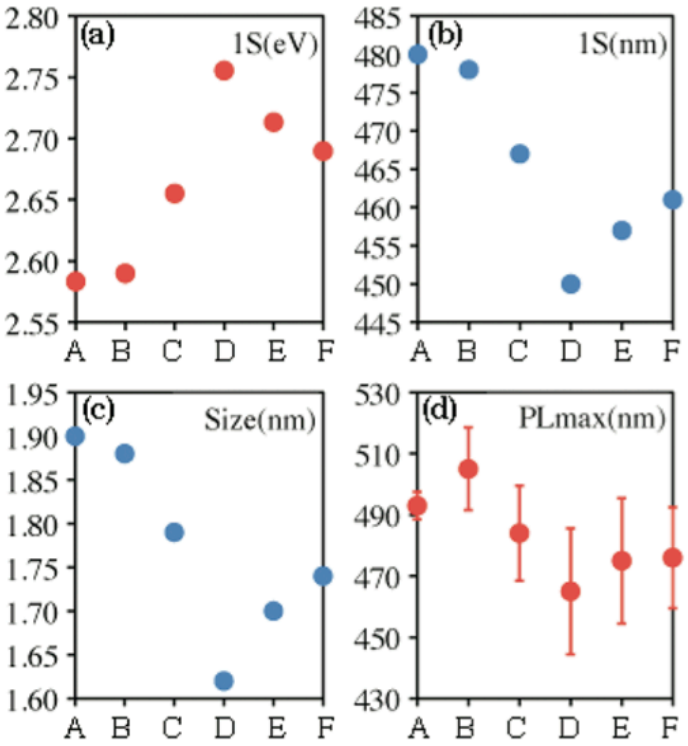

Figure 6. Amine-induced CdSe etching: 1st (1S) absorption (a,b), apparent size (c) and PLmax(±1/2fwhm) (d). CdSe cores: freshly made (crude) (A), washed (B), heated to 75 (C), 190 (D), and 200 °C for 10 min (E), and 20 min (F).

Core-Etching before Shell-Growth. To probe etching, we monitored "apparent" core size right before shell growth by UV-vis and PL starting with CdSe (1.9 nm) having first

absorption peak 1S = 480 nm (2.58 eV) and PLmax = 493 nm (full width at half-maximum, fwhm = 19 nm) (Figure 6A). Upon washing, CdSe size decreased very slightly to "1.88" nm, calculated from 1S = 478 nm (2.59 eV) (redder PLmax = 505 nm and fwhm = 27 nm are attributable to wider size distribution) (Figure 6B). Washed cores were introduced into ODE/$(octyl)_2NH$ and heated to 75 °C. This caused CdSe size to decrease to "1.79" nm, with 1S=467nm (2.66 eV) and PLmax =484 nm (fwhm=31nm) (Figure 6C). Increased heating to 190 °C resulted in smaller CdSe size of "1.62" nm, with 1S = 450 nm (2.76 eV) and PLmax = 465 nm (fwhm = 41 nm) (Figure 6D). After heating for 10 min at initial shell-growth temperature of 200°C, CdSe size was "1.70" nm, with1S=457nm (2.71 eV) and PLmax =475nm (fwhm=41nm) (Figure 6E). After 20 min, CdSe size was "1.74" nm with 1S=461nm (2.69 eV) and PLmax =476nm(fwhm=33nm) (Figure 6F).

This demonstrates CdSe core etching occurs prior to CdS shell-growth.[81] Fast etching in hot $(octyl)_2NH$ removes CdSe surface material. Going from RT to 200 ° C causes 0.28 nm deep CdSe surface etching or ~0.5 MLs (cubic-lattice-parameter = 0.605 nm). Assuming that amine etching proceeds to equal depths on small (1.9 nm) and large (4.7 nm) cores, we calculate that etching decreases nanocrystal volumes by 38 and 16.8%, respectively. Amine-induced etching may arise from quick equilibration between free amine, CdSe, and unidentifiable complexes similar to those in Scheme 1d. Equilibration appears fast and temperature-dependent and is more prominent with increasing temperature (Figure 6C,D). At constant temperature, slow ripening occurs as evidenced by steady regrowth of CdSe over time at 200 ° C (Figure 6E,F).

Growing Very Thick (n ≥ 20) CdS Shells on CdSe. Amine-induced CdSe-etching is most dramatic when growing very thick (n ≥ 20 MLs) CdS shells. Figure 7 shows TEM of

CdSe (1.9 nm)/27CdS and CdSe (4.7 nm)/27CdS obtained by attempting to grow CdSe (1.9 nm)/(‘18’)CdS and CdSe (4.7 nm)/(‘18’)CdS, respectively. The disparity between observed and desired CdS MLs becomes much more prominent as CdS MLs increase (discussion above).

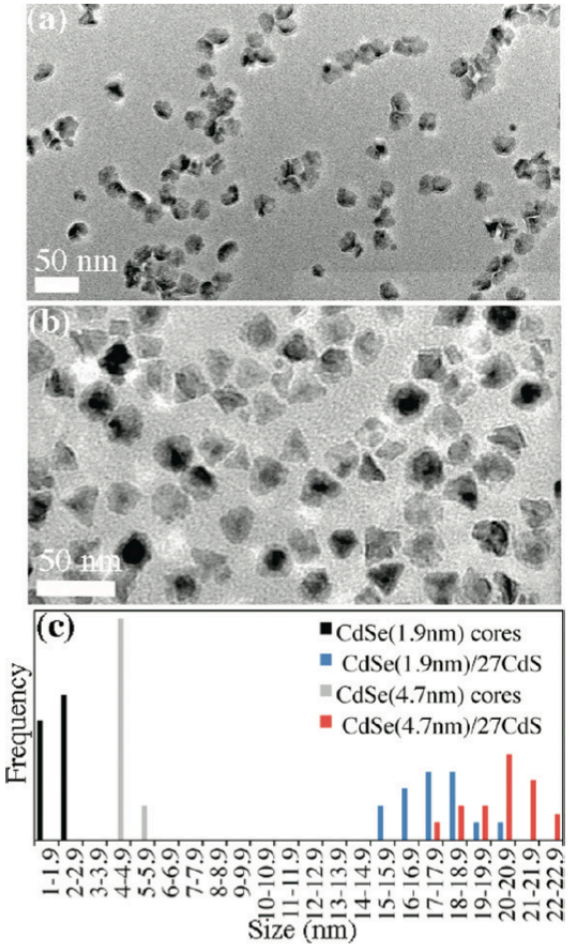

Figure 7. Growth of very thick (n ≥ 20) CdSe/nCdS nanocrystals: TEM of (a) CdSe (1.9 nm)/27CdS (17.7 ± 1.3 nm) and (b) CdSe (4.7 nm)/27CdS (20.3 ± 1.4 nm). (c) Corresponding size histograms.

Annealing Time and Injection Rate. Having optimum shell-growth conditions, we explored annealing and precursor injection rate effects during thick CdSe/nCdS core/shell growth. Annealing could thicken CdS shells from unreacted precursors or cause CdSe/CdS interfacial allowing via Se-S exchange and diffusion. We explored annealing using large

CdSe (4.7 nm)/ 18CdS nanocrystals, picked for easier characterization. Upon annealing at 245 °C for 180 min, TEM showed multiple small ca. 2 nm CdS homonuclei, severely decreasing the average particle size and widening the size distribution from 13.6 ± 3.0 to 7.4 ± 5.6 nm. Without considering CdS homonuclei, size distribution remained 13.9 ± 3.2 nm, and thus annealing did not increase core/shell particle size. Similar effects may occur when using longer wait times (1-3 h) between SILAR injections,[46,57] strengthening the case for short wait times (15 min).[45,55,56] Seldom mentioned in SILAR literature are injection rate effects. We attempted growing CdSe/(‘12’)CdS core/shells using precursor injection rates of 0.2 and 0.4 mL/min and obtained CdSe/ 9.9CdS(10.2 ± 1.4 nm) and CdSe/5.5CdS (7.7 ± 0.9 nm; plus many CdS homonuclei), respectively. Therefore, faster injection rates fail in yielding thick shells.

Structure and Composition Analysis. Small (1.9 ± 0.2 nm) CdSe used here has cubic, zinc blende structure evidenced by energy difference between second (1P) and first (1S) excitonic (absorption) peaks (1P–1S = 303 ± 14 meV, 1S = 2.56 ± 0.03 eV).[56,82-84] Large (4.7 (0.6 nm) CdSe has hexagonal, wurtzite structure evidenced by energy difference between second (1P) and first (1S) excitonic (absorption) peaks (1P–1S = 32.5 ± 0.4 meV, 1S = 2.02 ± 0.01 eV).[56,82] The presence of hexagonal, wurtzite phase in large CdSe cores is evidenced by hexagonal packing seen by TEM (Figure 4f) and 002 peak in XRD (Figure 8a). This agrees with reports on large CdSe made in 1° amines. (See the Experimental Section.)[59] After shell growth, TEM shows cubic and tetrahedral morphologies, suggesting that core/shells derived from small CdSe (1.9 nm) remain mostly cubic, whereas those from large CdSe (4.7 nm) structurally transform from hexagonal to cubic. Ligand-induced structural transformations are known,[87] including cases with 1° amines.[56] However, XRD shows that

significant hexagonal domains are still present, as evidenced by 002(hexagonal)-to-100 and 101(cubic) peak ratios (Figure 8a). Unlike CdSe, which prefers hexagonal structure, CdS prefers cubic structure. CdSe/nCdS core/shells contain much more S than Se: At n > 6 MLs, <10 wt % and <15 at % is Se (Figure 8b,c). Energy-dispersive X-ray spectroscopy (EDS) on core/shells with different thickness shows strong correlation between theoretical and experimental compositions (Figure 8b,c).

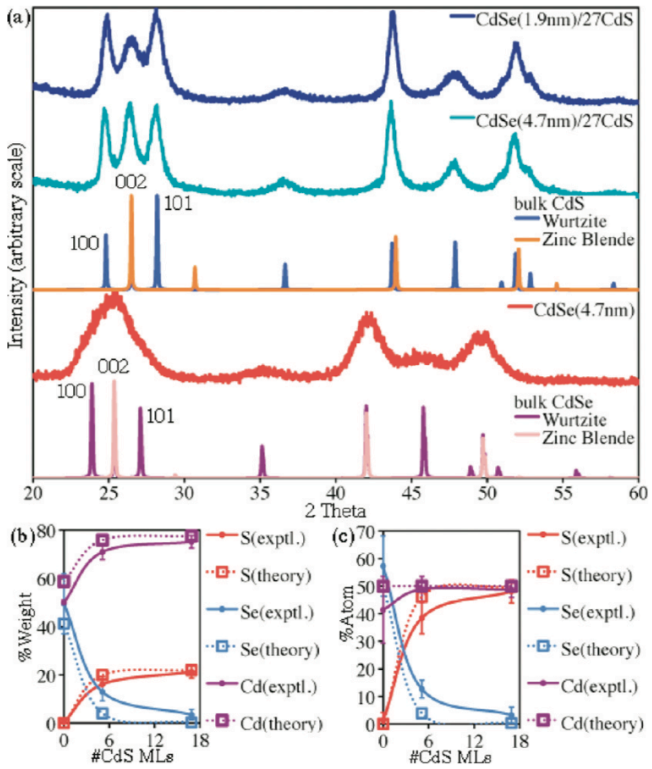

Figure 8. (a) CdSe and CdSe/nCdS(n ≥ 10)XRD (bulk hexagonal-W and cubic-ZB patterns shown for comparison). Comparison of calculated and experimental (EDX) % weight (b) and % atom (c) as a function of shell thickness (n) for CdSe (4.7)/nCdS.

Optical Characterization. Ensemble. CdSe/nCdS 1S peak and PLmax red shift with shell thickness (n) (Figure 5b). This red shift is more pronounced for small CdSe (1.9 nm) than for large CdSe (4.7 nm) (~100 versus ~15 nm for 15CdS MLs, respectively).[55] PL peaks at 30-40% QY for low-to-moderate shell- thicknesses of ca. 4 to 5 MLs, then decreases

with shell thickness. (Some batches reached ~100% QYs, but typical peaks were ~30-40%; there is no consensus as to whether this is an inherent property or signals thicker-shell surface defects.)[6,47-49]

Table 2. Single-Particle Optical Behavior of Thick-Shelled CdSe/nCdS Nanocrystals

sample	exciton lifetime (ns)	>99% non-blinking fraction	>80% non-blinking fraction
CdSe(1.9 nm)/15CdS	55	2	63
CdSe(4.7 nm)/15CdS	10	54	93

Single Particle. To learn more about thick-shell CdSe/CdS structure-property relationships, we recorded single-particle PL exciton lifetime and fluorescence intermittency (blinking) via fluorescence microscopy. CdSe (1.9 nm)/15CdS and CdSe (4.7 nm)/15CdS PL exciton-lifetimes were 55 and 10 ns, respectively (Table 2). Significantly shorter PL lifetimes for large CdSe/CdS indicate stronger electron-hole overlap and agree well with recent calculations.[6,52] In CdSe (4.7 nm)/15CdS, electron and hole wave functions are both strongly confined to CdSe core (type-I configuration), resulting in strong electron-hole overlap and short PL exciton lifetime.[52] In contrast, in CdSe (1.9 nm)/CdS, electron wave function delocalizes out of CdSe core into CdS shell (quasi-type-II configuration), resulting in poor electron-hole overlap and longer PL exciton lifetime.[52] Under the microscope with continuous 488 nm laser excitation, >99 and >80% nonblinking (constantly on) nanocrystal fractions for CdSe (1.9 nm)/15CdS are 2 and 63%, respectively; >99 and >80% nonblinking

fractions for CdSe (4.7 nm)/15CdS are 54 and 93%, respectively. This suggests that type-I CdSe/nCdS nanocrystals based on larger CdSe (4.7 nm) cores show more suppressed (less) blinking than quasi-type-II CdSe/nCdS nanocrystals based on smaller CdSe (1.9 nm) cores. Additional theoretical and experimental spectroscopic studies will be needed to explain this behavior.

Conclusions

We carried out a thorough investigation of thick-shelled CdSe/nCdS ($n \geq 10$) nanocrystal synthesis using short and accessible 15 min wait times between SILAR injections. We found successful shell growth presents unique challenges compared to core/shells with thinner shells. In particular, we explored the effect that added amine, type of amine (1° vs. 2°), core and precursor concentrations, annealing times, and injection rate have on the synthesis of these materials. Main obstacles are how to suppress homogeneous nucleation of CdS, which occurs at high precursor concentration and in the absence of a ripening agent. Additionally, primary amines decrease cadmium precursor reactivity and lead to incomplete shell growth. Based on structural and optical characterization, we found added secondary amine and low core and precursor concentrations, introduced at slow injection rate, result in core/shells with desired particle size and shell thickness. Amine-induced surface etching of CdSe cores decreases their effective size prior to shell growth and significantly affects growth of very thick shells ($n \geq 20$ MLs). The new general method was applied to small CdSe(1.9nm) and large CdSe(4.7nm) cores. The CdSe/nCdS nanocrystals are highly crystalline with a zinc blende crystal structure. Small CdSe(1.9nm) core/shells have longer PL lifetimes and more pronounced blinking at single particle level compared to

large CdSe(4.7nm) core/shells. We expect our new synthetic approach will lead to larger throughput of these materials, increasing availability for fundamental study and application.

Acknowledgement

We thank Iowa State University's Plant Sciences Institute Phase II-Trans-disciplinary Research Program (Diane C. Bassham, PI) and North Dakota State University's Center for Nanoscale Energy (US-DOE DE-FG36-08GO88160, 1.4.f) for funding of this work. We thank Iowa State University (ISU), US-DOE Ames Laboratory Royalty Account, and Institute for Physical Research and Technology (IPRT) for startup funds (J.V.), University of Texas at Dallas for startup funds (A.V.M.), ISU Chemistry Department for a Women in Chemistry award (Y.G.), Cytec Industries, Inc. for a sample of bis(2,2,4-trimethylpentyl)phosphinic acid (TMPPA) (CYANEX272), and Yongfen Chen for helpful discussions. Dedicated to Prof. Jesús E. Morales-Rodríguez (1948-2011) in gratitude for his many years of instructional excellence.

References

[1] Reiss, P.; Protière, M.; Li, L. *Small* **2009**, *5*, 154-168.

[2] Van Embden, J.; Jasieniak, J.; Gómez, D. E.; Mulvaney, P.; Giersig, M. *Aust. J. Chem.* **2007**, *60*, 457-471.

[3] Yu, W. W.; Qu, L.; Guo, W.; Peng, X. *Chem. Mater.* **2003**, *15*, 2854-2860; **2004**, *16*, 560.

[4] Jasieniak, J.; Smith, L.; Van Embden, J.; Mulvaney, P.; Califano, M. *J. Phys. Chem. C* **2009**, *113*, 19468-19474.

[5] Capek, R. K.; Moreels, I.; Lambert, K.; De Muynck, D.; Zhao, Q.; Van Tomme, A.; Vanhaecke, F.; Hens, Z. *J. Phys. Chem. C* **2010**, *114*, 6371-6376.

[6] García-Santamaría, F.; Chen, Y. F.; Vela, J.; Schaller, R. D.; Hol-lingsworth, J. A.; Klimov, V. I. *Nano Lett.* **2009**, *9*, 3482-3488.

[7] Cademartiri, L.; Bertolotti, J.; Sapienza, R.; Wiersma, D. S.; von Freymann, G.; Ozin, G. A. *J. Phys. Chem. B* **2006**, *110*, 671-673.

[8] Smith, A. M.; Nie, S. M. *Acc. Chem. Res.* **2010**, *43*, 190-200.

[9] Talapin, D. V.; Lee, J.-S.; Kovalenko, M. V.; Shevchenko, E. V. *Chem. Rev.* **2010**, *110*, 389-458.

[10] Park, J.; Joo, J.; Kwon, S. G.; Jang, Y.; Hyeon, T. *Angew. Chem. Int. Ed.* **2007**, *46*, 2-33.

[11] Cushing, B. L.; Kolesnichenko, V. L.; O'Connor, C. J. *Chem. Rev.* **2004**, *104*, 3893-3946.

[12] Burda, C.; Chen, X.; Narayanan, R.; El-Sayed, M. A. *Chem. Rev.* **2005**, *105*, 1025-1102.

[13] Wang, X.; Li, Y. *Chem. Commun.* **2007**, 2901-2910.

[14] Rao, C. N. R.; Vivekchand, S. R. C.; Biswasa, K.; Govindaraj, A. *Dalton Trans.* **2007**, 3728-3749.

[15] Rogach, A. L.; Eychmüller, A.; Hickey, S. G.; Kershaw, S. V. *Small* **2007**, *3*, 536-557.

[16] Ivanov, S. A.; Piryatinski, A.; Nanda, J.; Tretiak, S.; Zavadil, K.; Wallace, W. O.; Werder, D.; Klimov, V. I. *J. Am. Chem. Soc.* **2007**, *129*, 11708-11719.

[17] Ivanov, S. A.; Nanda, J.; Piryatinski, A.; Achermann, M.; Balet, L. P.; Bezel, I. V.; Anikeeva, P. O.; Tretiak, S.; Klimov, V. I. *J. Phys. Chem. B.* **2004**, *108*, 10625-10630.

[18] Smith, A. M.; Mohs, A. M.; Nie, S. *Nature Nanotech.* **2009**, *4*, 56-63.

[19] Astashkin, A. V.; Johnson-Winters, K.; Klein, E. L.; Byrne, R. S.; Hille, R.; Raitsimring, A. M.; Enemark, J. H. *J. Am. Chem. Soc*. **2007**, *129*, 14800-14810.

[20] Battaglia, D.; Blackman, B.; Peng, X. *J. Am. Chem. Soc.* **2005**, *127*, 10889-10897.

[21] Kim, J.; Wong, C. Y.; Scholes, G. D. *Acc. Chem. Res.* **2009**, *42*, 1037-1046.

[22] Dabbousi, B. O.; Rodriguez-Viejo, J.; Mikulec, F. V.; Heine, J. R.; Mattoussi, H.; Ober, R.; Jensen, K. F.; Bawendi, M. G. *J. Phys. Chem. B*. **1997**, *101*, 9463-9475.

[23] Talapin, D. V.; Koeppe, R.; Gotzinger, S.; Kornowski, A.; Lupton, J. M.; Rogach, A. L.; Benson, O.; Feldmann, J.; Weller, H. *Nano Lett.* **2003**, *3*, 1677-1681.

[24] Steckel, J. S.; Zimmer, J. P.; Coe-Sullivan, S.; Stott, N. E.; Bulovic, V.; Bawendi, M. G. *Angew. Chem., Int. Ed.* **2004**, *43*, 2154-2158.

[25] Peng, X. G.; Schlamp, M. C.; Kadavanich, A. V.; Alivisatos, A. P. *J. Am. Chem. Soc.* **1997**, *119*, 7019-7029.

[26] Manna, L.; Scher, E. C.; Li, L. S.; Alivisatos, A. P. *J. Am. Chem. Soc.* **2002**, *124*, 7136-7145.

[27] Mekis, I.; Talapin, D. V.; Kornowski, A.; Haase, M.; Weller, H. *J. Phys. Chem. B* **2003**, *107*, 7454-7462.

[28] Pan, D.; Wang, Q.; Jiang, S.; Ji, X.; An, L. *Adv. Mater.* **2005**, *17*, 176-179.

[29] Hao, E.; Sun, H.; Zhou,Z.; Liu, J.; Yang, B.; Shen J. *Chem. Mater.* **1999**, *11*, 3096-3102.

[30] Malik, M. A.; O'Brien, P.; Revaprasadu, N. *Chem. Mater.* **2002**, *14*, 2004-2010.

[31] Wan, Z.; Luan, W.; Tu, S. *J. Phys. Chem. C.* **2011**, *115*, 1569-1575.

[32] Bao, H.; Gong, Y.; Li, Z.; Gao, M. *Chem. Mater.* **2004**, *16*, 3853-3859.

[33] Li, J. J.; Wang, Y. A.; Guo, W. Z.; Keay, J. C.; Mishima, T. D.; Johnson, M. B.; Peng, X. G. *J. Am. Chem. Soc.* **2003**, *125*, 12567-12575.

[34] Fleischhaker, F.; Zentel R. *Chem. Mater.* **2005**, *17*, 1346-1351.

[35] Lee, H.; Leventis, H. C.; Moon, S.-J.; Chen, P.; Ito, S.; Haque, S. A.; Torres, T.; Nüesch, F.; Geiger, T.; Zakeeruddin, S. M.; Grätzel, M.; Nazeeruddin, M. K. *Adv. Funct. Mater.* **2009**, *19*, 2735-2742.

[36] Lee, H. J.; Chen, P.; Moon, S.-J.; Sauvage, F.; Sivula, K.; Bessho, T.; Gamelin, D. R.; Comte, P.; Zakeeruddin, S. M.; Seok, S. I.; Grätzel, M.; Nazeeruddin, M. K. *Langmuir* **2009**, *25*, 7602-7608.

[37] Lee, H.; Wang, M.; Chen, P.; Gamelin, D. R.; Zakeeruddin, S. M.; Graetzel, M.; Nazeeruddin, M. K. *Nano Lett.* **2009**, *9*, 4221-4227.

[38] Blackman, B.; Battaglia, D.; Peng, X. *Chem. Mater.* **2008**, *20*, 4847-4853.

[39] Xu, J.; Cui, D.; Zhu, T.; Paradee, G.; Liang, Z.; Wang, Q.; Xu, S.; Wang, A. Y. *Nanotechnology* **2006**, *17*, 5428-5434.

[40] Blackman, B.; Battaglia, D. M.; Mishima, T. D.; Johnson, M. B.; Peng, X. *Chem. Mater.* **2007**, *19*, 3815-3821.

[41] Chen, D.; Zhao, F.; Qi, H.; Rutherford, M.; Peng X. *Chem. Mater.* **2010**, *22*, 1437-1444.

[42] Talapin, D. V.; Mekis, I.; Gotzinger, S.; Kornowski, A.; Benson, O.; Weller, H. *J. Phys. Chem. B.* **2004**, *108*, 18826-18831.

[43] Xie, R. G.; Kolb, U.; Li, J. X.; Basche, T.; Mews, A. *J. Am. Chem. Soc.* **2005**, *127*, 7480-7488.

[44] Zhang, J.; Tang, Y.; Lee, K.; Ouyang, M. *Science* **2010**, *327*, 1634-1638.

[45] Mahler, B.; Spinicelli, P.; Buil, S.; Quelin, X.; Hermier, J. P.; Dubertret, B. *Nature Mater.* **2008**, *7*, 659-664.

[46] Chen, Y.; Vela, J.; Htoon, H.; Casson, J. L.; Werder, D. J.; Bus-sian, D. A.; Klimov, V. I.; Hollingsworth, J. A. *J. Am. Chem. Soc.* **2008**, *130*, 5026-5027.

[47] Spinicelli, P.; Buil, S.; Quélin, X.; Mahler, B.; Dubertret, B.; Hermier, J.-P. *Phys. Rev. Lett.* **2009**, *102*, 136801-1–136801-4.

[48] Htoon, H.; Malko, A. V.; Bussian, D.; Vela, J.; Chen, Y.; Hollingsworth, J. A.; Klimov, V. I. *Nano Lett.* **2010**, *10*, 2401-2407.

[49] García-Santamaría; Brovelli, S.; Viswanatha, R.; Hollingsworth, J. A.; Htoon, H.; Scott A. Crooker; Klimov, V. I. *Nano Lett.* **2011**, *11*, 687-693.

[50] Buil, S.; Spinicelli, P.; Mallek-Zouari, I.; Camps, G.; Quélin, X.; Mahler, B.; Dubertret, B.; Hermier, J.-P. *J. Phys. B: At. Mol. Opt. Phys.* **2009**, *42*, 114003.

[51] Brovelli, S.; Schaller, R. D.; Crooker, S. A.; García-Santamaría, F.; Chen, Y.; Viswanatha, R.; Hollingsworth, J. A.; Htoon, H.; Klimov, V. I. *Nature Commun.* **2011**, *2*:280, 1-8.

[52] Piryatinski, A.; Ivanov, S. A.; Tretiak, S.; Klimov, V. I. *Nano Lett.* **2007**, *7*, 108-115.

[53] Cragg, G. E.; Efros, A. L. *Nano Lett.* 2010, *10*, 313-31.

[54] Wang, X.; Ren, X.; Kahen, K.; Hahn1, M. A.; Rajeswaran, M.; Maccagnano-Zacher, S.; Silcox, J.; Cragg, G. E.; Efros, A. L.; Krauss, T. D. *Nature* **2009**, *459*, 686-689.

[55] Van Embden, J.; Jasieniak, J.; Mulvaney, P. *J. Am. Chem. Soc.* **2009**, *131*, 14299-14309.

[56] Mahler, B.; Lequeux, N.; Dubertret, B. *J. Am. Chem. Soc.* **2010**, *132*, 953-959.

[57] Vela, J.; Htoon, H.; Chen, Y.; Park, Y.-S.; Ghosh, Y.; Goodwin, P.; Werner, J.; Wells, N. P.; Casson, J. L.; Hollingsworth, J. A. *J. Biophoton.* **2010**, *3*, 706-717.

[58] Van Embden, J.; Mulvaney, P. *Langmuir* **2005**, *21*, 10226-10233.

[59] Zhong, X.; Feng, Y.; Zhang, Y. *J. Phys. Chem. C* **2007**, *111*, 526–531.

[60] Leatherdale, C. A.; Woo, W.-K.; Mikulec, F. V.; Bawendi, M. G. *J. Phys. Chem. B* **2002**, *106*, 7619-7622.

[61] Grabolle, M.; Spieles, M.; Lesnyak, V.; Gaponik, N.; Eychmüller, A.; Resch-Genger, U. *Anal. Chem.* **2009**, *81*, 6285-6294.

[62] Fery-Forgues, S.; Lavabre, D. *J. Chem. Ed.* **1999**, *76*, 1260-1264.

[63] Sun, W.; Marchuk, K; Wang, G; Fang, N. *Anal Chem.* **2010**, *82*, 2441-2447.

[64] Gu, J.-Z.; Lv, D.-Y.; Gao, Z.-Q.; Liu, J.-Z.; Dou, W.; Tang, Y. *J. Solid State Chem.* **2011**, *184*, 675-683.

[65] Zhang, W. H.; Dong, Z.; Yu, Y.; Hou, W. L.; Jin, J. C.; Huang, W. H.; Shi, Q. Z. *Dalton Trans*. **2011**, *40*, 2509-2521.

[66] Liu, Y.-H.; Wu, H.-C.; Lin, H.-M.; Hou, W.-H.; Lu, K.-L. *Chem. Commun.* **2003**, 60-61.

[67] Song, W.-D.; Jia, L.-L.; Wu, H.-M. *Acta Cryst.* **2008**, *E64*, m653.

[68] Duan, J.-G.; Liu, J.-W.; Wu, S. *Acta Cryst.* **2007**, *E63*, m692-m694.

[69] Al-Salim, N.; Young, A. G.; Tilley, R. D.; McQuillan, A. J. Xia, J. *Chem. Mater.* **2007**, *19*, 5185-5193.

[70] Foos, E. E.; Willkinson, J.; Makinen, A. J.; Watkin, N. J.;Kafafi, Z. H.; Long, J. P. *Chem. Mater.* **2006**, *18*, 2886-2894.

[71] Striolo, A.; Ward, J.; Prausnitz, J. M.; Parak, W. J.; Zanchet, D.; Gerion, D.; Milliron, D.; Alivisatos, A. P. *J. Phys. Chem. B* **2002**, *106*, 5500-5505.

[72] De Mello Donegá, C.; Koole, R. *J. Phys. Chem. C* **2009**, *113*, 6511-6520.

[73] Pala, I. R.; Arachchige, I. U.; Georgiev, D. G.; Brock, S. L. *Angew. Chem. Int. Ed.* **2010**, *49*, 3661-3665.

[74] Yao, Q.; Brock, S. L. *Nanotechnology* **2010**, 115502.

[75] Liu, L.; Peng, Q.; Li, Y. *Inorg. Chem.* **2008**, *47*, 5022-5028.

[76] Tonti, D.; Mohammed, M. B.; Al-Salman, A.; Pattison, P.; Chergui, M. *Chem. Mater.* **2008**, *20*, 1331-1339.

[77] Liu, J.; Yang, X.; Wang, K.; Wang, D.; Zhang, P. *Chem. Commun.* **2009**, 6080-6082.

[78] Galian, R. E.; De la Guardia, M.; Pérez-Prieto, J. *J. Am. Chem. Soc.* **2009**, *131*, 892-893.

[79] Gao, F.; Huang, C. J.; Huang, D. D.; Li, J. P.; Sun, D. Z.; Kong, M. Y.; Zeng, Y. P.; Li, J. M.; Lin, L. Y. *J. Cryst. Growth* **2001**, *231*, 17-21.

[80] Rodríguez-González, B.; Sánchez-Iglesias, A.; Giersig, M.; Liz-Marzán, L. M. *Faraday Discuss.* **2004**, *125*, 133-144.

[81] Li, R.; Lee, J.; Yang, B.; Horspool, D. N.; Aindow, M.; Papadi-mitrakopoulos, F. *J. Am. Chem. Soc.* **2005**, *127*, 2524-2532.

[82] Ninomiya, S.; Adachi, S. *J. App. Phys.* **1995**, *78*, 4681-4689.

[83] Norris, D. J.; Bawendi, M. *Phys. Rev. B* **1996**, *54*, 16338-16346.

[84] Efros, A. L.; Rosen, M.; Kuno, M.; Nirmal, M.; Norris, D. J.; Bawendi, M. *Phys. Rev. B* **1996**, *54*, 4843-4856.

[85] Mohamed, M. B.; Tonti, D.; Al-Salman, A.; Chemseddine, A.; Chergui, M. *J. Phys. Chem. B* **2005**, *109*, 10533-10537.

[86] Jaseniak, J.; Bullen, C.; Van Embden, J.; Mulvaney, P. *J. Phys. Chem. B* **2005**, *109*, 20665-20668.

[87] Huang, J.; Kovalenko, M. V.; Talapin, D. V. *J. Am. Chem. Soc.* **2010**, *132*, 15866-15868.

CHAPTER 3

NON-BLINKING QUANTUM DOT FOR 3D SUPER-LOCALIZATION AND HIGH-PRECISION TRACKING AND SUBDIFFRACTION LUMINESCENCE-DEPLETION IMAGING

Reprinted with permission from *J. Am. Chem. Soc*, **2012**, *134*, 6108 and *J. Phys. Chem. C*, **2013**, *117*, 3662.

3D Super-Localization and High-Precision Tracking

Tracking single-molecule and nanoparticle probes with a precision of sub-nanometer to a few nanometers is crucial for elucidating nanoscale structures and movements in biological system. Semiconductors quantum dots hold advantages over traditional organic fluorophores such as narrow size-tunable emission band,[1,2] and increased photostability.[3] However, the use of quantum dots in high-precision tracking has been greatly limited by their intrinsic trait of single-particle fluorescent intermittency.

Having a reliable, highly reproducible method for the synthesis of non-blinking, giant CdSe/CdS nanocrystals at hand, we were in a position where we could study their application to single particle biological (3D) high-precision dynamic tracking.

To test the usefulness of these materials as fluorescent labels in biological systems, a scanning-angle total internal reflection fluorescence microscope (SA-TIRFM) was employed.[4,5] The generation of an exponentially decaying evanescent fielf at the surface of total internal reflection allows for significant background reduction. The SA-TIRFM used here has an in-house computer program that can accurately determine the ideal illumination area for a wide range of angles. [4,5] Giant non-blinking CdSe/CdS nanocrystals were used for

3D dynamic tracking near the total internal reflection (TIR) interface with a sub-10-nm axial localization precision.

Motor proteins, such as kinesin, are essential to cellular functions by transporting intracellur cargo throughout the cell. It has been found that by fixing kinesin to surface followed by introducing solutions of microtubules and adenosine-5'-triphosphate, the microtubules will be propelled laterally.[6,7,8,9] The SA-TIRFM system was used to determine the absolute vertical position of thick-shell nonblinking CdSe/17CdS nanocrysyals in this system.

The nanocrystals were attached to stationary as well as gliding and self-rotating microtubules. The self-induced rotation of microtubules functionalized with giant quantum dots is confined to approximately 50 nm along the z direction. With proper selection of the incident angle, a vast amount of information from the nonblinking quantum dot movement trace could be extracted. The incident angle of the excitation laser was varied from 88.3° to 67.3°, which correspondingly varied the fluorescence signal from the nonblinking giant dots at different axial positions. Using nonlinear least-square fitting, we were able to resolve their absolute axial distance. The unusually prolonged time that our nonblinking giant dots remained in the emissive state was the key to the SA-TIRF instrument's ability to find and replicate optimal incident illumination angles, and thus provided high localization precision.

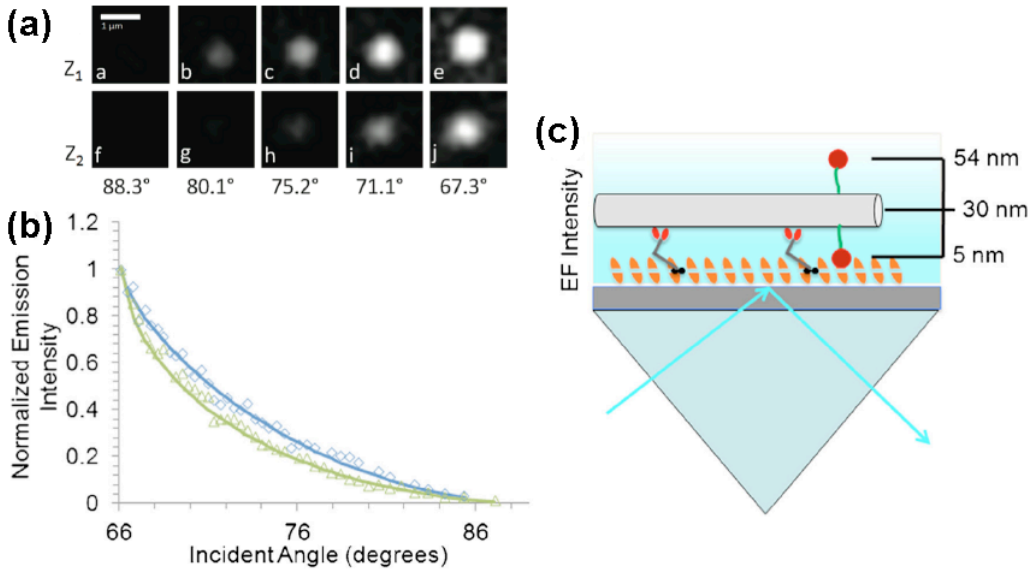

Figure 1. (a) Image set of quantum dots located at different axial positions on stationary microtubules. (b) Fluorescence intensity decay curves for two representative giant dot particles. (c) Schematic of the SA-TIRFM: Cartoon representing important distances of the rotational-microtubule nonblinking quantum dot system (not drawn to scale). Light blue arrow shows angle of incident light and internal reflection.

By controlling the incident light, it is possible to control the depth of the evanescent field (EF), because this is directly related to the fluorescence intensity decay at various axial distances (Figure 1). Figure 1 shows the increase in fluorescence signal for two quantum dots attached to microtubules at different axial positions as the incident angle was varied. Their absolute axial distances can be determined to be 19.0 ± 7.5 and 50.8 ± 4.3 nm, by nonlinear least-square fitting of the intensity curves.[4]

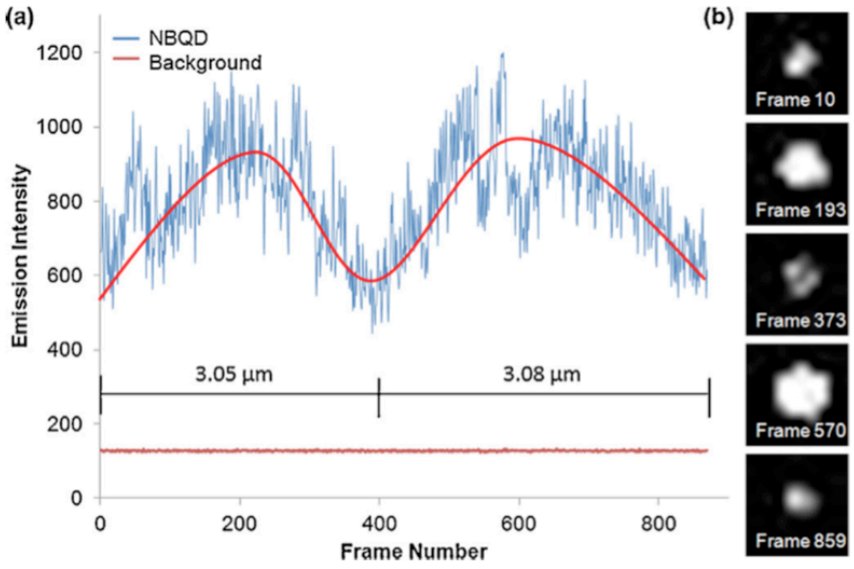

Figure 2. Representative trace of a non-blinking quantum dot attached to a rotating microtubule followed through two periods of rotation.

Figure 2 shows an example trace of a NBQD attached to a rotating microtubule followed for two full periods. It is easy to observe the maximum and minimum intensities as the microtubule travels laterally across the surface. The fluorescence intensity trace seen in Figure 2a was recorded using an incident angle of 80.1°, which produces an EF depth of near 77 nm. The relative change in axial distance Δz was calculated to be 49.5 nm, which translates to the axial distance traveled by the NBQD during microtubule rotation. This value aligns well with the estimated geometrical constraints previously mentioned. Using a particle tracking plugin within the open-source program ImageJ, we tracked the lateral distance traveled during the periods of rotation. The distances were measured to be ~3.1 µm for both rotations. This corresponds to the super-twist length of a microtubule composed of 12 protofilaments.[6] Analysis and measurement of different traces provided distances of 5.4–5.7 µm. These values correspond to a microtubule composed of 14 protofilaments.

In summary, novel quantum dots with suppressed fluorescence intermittency were used in 3D super-localization and dynamic tracking experiments to achieve exceptionally

high precision. The combination of the fully automated SA-TIRFM and nonblinking quantum dots enabled us to find the absolute vertical positions of nonblinking quantum dots attached along the rotational axis of stationary microtubules. The ability to easily tune the incident illumination angle and the stable fluorescence signal of nonblinking quantum dots allowed us to discern the self-rotation of kinesin-driven microtubules taking place within a limited axial width. Looking forward, as the understanding of fluorescence intermittency increases, QDs will continue to become more versatile in their applications.

Subdiffraction, Luminescence-Depletion Imaging

We also studied thick-shelled CdSe/CdS non-blinking quantum dots via stimulated emission depletion (STED) microscopy, an imaging method capable of providing a signal that is below the diffraction limit.[10] In this technique, two overlapped laser beams are applied to the target fluorophore. An inner beam excites the target fluorophore, while the wavelength of a ring-shaped outer beam is tuned to the red edge of the fluorophore's emission spectrum. The resulting signal from the center of the excitation profile is below the diffraction limit.

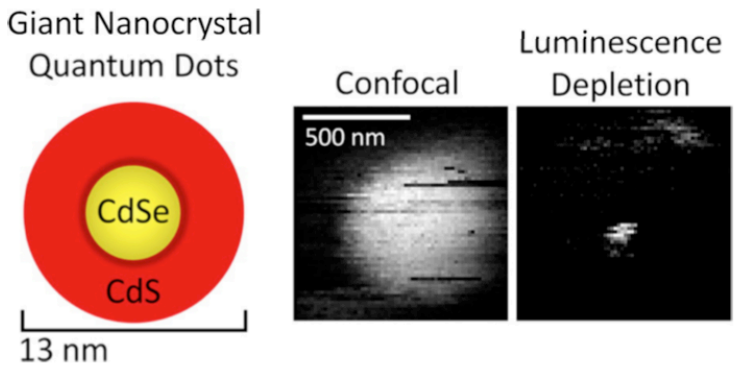

Figure 3. Schematic of CdSe/CdS core-shell giant quantum dots and example sub-diffraction images. Applying diffraction-limited confocal luminescence imaging provided an average

full width at half maximum (FWHM) of 450±90nm, while luminescence depletion imaging gave an average FWHM of 40 ± 10 nm.

The confocal and LD images of 12 quantum dots are shown in Figure 4. The confocal images were recorded using only the excitation beam, while both the excitation and depletion beams were incident upon the sample for the LD images. The improvement in the spatial resolution of the LD images is evident by the smaller feature size. In the confocal images, there are occasional rows of lower luminescence intensity compared to the rest of the pixels representing the g- NQD. This is attributed to a few intermittent blinking periods, characteristic of even the best g-NQDs. The amount of intermittent blinking recorded in the LD images is significantly lower than that in the confocal images, and is only observed for g-NQD number 6. This is expected, since the total time used to collect the nanoparticle's luminescence signal (not the time the nanoparticle is exposed to the laser) in the LD mode is 97.7 ± 0.8% shorter than that used to collect the confocal image.

Cross sections were measured for each g-NQD shown in Figure 4, and representative cross sections are shown in Figure 5. The confocal cross sections were best fit to Gaussians, while the LD cross sections were best fit to Lorentzians. The representative cross sections in Figure 5 show a resolution enhancement, as defined by the full width at half-maximum (fwhm), from 398 nm for the confocal mode to 43 nm for the LD mode. The average fwhm values for 12 g-NQDs are given in Table 1. The average cross section is 450 ± 90 and 40 ± 10 nm for the confocal and LD modes, respectively. For comparison, the actual "physical" average particle size measured by transmission electron microscopy is 13 ± 2 nm.

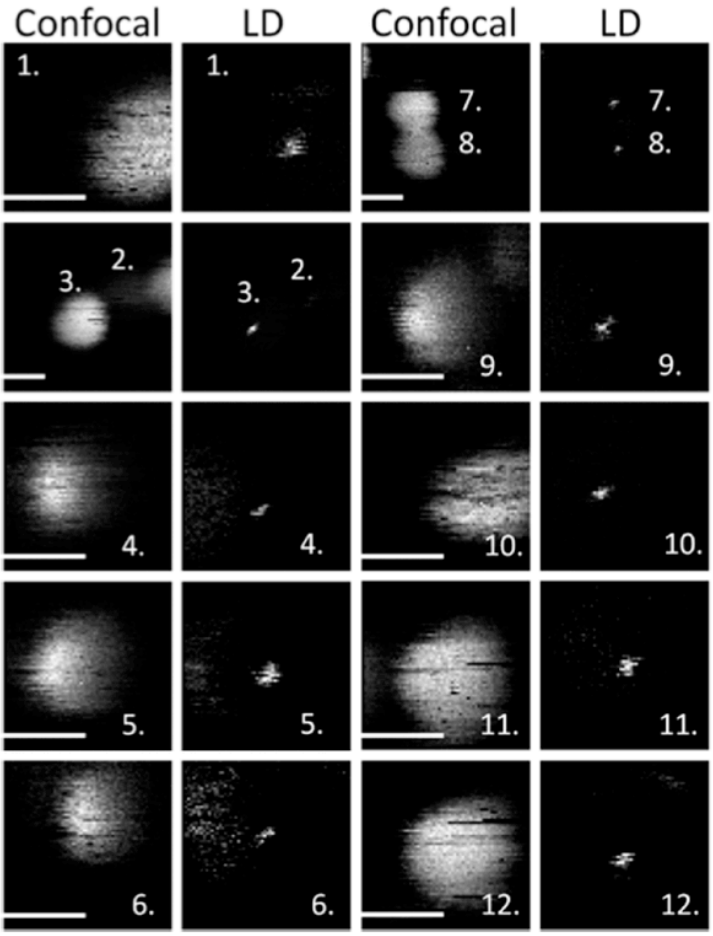

Figure 4. Images of 12 g-NQDs measured in the confocal and LD modes. The confocal images were collected after blocking the depletion beam, and the doughnut shaped depletion beam was unblocked to generate the LD images. The scan direction was from left to right and back right to left with a stage step size of 15.6 nm. A stage repeatability of tens of nanometers results in a small shift from the confocal to LD image. Scale bars are all equal to 500 nm.

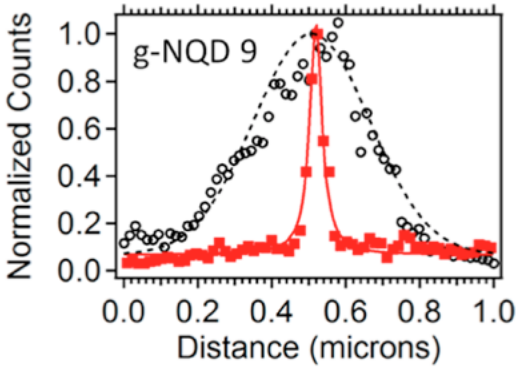

Figure 5. Representative cross sections and associated fits for a g- NQD in confocal (open black circles, Gaussian fit with 398 fwhm) and time-gated LD (solid red squares, Lorentzian

fit with 43 nm fwhm) modes. The time-gate applied to the LD images yields an improvement of 2.25 fold over the ungated LD data. A 7× average lateral resolution improvement is observed for the time-gated STED data over the system's diffraction limit.

Luminescence depletion images of CdSe/14CdS giant nanocrystal quantum dots (g-NQDs) with 13 ± 2 nm particle size have been imaged with 40 ± 10 nm spatial resolution. The mode of resolution enhancement over the diffraction limit is through depletion of the g-NQDs luminescence, suggested to be the result of stimulated emission and absorption working individually or in concert. Time-correlated, single-photon counting detection allowed the signal to be time-gated, which is required for achieving 40 nm spatial resolution. Critical for obtaining this result is that photobleaching was not observed, permitting high quality measurements with extended dwell times that would be difficult to obtain under conditions where photobleaching was present. We conclude that g-NQDs show great promise as robust fluorescent labels for subdiffraction measurements in densely populated systems.

References

[1] Bruchez, M.; Moronne, M.; Gin, P.; Weiss, S.; Alivisatos, A. P. *Science* **1998**, *281*, 2013-2016.

[2] Han, M. Y.; Gao, X. H.; Su, J. Z.; Nie, S. *Nature Biotechnology* **2001**, *19*, 631-635.

[3] Chan, W. C. W.; Nie, S. M. *Science* **1998**, *281*, 2016-2018.

[4] Sun, W.; Marchuk, K.; Wang, G. F.; Fang, N. *Anal. Chem.* **2010**, *82*, 2441-2447.

[5] Sun, W.; Xu, A. S.; Marchuk, K.; Wang, G. F.; Fang, N. *JALA* **2011**, *16*, 255-262.

[6] Ray, S.; Meyhofer, E.; Milligan, R. A.; Howard, J. *Journal of Cell Biology* **1993**, *121*, 1083-1093.

[7] Bohm, K. J.; Stracke, R.; Unger, E. *Cell Biology International* **2000**, *24*, 335-341.

[8] Friedman, D. S.; Vale, R. D. *Nature Cell Biology* **1999**, *1*, 293-297.

[9] Nitzsche, B.; Ruhnow, F.; Diez, S. *Nature Nanotechnology* **2008**, *3*, 552-556.

[10] Lesoine, M. D.; Bhattacharjee, U.; Guo, Y.; Vela, J.; Petrich, J. W.; Smith, E. A. *J. Phys. Chem. C* **2013**, *119*, 3662–3667.

CHAPTER 4

NEAR-INFRARED PHOTOLUMINESCENCE ENHANCEMENT IN Ge/CdS AND Ge/ZnS CORE/SHELL NANOCRYSTALS: UTILIZING IV/II-VI SEMICONDUCTOR EPITAXY

A paper to be submitted to *ACS Nano*

Yijun Guo, Clare E. Rowland, Richard D. Schaller, Javier Vela

Abstract

Ge nanocrystals have a large Bohr radius and a small, size-tunable band gap that may engender direct character via strain or doping effects. Colloidal Ge nanocrystals are particularly interesting in the development of near-infrared materials for applications in bio-imaging, telecommunications and energy conversion. Epitaxial growth of a passivating shell is a common strategy employed in the synthesis of highly luminescent II-VI, III-V and IV-VI semiconductor quantum dots. Here, we use relatively unexplored IV/II-VI epitaxy as a way to enhance the photoluminescence and improve the optical stability of colloidal Ge nanocrystals. Selected based on their relatively small lattice mismatch compared with crystalline Ge, we explore the growth of epitaxial CdS and ZnS shells using the successive ion layer adsorption and reaction method. Powder X-ray diffraction and electron microscopy techniques, including energy dispersive X-ray spectroscopy and selected area electron diffraction clearly show the controllable growth of as many as twenty epitaxial monolayers of CdS atop Ge cores. In contrast, Ge etching and/or replacement by ZnS result in relatively small Ge/ZnS nanocrystals. The presence of an epitaxial II-VI shell greatly enhances the near-infrared photoluminescence and improves the photoluminescence stability of Ge. Ge/II-VI nanocrystals are reproducibly one-to-three orders of magnitude brighter than the brightest

Ge cores. Ge/4.9CdS core/shells show the highest photoluminescence quantum yield and longest radiative recombination lifetime. Thiol ligand exchange easily results in near-infrared active, water-soluble Ge/II-VI nanocrystals. We expect our new synthetic IV/II-VI epitaxial approach will lead to further studies into the optoelectronic behavior and practical applications of Si and Ge-based nanomaterials.

Introduction

Elemental germanium (Ge) is a relatively abundant and robust, covalent semiconductor.[1] Ge has a small indirect band gap (0.661 eV or 1876 nm) and a large Bohr radius (24 nm), which together theoretically provide for a wide range of emission energies attainable via size-tunable quantum confinement.[2,3,4] Further, recent reports suggest that strain[5,6,7] and doping strategies[8] may result in direct band gap Ge nanostructures. As such, Ge is particularly interesting in the development of near-infrared (near-IR) active quantum dot fluorophores for applications in biology (imaging and tracking), telecommunications, and energy conversion (photovoltaics, photocatalysis).

Different routes exist for the synthesis of low dimensional Ge. Reduction of GeI_2 with $LiAlH_4$[9] or hexamethyldisilazane/oleylamine[10] and microwave reduction of GeI_2 and GeI_4 with oleylamine result in colloidal Ge nanocrystals.[11] Reduction of $Ge(OEt)_4$ with trialkoxysilanes[12] and thermal processing of polymeric sol-gel organogermanium oxides (-$PhGeO_{1.5}$-)[13,14] result in SiO_2- and GeO_2-supported Ge nanocrystals, respectively. Pulsed-laser photolysis of $GeMe_4$ in the gas phase also yields Ge nanocrystals.[15] Thermal disproportionation of hydrogen silsesquioxane ($H_8Si_8O_{12}$) and GeI_2 results in $Si_{0.45}Ge_{0.55}$

nanocrystals.[16] A mixed valence iodide reduction method enables the synthesis of alloyed $Ge_{1-x}E_x$ nanocrystals (E = Al, P, Ga, As, In, Sn, Sb, where x > 45%).[17]

Some Ge syntheses reportedly produce fluorescent (photoluminescent) Ge nanocrystals. Reduction of $GeCl_4$ with $NaBH_4$ in polyvinylpyrrolidone (PVP) at room temperature (R.T.)[18] and laser ablation of H-terminated Ge wafers[19] produce violet (380 nm) and blue (450 nm) emitting Ge nanocrystals, respectively. Templated oxidative polymerization of Zintl $(Ge_9)^{4-}$ clusters produces hexagonal Ge mesopores (3.1-3.2 nm pore size) characterized by large surface areas (404-451 m^2/g) and tunable (1.3 to 2.2 nm), wall thickness-dependent photoluminescence (PL, 640-672 nm).[20,21,22,23,24,25] A small subset of available syntheses are believed to produce Ge nanocrystals that emit in the near-IR (800-2500 nm, also called "NIR" region). Reduction of GeI_2 with nBuLi in hexadecylamine, [26] GeI_4 and GeI_2 with hexadecyl- or oleyl-amine,[27] or gaseous $GeCl_4$ with H_2 in a plasma were reported to produce near-IR emitting Ge nanocrystals with tunable band gap.[28] Near-IR PL quantum yields as high as 8% are reported,[26] but much more typically hover between zero (0) and below 1%. Epitaxial growth of a surface-passivating layer is a common strategy employed in the synthesis of highly luminescent II-VI, III-V and IV-VI semiconductor quantum dots.[29,30,31,32,33,34,35,36,37,38] Here, we utilize relatively-unexplored IV/II-VI epitaxy to enhance the photoluminescence and improve the optical stability of Ge nanocrystals.[39,40]

Results and Discussion

Ge crystal chemistry. Elemental germanium adopts the diamond crystal structure that is common to all group IV semiconductors (C, Si, Ge, Sn, Pb) (Figure 1). This diamond structure is topologically similar to, or isotopic with the zinc blende (sphalerite) crystal

structure adopted by many II-VI and III-V semiconductors. In both the diamond and zinc blende structures, each and every atom (or ion) is tetrahedrally coordinated. In the diamond structure, the same atom occupies all positions (for example, Ge as in Ge-Ge-Ge-Ge) (Figure 1a), whereas in the zinc blende structure, two different ions alternate positions (for example, Zn^{2+} and S^{2-} as in Zn-S-Zn-S) (Figure 1b).

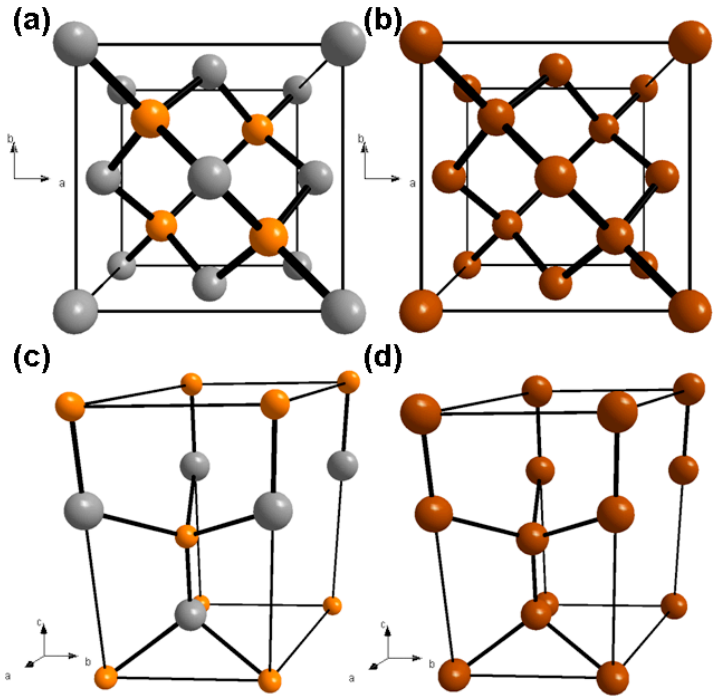

Figure 1. Unit cells of (a) cubic ZnS or CdS (zinc blende), (b) cubic Ge (diamond), (c) hexagonal ZnS or CdS (wurtzite), and (d) hypothetical hexagonal Ge (gray: Zn or Cd; orange: S; brown: Ge).

Selecting shell materials for Ge epitaxy. Because highly crystalline semiconductors tend to possess superior optical qualities, core/shell and multilayer nanostructures require the structure of their individual components to be similar enough so that all interfacial boundaries remain defect-free. In other words, interfacial epitaxy between the different phases must have strict continuity. In a core/shell, this can only be accomplished when the

core and shell materials have identical and/or very similar crystal structures or, more specifically, when both materials are isostructural (isotopic) and share a similar lattice constant (exceptions are uncommon among optical materials[41,42]). As an example, the small lattice mismatch (-3.7%, Table 1) between isostructural CdSe and CdS allowed the growth of thick epitaxial CdS shells on top of CdSe cores.[43,44,45] The resulting high quality, "giant" CdSe/CdS core/shell nanocrystals remain the best example of non-blinking quantum dot fluorophores to date,[46,47,48,49,50,51,52] which allowed their use in 3D super-localization, dynamic tracking, and subdiffraction spatial resolution luminescence depletion imaging.[53,54,55] In contrast, the large lattice mismatch (-11%, Table 1) between CdSe and ZnS did not allow the growth of real (complete) ZnS shells on CdSe cores. Only isolated ZnS islands could be grown on the surface of CdSe cores.[56] For this reason, we decided to investigate shell materials that can adopt a cubic, zinc blende structure with a similar lattice parameter to that of cubic, diamond Ge. Several II-VI and III-V semiconductors are available for this purpose (Table 1). However, we focused on II-VI semiconductors because these are known to be much more chemically and photochemically robust compared to III-V semiconductors. Here, we specifically explore CdS and ZnS as shell materials because the lattice mismatch between these and Ge is relatively small at +3.1 and -4.4, respectively (Table 1). In addition, the valence and conduction energy levels of Ge, CdS and ZnS are such that either type I (Ge/ZnS, Ge/CdS) or quasi-type II (Ge/CdS) heterostructures could be possible depending on the relative size of the Ge core and the thickness of the II-VI shell (Figure 2).[47]

Table 1. Structural and optical properties of II-VI and IV semiconductors: Cores *vs.* possible epitaxial shell materials.

Core/ shell	**Crystal structure**	**Lattice parameters** (% lattice mismatch)[c]	**Band gap Type**	**Bulk value**	**Core quantized (qdot) range**
IV*/IV and* ***IV****/II-VI core/shells*					
Ge/	Diamond	5.658 Å (0%)	Indirect	0.664 eV (1870 nm)	1.46-0.77 eV (850-1600 nm)
Si	Diamond	5.431 Å (-4.0%)	Indirect	1.12 eV (1110 nm)	-
CdS	Zinc blende	5.832 Å (+3.1%)	Direct	2.40 eV (520 nm)	-
ZnS	Zinc blende	5.4063 Å (-4.4%)	Direct	3.60 eV (344 nm)	-
ZnSe	Zinc blende	5.6676 Å (+0.17%)	Direct	2.70 eV (460 nm)	-
II-VI*/II-VI core/shells* (previously synthesized, refs. 29, 30, 43-45)					
CdSe/	Wurtzite[a]	4.299, 7.010 Å (0%)	Direct	1.74 eV (713 nm)	2.53-1.94 eV (490-640 nm)
CdS	Wurtzite[a]	4.1348, 6.749 Å (-3.7%)	Direct	2.40 eV (520 nm)	-
ZnS	Wurtzite[a]	3.814, 6.258 Å (-11%)	Direct	3.60 eV (344 nm)	-
III-V*/II-VI core/shells* (previously synthesized, refs. 31, 36-38)					
InP/	Zinc blende[a]	5.86875 Å (0%)	Direct	1.34 eV (925 nm)	2.53-1.77 eV (490-700 nm)
CdS	Zinc blende[a,b]	5.832 Å (-0.63%)	Direct	2.40 eV (520 nm)	-

[a]Calculated lattice mismatches for II-VI/II-VI and III-V/II-VI core/shells are similar regardless of whether zinc blende (cubic) or wurtzite (hexagonal) structures are considered. [b]InP/CdS were reported to have a wurtzite structure. [c]Calculated as: 100 × [(Shell lattice parameter - core lattice parameter) / core parameter], positive (+) and negative (-) values correspond to core-to-shell lattice expansion and compression, respectively.

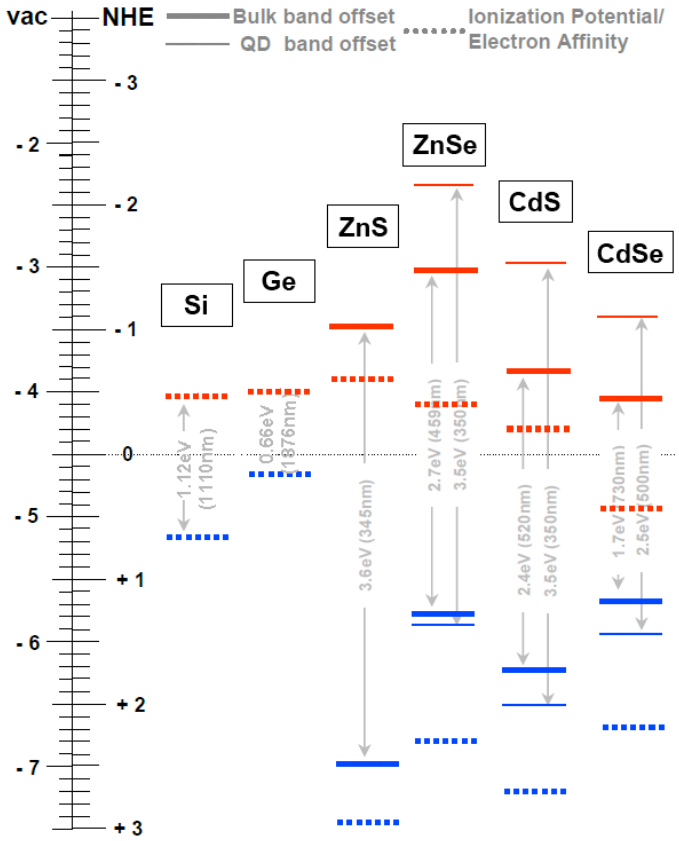

Figure 2. Compilation of valence and conduction energy levels, as well as ionization potentials and electron affinities reported for Ge, ZnS and CdS semiconductors. Si, ZnSe and CdSe are also shown for comparison. The "QD" levels represent maximum band gap

widening due to the effect of quantum confinement in low dimensional (nanosized) semiconductors.

IV/II-VI epitaxy: Synthesis of Ge/CdS core/shell nanocrystals. Nanocrystalline Ge cores, freshly synthesized by reduction of GeI2 with n-butyllithium[32] were reacted with enough Cd and S precursors alternately to form one atomic monolayer (ML) of CdS at a time using the Successive Ion Layer Adsorption and Reaction (SILAR) method.[44,57] We originally carried out this procedure by adding the S precursor solution first, followed by adding the Cd precursor solution (S first, Cd second). Based on the relative electronegativity values ($\chi_{Pauling}$) of Ge (2.01), S (2.58) and O (3.44), oxidation of Ge by S is similar to its oxidation by oxygen, but with a smaller driving force. We thus speculated this could permit a mild and controllable, shallow oxidation of the outermost layer of Ge atoms by S, forming strong Ge-S bonds and allowing shell growth to initiate more smoothly (Scheme 1). However, subsequent experiments showed that the specific order of precursor addition does not matter. Starting with Cd precursor addition, followed by S addition (Cd first, S second) was just as effective in growing thick CdS shells atop Ge cores.

Scheme 1. Illustration of the sulfur-based surface "priming" approach initially used in the synthesis of Ge/CdS and Ge/ZnS core/shell nanocrystals (a). The experimental setup uses two programmable syringe pumps containing the two separate M (Cd or Zn) and S precursor solutions (b).

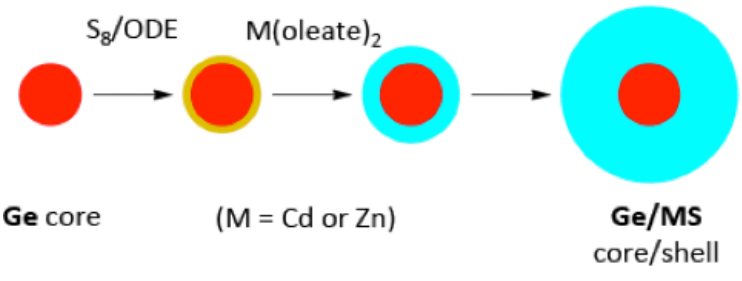

Figure 3 shows transmission electron microscopy (TEM) analyses for a typical shell growth procedure. Starting with cubic Ge cores (with a size or diameter of 4.6±0.7 nm), we were able to grow Ge/nCdS with varying shell thicknesses of up to ca. n = 20 CdS monolayers (MLs): Ge/3.1CdS (6.4±0.8 nm), Ge/4.9CdS (7.4±1.0 nm), Ge/10.5CdS (10.7±1.3 nm), and Ge/18.8CdS (15.5±1.8 nm) (Table 2). All the Ge/CdS core/shell nanocrystal samples have a narrow size distribution (11-13%), comparable or narrower than the initial Ge cores (15%), thus their isolation did not require any size selection.

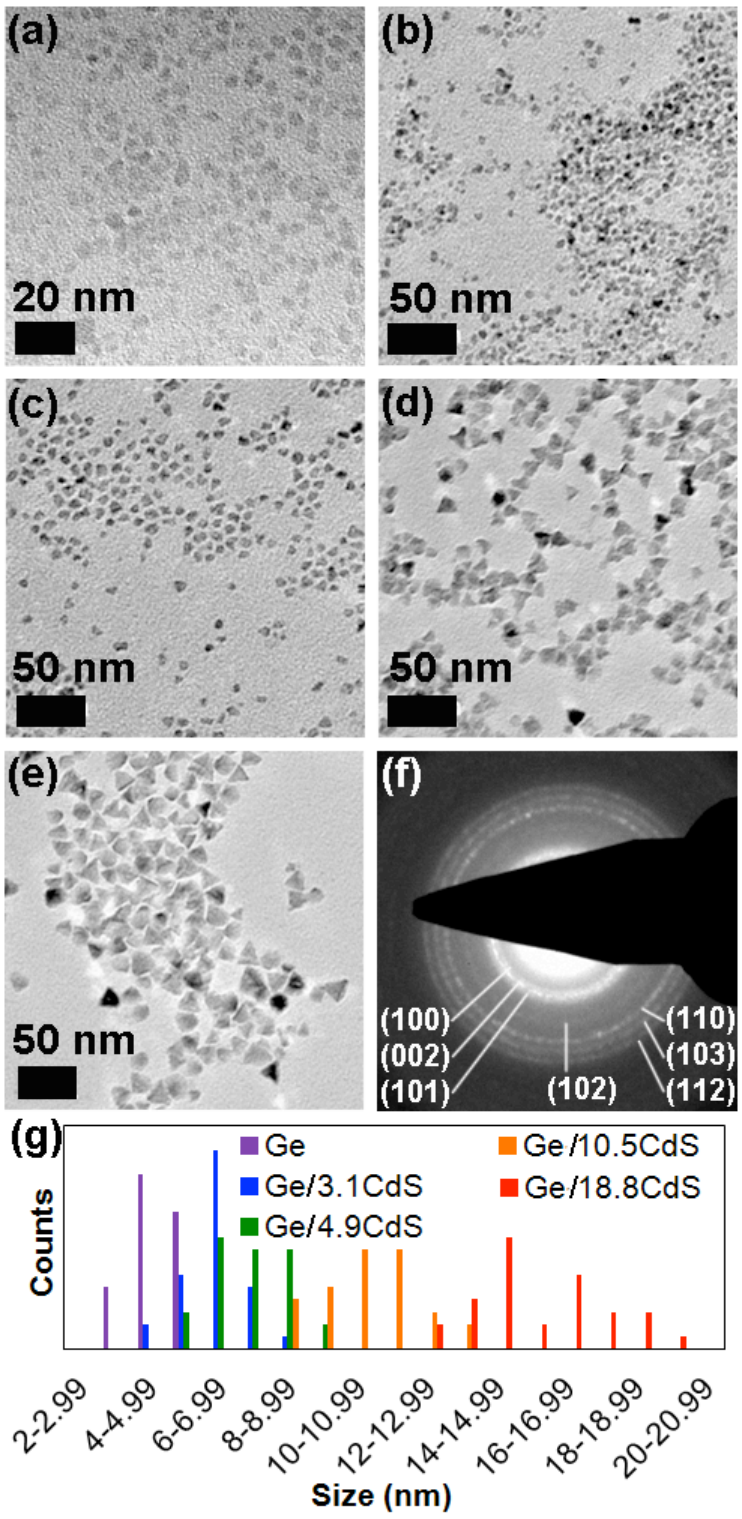

Figure 3. Ge core and thick-shell Ge/nCdS core/shell nanocrystals (n = number of MLs): (a) Ge (4.6±0.7 nm), (b) Ge/3.1CdS (6.4±0.8 nm), (c) Ge/4.9CdS (7.4±1.0 nm), (d) Ge/10.5CdS (10.7±1.3 nm), (e) Ge/18.8CdS (15.5±1.8 nm), (f) SAED pattern of Ge/4.9CdS nanocrystals, and (g) overall size histograms (>200 particles counted in each case).

Table 2. Synthesis of Ge/II-VI Core/shell Nanocrystals.

Sample	Size (nm)	Composition: Ge, M (Cd or Zn), S Theoretical	Composition: Ge, M (Cd or Zn), S EDS	Theoretical Ge core volume	XRD phase(s)
Ge	4.6±0.7	100, 0, 0	100, 0, 0	100%	diamond (cubic)
Ge/3.1CdS	6.4±0.8	40, 30, 30	16±4, 43±3, 41±2	38%	n.d.[b]
Ge/4.9CdS	7.4±1.0	25, 38, 38	5±2, 42±6, 53±7	23%	17% zinc blende (cubic) + 83% wurtzite (hexagonal)
Ge/10.5CdS	10.7±1.3	9, 46, 46	2.0±0.5, 49±4, 49±4	8%	7% zinc blende (cubic) + 93% wurtzite (hexagonal)
Ge/18.8CdS	15.5±1.8	3, 49, 49	2±1, 47±6, 50±6	3%	12% zinc blende (cubic) + 88% wurtzite (hexagonal)
Ge/ZnS[a]	3.8±0.7	n.d.[a]	13±3, 37±5, 49±5	n.d.[a]	zinc blende (cubic)

[a]Partial Ge etching may have occurred (see below), exact no. of MLs unknown. [b]Not determined.

During CdS shell growth, the shape of the Ge/CdS core/shells slowly transforms from spheres (Ge and Ge/3.1CdS) to tetrahedral prisms (Ge/10.5CdS and Ge/18.8CdS) (Figure 3a-d). A tetrahedral morphology is usually a strong indication of a cubic crystal structure. However, powder X-ray diffraction (XRD) (Figure 4) and selected area electron diffraction (SAED) (Figure 3f) are both consistent with all the Ge/CdS core/shells containing a mixture of hexagonal and cubic structures. We believe a plausible explanation for the observed shape evolution is that the original cubic (diamond) structure of the Ge cores could be dictating the final shape of the Ge/CdS core/shells. Crystalline Ge is a covalent material made up of strong Ge-Ge cores. Cubic to hexagonal transformations of Ge may thus involve a large activation energy barrier and may not be nearly as common as for II-VI semiconductors. In fact, hexagonal Ge remains unknown under standard ambient conditions. In contrast, the epitaxial CdS shell could easily adopt a hexagonal (wurtzite) structure, or a cubic (zinc blende) structure, or any combination of the two. Based on the XRD data, Ge/nCdS core/shells having between 5 and 19 MLs are anywhere between 7-17% cubic and between 83-93% hexagonal (Table 2). This is consistent with the fraction of the core/shells made up by the

relatively small Ge core. Based on the number of MLs calculated from TEM data (size histograms), the theoretical Ge core volume falls quickly from 23% to 3% on going from Ge/5CdS and Ge/19CdS, respectively. We also note that, among the possible impurities possible for Ge-based materials, neither the initial Ge cores nor the resulting Ge/CdS core/shells showed any conclusive evidence of GeO_2, GeS_2 or GeS (Figure 4).

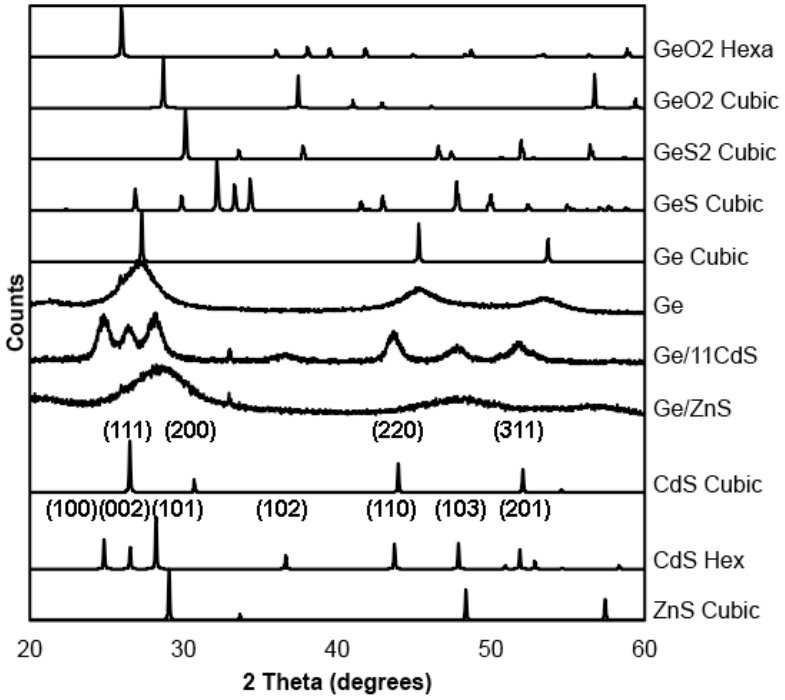

Figure 4. Powder X-Ray diffraction patterns of Ge, Ge/CdS and Ge/ZnS nanocrystals (experimental), and of bulk GeO_2, Ge, CdS and ZnS (for comparison).

Elemental mapping and composition analyses of several individual particles by energy dispersive X-ray spectroscopy (EDX) confirmed the presence and homogeneous distribution of all three Ge, M (Cd or Zn) and S elements within all particles. These data, summarized in Table 2, show good agreement with the theoretical elemental composition calculated from the number of MLs obtained from TEM. Figure 5 shows representative EDX elemental mapping data for Ge/10.5CdS core/shell nanocrystals. Because the core makes only a very small fraction of the sample (ca. 8% in volume, see Table 2), the Ge signal-to-

noise (S/N) ratio is low. Nevertheless, we found no evidence of phase segregation in any Ge/II-VI sample using EDX.

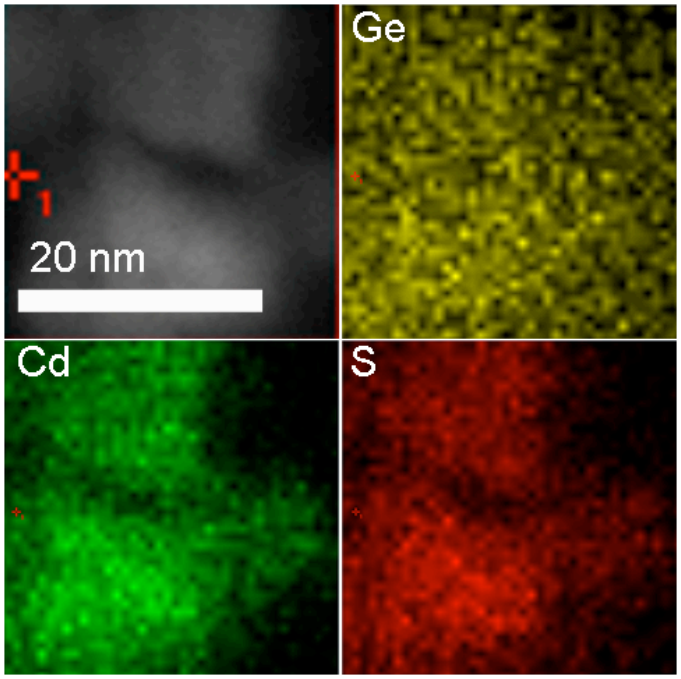

Figure 5. EDX elemental mapping of Ge/10.5CdS nanocrystals does not show any clear evidence of phase segregation (Notes: Shown are four identical or "registered" areas within the same sample; only 8% of this sample's volume is made of Ge, see Table 2).

Synthesis of Ge/ZnS nanocrystals. We also explored a similar SILAR procedure to grow epitaxial ZnS shells on Ge cores. This resulted in Ge/ZnS nanocrystals (3.8±0.7nm) that are either comparable in size or slightly smaller than the initial Ge cores (4.6±0.7 nm) (Figure 6 and Table 2). EDX data of several such particles across multiple areas of different samples consistently showed the presence of all three Ge, Zn and S in significant ratios: 13±3, 37±5 and 49±5 atom%, respectively (Table 2). Of course, it is impossible for the particle size to decrease upon shell growth. Thus, we conclude that the original Ge cores must be undergoing either etching and/or partial exchange by ZnS.[33,34,58,59,60,61] Because the resulting nanocrystals still show the NIR photoluminescence characteristic of Ge, we also conclude

that these nanocrystals must have either a core/shell or graded Ge/ZnS composition.[62] On thinking about why we observe this etching or exchange behavior with ZnS and not with CdS, we note the following differences: First, based on lattice parameters, ZnS leads to compression (-4.4%) while CdS leads to expansion (+3.1%) of the Ge core (Table 1); second, according to Pearson's theory of Hard and Soft Acids and Bases (HSAB)[63,64] Zn^{2+} is a borderline acid while Cd^{2+} is a soft acid; and third, the 0.1 M $Zn(oleate)_2$ precursor solution contains a somewhat higher concentration of excess oleic acid (0.68 M) compared to the 0.1 M $Cd(oleate)_2$ precursor solution (0.24 M) (see below Methods). However, none of these differences provides an immediate or obvious explanation for the observed behavior. A much more detailed study of the underlying causes behind this particular effect is out of the scope of the present manuscript, but will be the subject of a separate article.

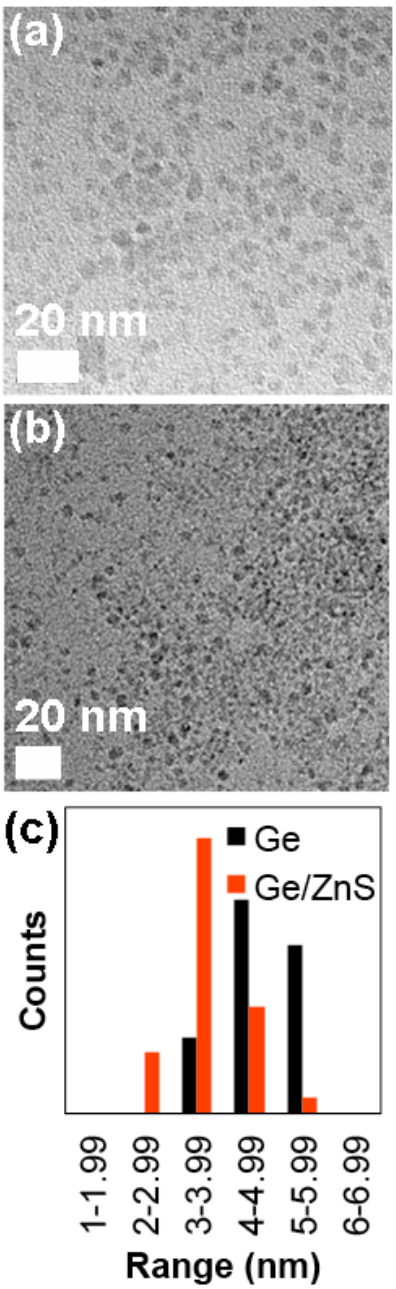

Figure 6. Ge core and Ge/ZnS nanocrystals: (a) Ge (4.6±0.7 nm), (b) Ge/ZnS (3.8±0.7nm), (c) size histograms (>200 particles counted in each case).

Photoluminescence enhancement in Ge/II-VI nanocrystals. Growth of an epitaxial II-VI shell greatly enhances the NIR PL intensity and improves the NIR PL stability of Ge nanocrystals (Table 3, Figures 7 and 8). All the Ge/CdS core/shells and Ge/ZnS nanocrystals we have made showed NIR PL and retained their NIR PL over a period of several months,

regardless of shell thickness or composition. Among the Ge/CdS core/shell nanocrystals with different number of MLs that we studied, Ge/4.9CdS had the highest NIR PL quantum yield of 1.2% (almost three thousand times brighter than the best Ge cores), as well as the longest PL decay lifetime of 2.740±0.01 μs (Table 3 and Figure 8). Additional shell growth lowered the relative PL intensity, as observed previously for giant, thick-shelled CdSe/CdS core/shell nanocrystals (an effect that was attributed to the eventual appearance of cracks or defects due to excessive strain effects).[29,44,45] Nevertheless, all Ge/II-VI nanocrystals consistently showed one-to-three (10-103×) orders of magnitude more intense NIR PL compared to the brightest bare Ge nanocrystals we ever obtained, which produced only 0.0004%, if and when emission was detectable. In fact, Ge cores made by reduction of GeI_2 with nBuLi in hexadecylamine and ODE (see Methods) were only photo luminescent in a minority of cases; roughly one out of every ten or twenty Ge batches made produced measurable PL. Because even the best Ge cores were so weakly emitting, we were unable to measure their PL lifetime (Figure 8b). While the lack of a Ge core-only excited-state lifetime prevents a definitive statement, we note that measured core/shell lifetimes, as shown in Figure 8 and summarized in Table 3 (single exponential fit of the long-lived decay), all fall within a factor of 5 of each other for various CdS shell thicknesses as well as for ZnS. Such comparable lifetimes suggest Type-I band alignment as suggested in Figure 2 for these compositions.

Table 3. Representative Photoluminescence Properties of Ge/II-VI Core/shell Nanocrystals.

Sample	QY (%)	PL Enhancement[a]	Lifetime (ns)
Ge	0.00041	× 1[a]	n.d.[b]
Ge/3.1CdS	0.050	× 120	2280±30
Ge/4.9CdS	1.2	× 2930	2740±11
Ge/4.9CdS in water	0.0029	× 7	596±52
Ge/10.5CdS	0.066	× 160	2440±32
Ge/18.8CdS	0.0060	× 15	1820±261
Ge/ZnS	0.23	× 560	551±13
Ge/ZnS in water	0.0072	× 18	943±19

[a]Relative PL intensity of the Ge cores was set to 1. [b]Not determined: PL was too weak to measure a lifetime.

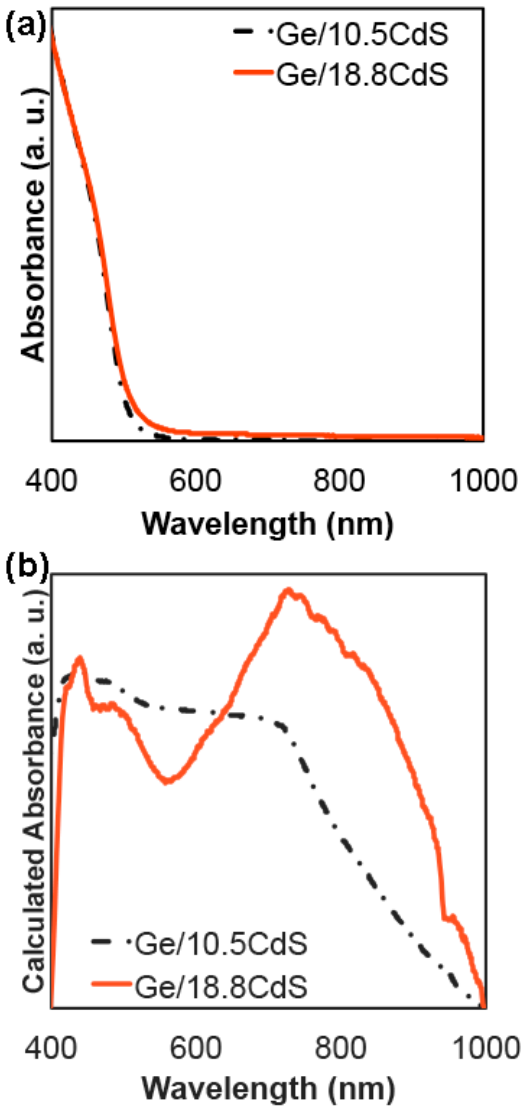

Figure 7. Representative solution phase absorption spectra (a) and solid phase (film) absorption spectra (calculated from diffuse reflectance data, b) for Ge/CdS core/shell nanocrystals. The two clear absorption edges evident at 520 nm (a) and ca. 800 nm (b) originate from the thick CdS shell[29,30,44,45] and Ge core,[26-28] respectively.

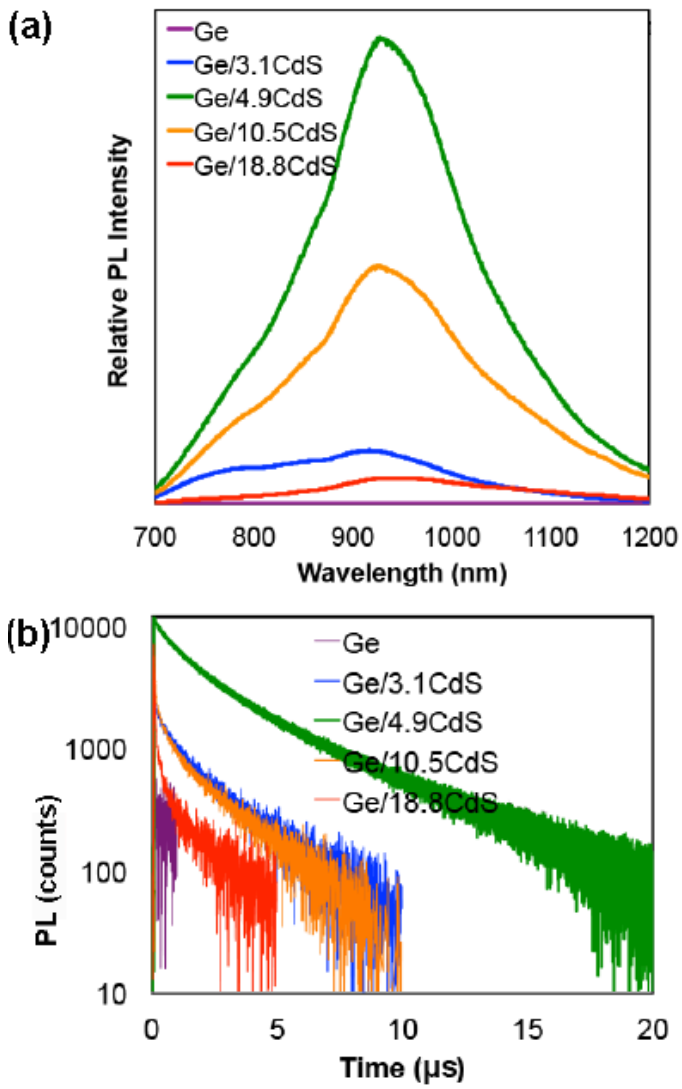

Figure 8. (a) Photoluminescence spectra of Ge, Ge/3.1CdS, Ge/4.9CdS, Ge/10.5CdS and Ge/18.8CdS nanocrystals (normalized by optical density (absorbance) at the excitation wavelength, λ_{exc} = 532 nm). (b) Time-resolved photoluminescence decay of Ge, Ge/3.1CdS, Ge/4.9CdS, Ge/10.5CdS and Ge/18.8CdS nanocrystals (λ_{exc} = 450 nm).

To confirm that Ge, rather than CdS traps, are responsible for the observed near-IR PL (900-1100 nm), we utilized a redder excitation to recollect the photoluminescence data. As shown in Figure 9, the PL spectra of Ge/CdS core/shell nanocrystals collected using 532 nm *vs*. 705 nm laser excitation are very comparable. Because the CdS shell, with a band gap

of ca. 520 nm (2.48 eV), cannot absorb or get excited with the much redder 705 nm laser, we conclude that the Ge core –rather than the CdS shell– is indeed responsible for the observed near-IR emission.

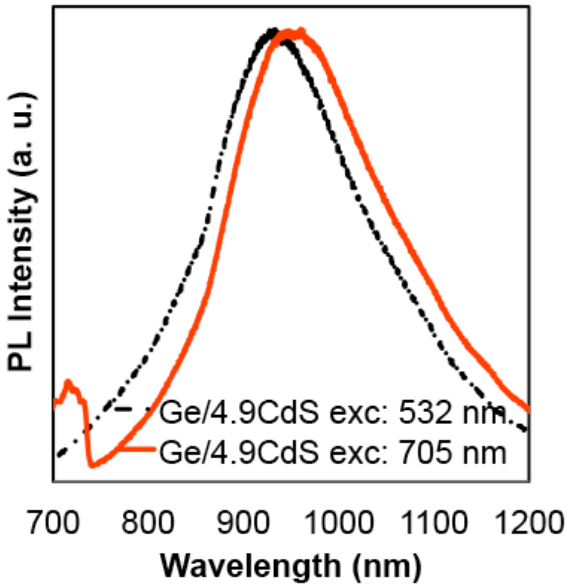

Figure 9. Photoluminescence spectra of Ge/4.9CdS nanocrystals collected with two different excitation wavelengths, λ_{exc} = 532 nm *vs.* λ_{exc} = 705 nm (arbitrarily normalized).

Aqueous solubilization via ligand exchange. Ge/II-VI nanocrystals (both Ge/CdS and Ge/ZnS) easily transfer from organic (typically toluene, hexane or chloroform) to aqueous phase upon ligand exchange with a suitable, water-soluble thiol. Scheme 2 graphically shows this procedure using Ge/4.9CdS and mercaptosuccinic acid as a representative example (see Methods) (Figure 10). Unfortunately, ligand exchange and/or water solubilization results in a decrease of PL intensity. However, the resulting water-soluble Ge/II-VI nanocrystals are still ten times (10×) brighter than the best, uncoated Ge cores (Table 3), which cannot be easily transferred to water.

Scheme 2. Solubilization of Ge/4.9CdS nanocrystals in water *via* thiol ligand exchange.

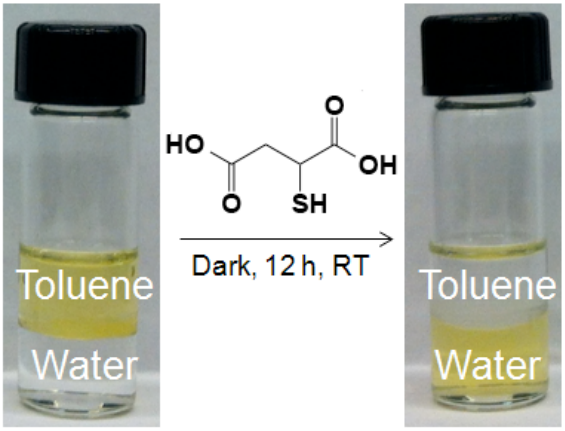

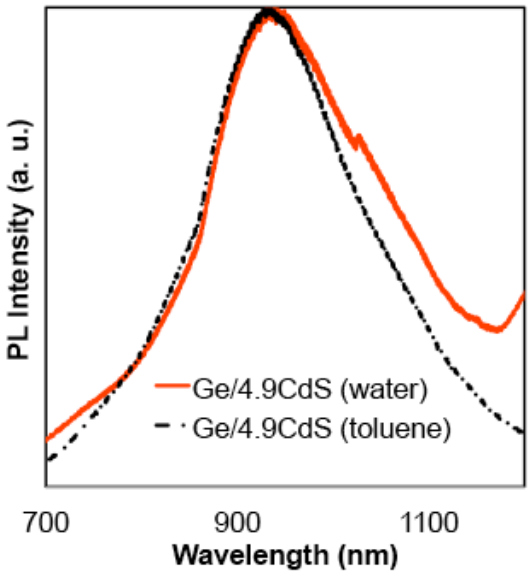

Figure 10. Photoluminescence spectra of Ge/4.9CdS core/shell nanocrystals in toluene and in water (after thiol ligand exchange) with λ_{exc} = 532 (the PL intensities are not relative and were arbitrarily normalized).

Conclusion

Inspired by the prospect of using IV/II-VI epitaxy in colloidal semiconductors, we carried out a thorough investigation on the colloidal synthesis of thick-shelled Ge/MS (M = Cd or Zn) core/shell nanocrystals. We chose CdS and ZnS as shell materials based on their

low lattice mismatch with crystalline Ge. Freshly prepared Ge cores were alternately reacted with enough metal (Cd or Zn) and sulfur (S) precursors to form one epitaxial atomic monolayer at a time using the SILAR method. Elemental mapping confirmed the presence and homogeneous distribution of Ge, M (Cd or Zn) and S elements in all samples. Further, we did not find any evidence of phase segregation in the several Ge/CdS and Ge/ZnS nanocrystals that we made and measured. In addition, analysis of Ge/CdS core/shells with different shell thickness showed a strong correlation between their theoretically expected and experimentally measured elemental compositions. We observed the shape evolution (morphology transformation) of Ge/CdS nanocrystals from spheres to tetrahedral prisms during shell growth. We believe the original cubic structure of the Ge cores played an important role in dictating the final morphology of the Ge/CdS core/shells. In contrast to Ge/CdS, Ge/ZnS nanocrystals did not show the expected larger particle size compared to the initial Ge cores. We attribute this behavior to the combined effect of etching and exchange of Ge by ZnS.

Growth of a CdS or ZnS shell greatly enhances the near-infrared (NIR) photoluminescence intensity and improves the NIR photoluminescence stability of Ge nanocrystals. In general, all Ge/II-VI heterostrucutures showed one-to-three orders of magnitude more intense NIR emission compared to the original Ge cores. All the Ge/CdS and Ge/ZnS nanocrystals retained their NIR photoluminescence after several months. Ge/4.9CdS showed the highest NIR quantum yield and longest PL lifetime. Although there is clearly room for improvement, the achieved PL level is already three thousand times brighter than the most emissive Ge cores we were able to make using literature procedures. Additional CdS shell growth caused a decrease in quantum yield, possibly due to the

introduction of defects due to strain effects. Ge/II-VI nanocrystals easily transfer from organic to aqueous phase upon thiol ligand exchange. We expect that these results will extend the arsenal of quantum dot fluorophores available, particularly near-IR active quantum dots, for fundamental optoelectronic studies as well as for biological imaging and tracking, telecommunications, and energy conversion applications.

Experimental Section

Materials. Cadmium oxide (CdO, 99.998%), zinc oxide (ZnO, 99.99%), sulfur (S_8, 99.999%) and oleic acid (90%) were purchased from Alfa Aesar; n-butyllithium (n-BuLi, 1.6 M hexane solution), dioctylamine ($octyl_2NH$, 98%), tetramethylammoniumhydroxide pentahydrate ($Me_4NOH•5H_2O$, ≥97%) and mercaptosuccinic acid (97%) from Sigma-Aldrich; hexadecylamine ($hexadecylNH_2$, 98%) and 1-octadecene (ODE, 90%) from Acros; sodium chloride (NaCl) from Fisher; and germanium(II) iodide (GeI_2, 99.99+%-Ge) from Strem. Procedures were performed under a dry inert gas atmosphere (N_2 or Ar) inside a glovebox or a Schlenk line unless specified otherwise.

Synthesis. Ge cores. Ge was synthesized by a modified literature procedure.[26] Inside a dry N_2-filled glove box, GeI_2 (0.05 g, 0.15 mmol), hexadecylamine (0.75 g, 3.11 mmol) and a Teflon-coated stir bar were added to an oven dry, four-neck 250 mL round bottom (R.B.) flask. The flask was fitted with a condenser and the system sealed and brought out and connected to a vacuum line. The contents were degassed under vacuum at 80 °C for 30 min, refilled with dry Ar, and heated to 200 °C. After 5 min at this temperature, a mixture of n-BuLi (0.2 mL of 1.6 M hexane solution) and ODE (0.75 mL) made inside the dry-N_2 filled glove box was quickly injected. The mixture was heated to and annealed at 300 °C for 1 h.

The mixture was then allowed to cool down to R.T. The freshly prepared Ge cores were allowed to remain in the crude solution (without washing) under a constant stream of dry Ar until further processing (see Shell Growth below).

Ge/MS nanocrystals (M = Cd or Zn): Precursor solutions. Cd, Zn and S stock solutions were made by a previously reported procedure:[44] 0.2 M $Cd(oleate)_2$. CdO (318 mg, 2.48 mmol), oleic acid (3.09 g, 10.94 mmol), and ODE (7.11 g, 28.16 mmol) were degassed under vacuum at 80 °C for 60 min, refilled with Ar, and heated to 240 °C until optically clear. 0.1 M $Cd(oleate)_2$-amine. $(octyl)_2NH$ (12.5 mL, 41.36 mmol) was degassed under vacuum at 80 °C for 30 min, refilled with Ar, and transferred to another flask containing 0.2 M $Cd(oleate)_2$ (12.5 mL). The mixture was stirred at 60 °C for 20 min. 0.2 M $Zn(oleate)_2$. ZnO (203 mg, 2.49 mmol), oleic acid (6.18 g, 21.88 mmol), and ODE (4.41 g, 17.47 mmol) were degassed under vacuum at 80 °C for 60 min, refilled with Ar, and heated to 240°C until optically clear. 0.1 M $Zn(oleate)_2$-amine. $(octyl)_2NH$ (12.5 mL, 41.36 mmol) was degassed under vacuum at 80 °C for 30 min, refilled with Ar, and transferred to another flask containing 0.2 M $Zn(oleate)_2$ (12.5 mL). The mixture was stirred at 60 °C for 20 min. 0.1 M S_8 precursor solution. S_8 (79.0 mg, 2.47 mmol) and ODE (19.73 g, 78.13 mmol) were degassed under vacuum at 80 °C for 30 min, refilled with Ar, heated to 180 °C for 20 min until optically clear. Shell Growth. ODE (1.5 mL, 4.69 mmol) and dioctylamine (1.5 mL, 4.96 mmol) were introduced to the four-neck 250 mL R.B. flask where the freshly made Ge cores were kept. The mixture was degassed under vacuum at 80 °C for 30 min, refilled with Ar, and heated to a constant shell growth temperature 230 °C. M (Cd or Zn) and S precursors were introduced in an alternating fashion using two programmable syringe pumps, each followed by a 15 min wait period. Either the S (preferred) precursor or the M precursor (Cd

or Zn, also ok) was injected first. Shell growth was monitored by absorption or transmission electron microscopy (TEM) (below) using aliquots (0.05 mL) taken at different shell growth stages. The mixture was allowed to cool to R.T. 15 min after the last M (Cd or Zn) or S injection. Purification. Core/shell nanocrystals were washed three times by precipitation with 1:1 or 1:3 v/v acetone/methanol mixtures and centrifugation at 4200 rpm for 5 min, using each time toluene as the re-dissolution solvent. Transfer to water via ligand exchange. 0.5 mL of "crude" (unpurified) Ge/MS and mercaptosuccinic acid (100 mg, 0.67 mmol) were dissolved in toluene (2.5 mL). A solution of tetramethylammonium hydroxide pentahydrate (600 mg, 3.31 mmol) de-ionized ("de-i") water (3 mL) was added. The mixture was transferred into a vial coated with aluminum foil and vigorously stirred overnight. Water-soluble Ge/nMS were washed once or twice by precipitation with brine (saturated NaCl solution) and centrifugation at 4200 rpm for 5 min, using each time de-ionized water as re-dissolution solvent.

Structural Characterization. Powder X-ray diffraction (XRD) was measured using Cu Kα radiation on Scintag XDS-2000 diffractometer. Transmission Electron Microscopy (TEM) was conducted on carbon-coated copper grids using FEI Technai G2 F20 field emission scanning transmission electron microscope (STEM) at 200 kV (point-to-point resolution <0.25 nm, line-to-line resolution <0.10 nm). Elemental composition was characterized by energy-dispersive spectroscopy (EDS). Particle Analysis. Dimensions were measured manually or with ImageJ for >200 particles. Average sizes (diameters) are reported ± standard deviations.

Optical Characterization. Absorption spectra were measured with an Agilent 8453 UV-Vis photodiode array spectrophotometer. Steady-state PL spectra were measured by

exciting the sample with a 532 nm diode laser and directing the collected PL to a 0.3 m spectrometer and liquid nitrogen-cooled InGaAs photodiode array. Comparison of integrated PL intensity to the organic dye IR-26 (0.05% QY) was used to determine quantum yields.[65,66] Time-resolved PL was measured using time-correlated single photon counting (TCSPC). Samples were photoexcited with a 35-ps pulsewidth, 450-nm diode laser operated between 100 and 400 kHz. TCSPC was then recorded at the PL spectrum maximum using an avalanche photodiode.

Ackowledgement

J.V. gratefully acknowledges the National Science Foundation for funding of this work through a CAREER grant from the Division of Chemistry, Macromolecular, Supramolecular and Nanochemistry (MSN) program (NSF-CHE-1253058). This work was performed, in part, at the Center for Nanoscale Materials, a U.S. Department of Energy, Office of Science, Office of Basic Energy Sciences User Facility under Contract No. DE-AC02-06CH11357. Y.G. is the recipient of an Iowa State University Research Excellence Award and a scholarship from the Midwest Chapter of the Society of Cosmetic Chemists. C.E.R. acknowledges support from a National Science Foundation Graduate Research Fellowship (NSF-DGE-0824162). J.V. and Y.G. thank Iowa State University's Plant Sciences Institute for initial support, as well as Purnima Ruberu and Sam Alvarado for assistance with synthesis and graphics.

References

[1] Cullis, A. G.; Canham, L. T.; Calcott, P. D. J. *Appl. Phys. Rev.* **1997**, *82*, 909−965.

[2] Maeda, Y.; Tsukamoto, N.; Yazawa, Y.; Kanemitsu, Y.; Masumoto, Y. *Appl. Phys. Lett.* **1991**, *59*, 3168−3170.

[3] Wu, Y.; Yang, P. *Chem. Mater.* **2000**, *12*, 605−607.

[4] Sánchez-Péreza, J. R.; Boztugb, C.; Chena, F.; Sudradjatb, F. F.; Paskiewicza, D. M.; Jacobsona, R. B.; Lagallya, M. G.; Paiella, R. *Proc. Natl. Acad. Sci.* **2011**, *108*, 18893−18898.

[5] Sun, X.; Liu, J.; Kimerling, L. C.; Michel, J. *App. Phys. Lett*. **2009**, *95*, 011911-1−3.

[6] Pavarelli, N.; Ochalski, T. J.; Murphy-Armando, F.; Huo, Y.; Schmidt, M.; Huyet, G.; Harris, J. S. *Phys. Rev. Lett.* **2013**, *110*, 177404-1−5.

[7] Camacho-Aguilera, R.; Han, Z.; Cai, Y.; Kimerling, L. C.; Michel, J. *App. Phys. Lett.* **2013**, *102*, 152106-1−3.

[8] Lu, X. M.; Korgel, B. A.; Johnston, K. P. *Chem. Mater.* **2005**, *17*, 6479−6485.

[9] Vaughn II, D. D.; Bondi, J. F.; Schaak, R. E. *Chem. Mater.* **2010**, *22*, 6103–6108.

[10] Muthuswamy, E.; Iskandar, A. S.; Amador, M. M.; Kauzlarich, S. M. *Chem. Mater.* **2013**, *25*, 1416−1422.

[11] Dag, Ö; Henderson, E. J.; Ozin, G. A. *Small* **2012**, *8*, 921−929.

[12] Henderson, E. J.; Hessel, C. M.; Cavell, R. G.; Veinot, J. G. C. *Chem. Mater.* **2010**, *22*, 2653−2661.

[13] Hoffman, M.; Veinot, J. G. C. *Chem. Mater.* **2012**, *24*, 1283−1291.

[14] Kim, C. H.; Im, H. S.; Cho, Y. J.; Jung, C. S.; Jang, D. M.; Myung, Y.; Kim, H. S.; Back, S. H.; Lim, Y. R.; Lee, C.-W.; Park, J.; Song, M. S.; Cho, W.-I. *J. Phys. Chem. C* **2012**, *116*, 26190−26196.

[15] Henderson E. J.; Veinot, J. G. C. *Chem. Mater.* **2007**, *19*, 1886−1888.

[16] Ruddy, D. A.; Erslev, P. T.; Habas, S. E.; Seabold, J. A.; Neale, N. R. *J. Phys. Chem. Lett.* **2013**, *4*, 416−421.

[17] Chou, N. H.; Oyler, K. D.; Motl, N. E.; Schaak, R. E. *Chem. Mater.* **2009**, *21*, 4105−4107.

[18] Shirahata, N.; Hirakawa, D.; Masuda, Y.; Sakka, Y. *Langmuir* **2013**, *29*, 7401−7410.

[19] Armatas, G. S.; Kanatzidis, M. G. *Nano Lett.* **2010**, *10*, 3330−3336.

[20] Armatas, G. S.; Kanatzidis, M. G. *J. Am. Chem. Soc*. **2008**, *130*, 11430−11436.

[21] Bag, S.; Trikalitis, P. N.; Chupas, P. J.; Armatas, G. S.; Kanatzidis, M. G. *Science* **2007**, *317*, 490−493.

[22] Armatas, G. S.; Kanatzidis, M. G. *Nat. Mater*. **2009**, *8*, 217−222.

[23] Kanatzidis, M. G. *Adv. Mater.* **2007**, *19*, 1165−1181.

[24] Armatas, G. S.; Kanatzidis, M. G. *Adv. Mater.* **2008**, *20*, 546−550.

[25] Lee, D. C.; Pietryga, J. M.; Robel, I.; Werder, D. J.; Schaller, R. D.; Klimov, V. I. *J. Am. Chem. Soc.* **2009**, *131*, 3436−3437.

[26] Ruddy, D. A.; Johnson, J. C.; Smith, E. R.; Neale, N. R. *ACS Nano* **2010**, *4*, 7459−7466.

[27] Wheeler, L. M.; Levij, L. M.; Kortshagen, U. R. *J. Phys. Chem. Lett.* **2013**, *4*, 3392−3396.

[28] Chen, Y.; Vela, J.; Htoon, H.; Casson, J. L.; Werder, D. J.; Bussian, D. A.; Klimov, V. I.; Hollingsworth, J. A. *J. Am. Chem. Soc.* **2008**, *130*, 5026−5027.

[29] Mahler, B.; Spinicelli, P.; Buil, S.; Quelin, X.; Hermier, J. P.; Dubertret, B. *Nature Mater*. **2008**, *7*, 659−664.

[30] Dennis, A. M.; Mangum, B. D.; Piryatinski, A.; Park, Y.-S.; Hannah, D. C.; Casson, J. L.; Williams, D. J.; Schaller, R. D.; Htoon, H.; Hollingsworth, J. A. *Nano Lett.* **2012**, *12*, 5545−5551.

[31] Lee, D. C.; Robel, I.; Jeffrey M. Pietryga, J. M.; Klimov V. I. *J. Am. Chem. Soc.* **2010**, *132*, 9960−9962.

[32] Pietryga, J. M.; Werder, D. J.; Williams, D. J.; Casson, J. L.; Schaller, R. D.; Klimov, V. I.; Hollingsworth, J. A. *J. Am. Chem. Soc.* **2008**, *130*, 4879−4885.

[33] Pietryga, J. M.; Schaller, R. D.; Werder, D.; Stewart, M. H.; Klimov, V. I.; Hollingsworth, J. A. *J. Am. Chem. Soc*. **2004**, *126*, 11752−11753.

[34] Pichaandi, J.; van Veggel, F. C. J. M. *Coord. Chem. Rev.* **2014**, 263-264, 138−150.

[35] van Veggel, F. C. J.M. *Chem. Mater.* **2014**, *26*, 111−122.

[36] Reiss, P.; Protière, M.; Li, L. *Small* **2009**, *5*, 154−168.

[37] Rogach, A. L.; Eychmüller, A.; Hickey, S. G.; Kershaw. S. V. *Small* **2007**, *3*, 536−557.

[38] Gejji F. H.; Holt, D. B. *J. Electrochem. Soc*. **1975**, *122*, 535−541.

[39] Paorici, C. G. C.; Pelosi, C.; Servidori, M. *J. Crystal Growth* **1977**, *41*, 181−191.

[40] Zhang, J.; Tang, Y.; Lee, K.; Ouyang, M. *Science* **2010**, *327*, 1634−1638.

[41] Lambright, S.; Butaeva, E.; Razgoniaeva, N.; Hopkins, T.; Smith, B.; Perera, D.; Corbin, J.; Khon, E.; Thomas, R.; Moroz, P.; Mereshchenko, A.; Tarnovsky, A.; Zamkov, M. *ACS Nano* **2014**, *8*, 352–361.

[42] Embden, J. V.; Jasieniak, J.; Mulvaney, P. *J. Am. Chem. Soc.* **2009**, *131*, 14299−14309.

[43] Vela, J.; Htoon, H.; Chen, Y.; Park, Y.-S.; Ghosh, Y.; Goodwin, P.; Werner, J.; Wells, N. P.; Casson, J. L.; Hollingsworth, J. A. *J. Biophoton*. **2010**, *3*, 706–717.

[44] Guo, Y.; Marchuk, K.; Sampat, S.; Abraham, R.; Fang, N.; Malko, A.; Vela, J. *J. Phys. Chem. C* **2012**, *116*, 2791–2800.

[45] Efros. A. L. *Nature Mat*. **2008**, *7*, 612−613.

[46] Piryatinski, A.; Ivanov, S. A.; Tretiak, S.; Klimov, V. I. *Nano Lett.* **2007**, *7*, 108−115.

[47] García-Santamaría, F.; Chen, Y.; Vela, J.; Schaller, R. D.; Hollingsworth, J. A.; Klimov, V. I. *Nano Lett.* **2009**, *9*, 3482−3488.

[48] Mahler, B.; Lequeux, N.; Dubertret, B. *J. Am. Chem. Soc*. **2010**, *132*, 953−959.

[49] Tschirner, N.; Lange, H.; Schliwa, A.; Biermann, A.; Thomsen, C.; Lambert, K.; Gomes, R.; Hens, Z. *Chem. Mater.* **2012**, *24*, 311−317.

[50] Dzhagan, V. M.; Valakh, M. Y.; Raevska, O. E.; Stroyuk, O. L.; Kuchmiy, S. Y.; Zahn, D. R. T. *Nanotechnology* **2009**, *20*, 365704-1−6.

[51] Dzhagan, V. M.; Valakh, M. Y.; Milekhin, A. G.; Yeryukov, N. A.; Zahn, D. R. T.; Cassette, E.; Pons, T.; Dubertret, B. *J. Phys. Chem. C* **2013**, *117*, 18225−18233.

[52] Vela, J. *J. Phys. Chem. Lett*. **2013**, *4*, 653–668.

[53] Marchuk, K.; Guo, Y.; Sun, W.; Vela, J.; Fang, N. *J. Am. Chem. Soc.* **2012**, *134*, 6108–6111.

[54] Lesoine, M. D.; Bhattacharjee, U.; Guo, Y.; Vela, J.; Petrich, J. W.; Smith, E. A. *J. Phys. Chem. C* **2013**, *117*, 3662–3667.

[55] McBride, J.; Treadway, J.; Feldman, L. C.; Pennycook, S. J.; Rosenthal, S. J. *Nano Lett.* **2006**, *6*, 1496–1501.

[56] Li, J. J.; Wang, Y. A.; Guo, W. Z.; Keay, J. C.; Mishima, T. D.; Johnson, M. B.; Peng, X. G. *J. Am. Chem. Soc*. **2003**, *125*, 12567−12575.

[57] Son, D. H.; Hughes, S. M.; Yin, Y.; Alivisatos, A. P. *Science* **2004**, *306*, 1009−1012.

[58] Beberwyck, B. J.; Surendranath, Y.; Alivisatos. A. P. *J. Phys. Chem. C* **2013**, *117*, 19759−19770.

[59] Rivesta J. B.; Prashant K. Jain. *Chem. Soc. Rev.* **2013**, *42*, 89-96.

[60] Gupta, S.; Kershaw , S. V.; Rogach. A. L. *Adv. Mater.* **2013**, *25*, 6923–6944.

[61] Wang, X.; Ren, X.; Kahen, K.; Hahn, M. A.; Rajeswaran, M.; Sara Maccagnano-Zacher, S.; Silcox, J.; Cragg, G. E.; Efros, A. L.; Krauss, T. D. *Nature* **2009**, *459*, 686−689.

[62] Pearson, R. G. *J. Am. Chem. Soc*. **1963**, *85*, 3533−3534.

[63] Pearson, R. G. *Coord. Chem. Rev.* **1990**, *100*, 403−425.

[64] Benfey, D. P.; Brown, D. C.; Davis, S. J.; Piper, L. G.; Foutter, R. F. *App. Optics*, **1992**, *31*, 7034−7041.

[65] Semonin, O. E.; Johnson, J. C.; Luther, J. M.; Midgett, A. G.; Nozik, A. J.; Beard, M. C. *J. Phys. Chem. Lett*. **2010**, *1*, 2445−2450.

CHAPTER 5

SHAPE-PROGRAMMED NANOFABRICATION: UNDERSTANDING THE REACTIVITY OF DICHALCOGENIDE PRECURSORS

Reprinted with permission from *ACS Nano*, **2013**, *7*, 3616.

Yijun Guo, Samuel R. Alvarado, Joshua D. Barclay, Javier Vela

Abstract

Dialkyl and diaryl dichalcogenides are highly versatile and modular precursors for the synthesis of colloidal chalcogenide nanocrystals. We have used a series of commercially available dichalcogenide precursors to unveil the molecular basis for the outcome of nanocrystal preparations, more specifically how precursor molecular structure and reactivity affect the final shape and size of II-VI semiconductor nanocrystals. Dichalcogenide precursors used are diallyl-, dibenzyl-, ditertbutyl-, diisopropyl-, diethyl-, dimethyl- and diphenyl-disulfides, and diethyl-, dimethyl- and diphenyl-diselenides. We find that the presence of two distinctively reactive C-E and E-E bonds makes the chemistry of these precursors much richer and interesting than that of other conventional precursors such as the more common phosphine chalcogenides. Computational studies (DFT) reveal that the dissociation energy of carbon-chalcogen (C-E) bonds in dichalcogenide precursors (R-E-E-R, E = S or Se) increases in the order (R): Diallyl < dibenzyl < ditertbutyl < diisopropyl < diethyl < dimethyl < diphenyl. The dissociation energy of chalcogen-chalcogen (E-E) bonds remains relatively constant across the series. The only exceptions are diphenyl dichalcogenides, which have a much lower E-E bond dissociation energy. An increase in C-E bond dissociation energy results in a decrease in R-E-E-R precursor reactivity, leading to

progressively slower nucleation and higher selectivity for anisotropic growth, all the way from dots to pods to tetrapods. Under identical experimental conditions, we obtain CdS and CdSe nanocrystals with spherical, elongated or tetrapodal morphology by simply varying the identity and reactivity of the dichalcogenide precursor. Interestingly, we find that precursors with strong C-E and weak E-E bond dissociation energies such as Ph-S-S-Ph serve as a ready source of thiol radicals that appear to stabilize small CdE nuclei, facilitating anisotropic growth. These CdS and CdSe nanocrystals have been characterized using structural and spectroscopic methods. An intimate understanding of how molecular structure affects the chemical reactivity of molecular precursors enables highly predictable and reproducible synthesis of colloidal nanocrystals with specific sizes, shapes and optoelectronic properties for customized applications.

Introduction

Dialkyl dichalcogenides (R-E-E-R; where R = alkyl or aryl, E = S, Se or Te) recently re-emerged as highly versatile molecular precursors for the solution-phase synthesis of colloidal nanocrystals. Intriguingly, these dichalcogenides enable the isolation of metastable nanocrystalline phases with unusual composition and morphology. tBu-E-E-tBu (E = S or Se) precursors allow the isolation of $CuInE_2$ and Cu_2SnE_3 nanocrystals with metastable wurtzite phases.[1,2] A change in reaction solvent from oleylamine to squalene leads to $CuInE_2$ nanocrystals with the more stable chalcopyrite phase.[2,3] tBu-S-S-tBu serves as precursor to In_2S_3 nanorods4 and $Cu_{2-x}S$ nanocrystals with a wide range of morphologies (from dots to dodecahedrons).[5] tBu-Se-Se-tBu serves as precursor to SnSe[6], hexagonal BiSe[7], and $Sn_xGe_{1-x}Se$[8] nanocrystals. Photolysis of tBu-Te-Te-tBu in aqueous micellar conditions

yields Te^0 nanorods.[9] Aqueous reaction of Me-Se-Se-Me with $SnCl_2$ in an autoclave yields SnSe nanosheets.[10] Ph-Se-Se-Ph allows the isolation of hexagonal and cubic nanocrystals of $CuInSe_2$ and $Cu_{2-x}S_ySe_{1-y}$.[11,12] Ph-Se-Se-Ph and Ph-Te-Te-Ph are useful alternatives to elemental chalcogenide precursors (Se or Te) in the synthesis of star-shaped SnTe and SnSe nanoparticles.[13] In spite of this very rich chemistry, it remains unclear what factors play a determinant role in the outcome of specific nanocrystal preparations.

Using the far more common phosphine-chalcogenide precursors, we recently found that a single injection of premixed trioctylphosphine-sulfide (Oct_3PS) and selenide (Oct_3PSe) to a bis-octadecylphosphonate-cadmium complex ($Cd(ODPA)_2$) at 320°C produces axially anisotropic $CdS_{1-x}Se_x$ nanorods characterized by having a thick, CdSe-rich "head" and a thin, CdS-rich "tail."[14,15] Using a combined experimental and computational approach, we showed that the time evolution and mechanism of formation mechanism and the S-to-Se content of these compositionally graded $CdS_{1-x}Se_x$ nanorods are direct consequences of relative phosphine-chalcogenide precursor reactivity. Further, by tuning the sterics and electronics of a family of closely related $R_3P=E$ precursors (R = amide, alkyl, aryl or aryloxy; E = S or Se), we reproducibly and predictably synthesized CdE nanorods with controllable aspect (length-to-diameter) ratios between 10-100.[16] These observations open new avenues for achieving "bottom-up," molecular-level control of composition, morphology and properties at the nanoscale.

Unlike phosphine-chalcogenides ($R_3P=E$), which contain only one type of reactive bond (P=E), dichalcogenide precursors (R-E-E-R) contain two different types of reactive bonds (C-E and E-E). We were intrigued by the inherent modularity of these molecular precursors, and wondered how varying the substituents (R = alkyl, aryl) around the reactive -

E-E- unit could affect dichalcogenide precursor reactivity and, ultimately, the outcome of nanocrystal preparations. Experimentally, we observe that differently substituted dichalcogenides lead to completely different nanocrystal morphologies, some lead to dots, others to rods or tetrapods. The selectivity for such anisotropic structures is obviously affected by reaction parameters such as reaction time[17] and temperature,[18,19] precursor concentration,[20] medium acidity,[21] ligand type (amines,[22-24] halides,[52] phosphonic acids[25,26]) and chain length.[27,28] Commonly used methods to obtain II−VI and IV-VI rods and tetrapods include seeded growth,[29-32] continuous precursor injection,[33,34] and noninjection routes.[35] Dichalcogenides offer a unique system where the selectivity for anisotropic structures under identical experimental conditions can be directly traced back to the molecular structure and chemical reactivity of the molecular precursor used. Here we present the results of a combined experimental and computational study aimed at addressing this question.

Results and Discussion

Seeking a deeper understanding of how molecular structure affects chemical precursor reactivity, we subjected different disubstituted dichalcogenides to a consistent set of nanocrystal forming conditions (Scheme 1). Briefly, we injected individual dichalcogenide precursors (1.1 equiv.) to a freshly generated solution of $Cd(oleate)_2$ (0.40 mol), oleic acid (20 equiv.) and oleyl amine (20 equiv.) in 1-octadecene (ODE) (4.6 mL) at 250°C. At regular intervals, we took small equal aliquots from the reaction mixture and monitored nanocrystal evolution (nucleation, growth, and ripening) by optical spectroscopy. After 40 min at 250°C, we isolated and fully characterized the nanocrystalline products. We repeated this procedure

for several different commercially available dichalcogenides having different alkyl and aryl substituents.

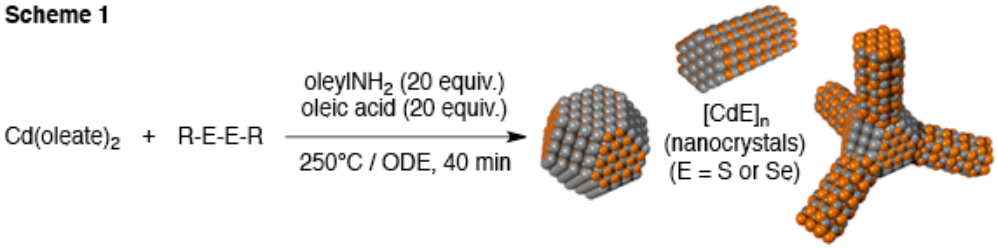

Dichalcogenide precursor chemistry: A springboard to nanocrystal shape diversity. Our experimental observations show that, in general, dichalcogenide precursors that reacted quickly produced spherical nanocrystals, while those that reacted more slowly produced nanocrystals of non-spherical morphology (often tetrapods). Figure 1 shows the time evolution of UV-Vis absorption spectra as well as final (after 40 min) TEM images of CdS nanocrystals obtained with different dialkyl disulfides (R-S-S-R). UV-Vis spectroscopy shows the appearance of the first absorption (1S) peak characteristic of CdS nanocrystals within a few minutes for most precursors. Transmission electron microscopy (TEM) images show that some dichalcogenide precursors lead to the formation of CdS nanocrystals with a spherical morphology, while others lead to the formation of CdS nanocrystals with a tetrapod morphology.[36-38] The majority of spherical CdS nanocrystals (dots) have a zinc blende (cubic) structure, while the CdS tetrapods are comprised of wurtzite (hexagonal) arms extending from the {111} facets of zinc blende (cubic) cores (seeds).[39-41] Based on these results, it is clear that the structure of the molecular precursor has considerable influence on the rate of growth, size and morphology of the resulting nanocrystals.

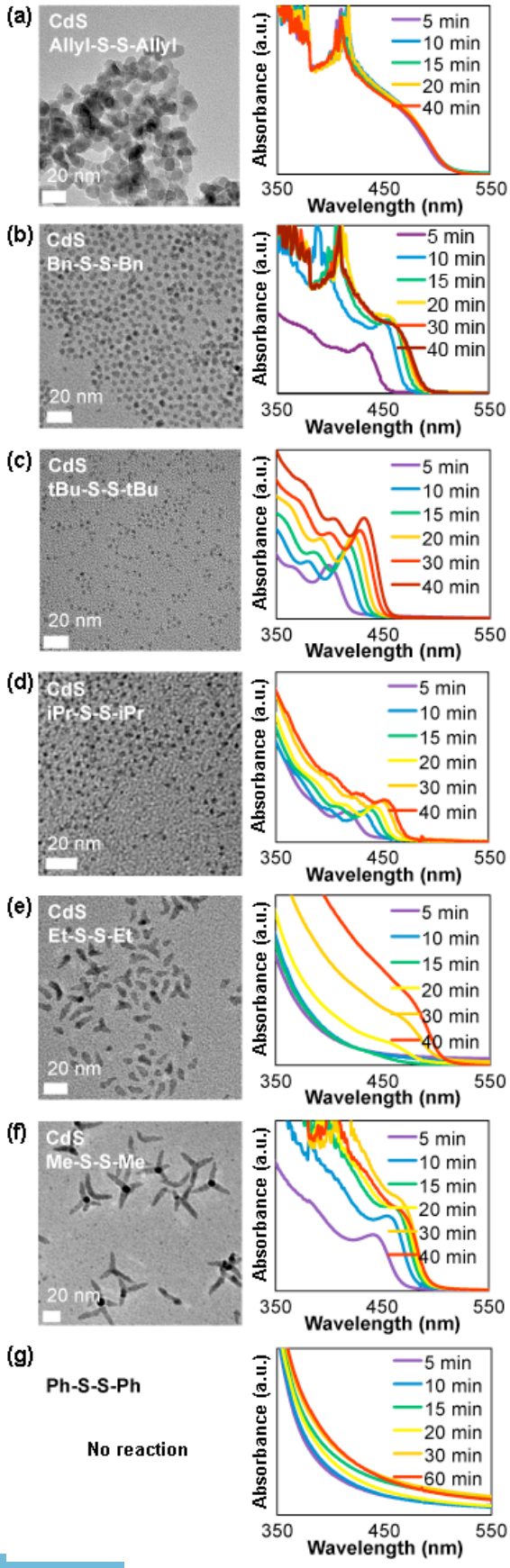

Figure 1. Representative TEM images after 40 min (left panel) and time evolution of UV-Vis absorption spectra (right panel) of CdS nanocrystals obtained with (a) diallyl-, (b) dibenzyl-, (c) ditertbutyl-, (d) diisopropyl-, (e) diethyl- and (f) dimethyl-disulfide precursors. (g) Diphenyl-disulfide was unreactive under identical conditions (0.40 mol $Cd(oleate)_2$, 1.1 equiv. R-S-S-R, 20 equiv. oleic acid, 20 equiv. oleyl amine, 4.6 mL ODE, 250°C).

Assessing the strength of C-E and E-E bonds from computations. To better understand these observations, we computationally studied the different dichalcogenide precursors using the GAMESS software. We computed their carbon-chalcogen (C-E) and chalcogen-chalcogen (E-E) bond dissociation energies (BDEs, Scheme 2) using density functional theory (DFT) with the Boese-Martin Kinetics (BMK) functional, which has been shown to be a viable method to calculate thermodynamic properties such as BDEs at a lower computational cost than high-precision methods such as G3. Table 1 and Figure 2 show the computed BDEs of all precursors we investigated.

Scheme 2

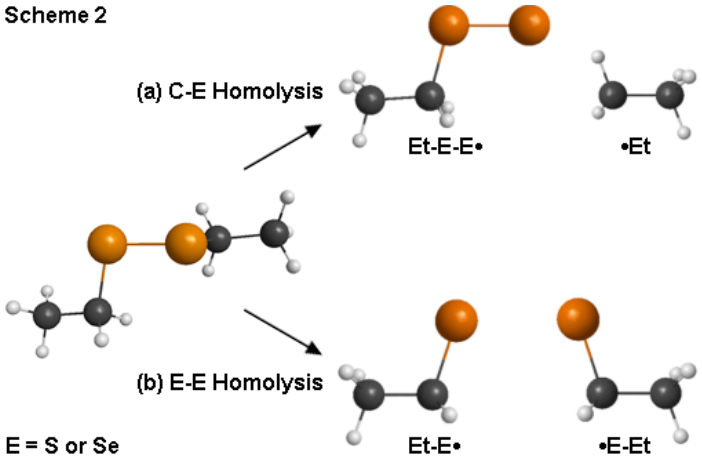

Table 1. Calculated bond dissociation (homolysis) energies (BDEs) for dialkyl dichalcogenide precursors (R-E-E-R, E = S or Se) and experimentally observed products from their reaction with $Cd(oleate)_2$.[a]

Precursor(s) R-E-E-R (E = S or Se)	C-E BDE kcal/mol	E-E BDE kcal/mol	(C-E)-(E-E) kcal/mol	40 min Product morphology (1*S* peak)	Size[b] / nm
Allyl-S-S-Allyl	45.71	61.33	-15.62	Nanocrystals[c] (480 nm)	9.4 ± 1.3
Bn-S-S-Bn	48.50	62.45	-13.94	Nanocrystals[c] (480 nm)	4.2 ± 0.6
tBu-S-S-tBu	52.81	59.39	-6.59	Quantum dots[c] (430 nm)	2.2 ± 0.2
iPr-S-S-iPr	55.45	59.69	-4.24	Quantum dots[c] (450 nm)	1.8 ± 0.3
Et-S-S-Et	58.13	59.48	-1.35	Pods/Multipods (470 nm)	Pod length: 10.3 ± 2.8 Pod width: 5.1 ± 0.6
Me-S-S-Me	59.03	58.04	+0.99	Tetrapods (465 nm)	Pod length: 19.5 ± 2.9 Pod width: 5.5 ± 0.5
Ph-S-S-Ph	69.75	45.65	+24.11	No reaction (n.a.)	-
Bn-S-S-Bn + Ph-S-S-Ph (1:1)	-[d]	-[d]	-[d]	Rods (470 nm)	Rod length: 11.5 ± 1.5 Rod width: 4.4 ± 0.5
tBu-S-S-tBu + Ph-S-S-Ph (1:1)	-[d]	-[d]	-[d]	Tetrapods (455 nm)	Pod length: 24.1 ± 4.7 Pod width: 3.5 ± 0.4
iPr-S-S-iPr + Ph-S-S-Ph (1:1)	-[d]	-[d]	-[d]	Tetrapods (455 nm)	Pod length: 21.3 ± 4.5 Pod width: 2.3 ± 0.3
Et-Se-Se-Et[e]	52.01	56.41	-4.40	Nanocrystals[c] (670 nm)	6.6 ± 0.6
Me-Se-Se-Me[f]	53.76	51.94	+1.82	Multipod clusters (685 nm)	65.7 ± 13.1
Ph-Se-Se-Ph	64.44	43.63	+20.80	Quantum dots[c] (550 nm)	3.5 ± 0.5

[a]Conditions: 0.40 mol $Cd(oleate)_2$, 1.1 equiv. R-E-E-R, 20 equiv. oleic acid, 20 equiv. oleyl amine, 4.6 mL ODE, 250°C, 40 min (except [e]Et-Se-Se-Et, 10 min, [f]Me-Se-Se-Me, 5 min). [b]Average sizes (50-100 particles) ±

one standard deviation. [c]Quantum dots have average diameters smaller than the Bohr radius reported for CdS (2.5-3.0 nm) or CdSe (5.4 nm).[64-66] [d]Not applicable (used a mixture of two precursors, see first column).

C-E and E-E BDEs: Comparison to prior experimental and computational data.

In terms of absolute value, our computational results appear to underestimate the experimentally measured values reported previously for disubstituted dichalcogenides, particularly in the case of E-E BDEs. For example, laser photofragmentation time-of-flight mass spectrometric studies of Me-S-S-Me, •S-S-Me, and •S-Me yielded at 0 K a C-S BDE of 55.0 kcal/mol and a S-S BDE of 72.4 kcal/mol at 0 K,[42] compared to our calculated values of 59.03 kcal/mol and 58.04 kcal/mol, respectively (Table 1). This discrepancy could be due to either computational or experimental error. In terms of the trends observed, our computational results are in agreement with those observed experimentally. E-E BDEs measured experimentally are generally quoted in the range 51-72 kcal/mol;[43] those derived from calorimetry are 66.1 kcal/mol for Et-S-S-Et, 65.2 kcal/mol for Me-S-S-Me, and 51.2 kcal/mol for Ph-S-S-Ph,[44-48] compared to our calculated values of 59.48 kcal/mol, 58.04 kcal/mol, and 45.65 kcal/mol, respectively (Table 1). Our computational results compare well with previous calculations reported for disubstituted dichalcogenide compounds. Early computational references on C-S and S-S BDEs used a complete basis set approach instead of DFT.[49] High-level *ab initio* approaches using G3, G3B3, CBS-Q, CBS-4M, CCSD(T), and ROMP2 were applied to S-S BDEs.[50] A limited DFT study showed the BMK functional provided accuracy close to composite methods, with S-S BDEs of 64.5 kcal/mol for tBu-S-S-tBu, 63.9 kcal/mol for iPr-S-S-iPr, 63.8 kcal/mol for Et-S-S-Et, 62.9 kcal/mol for Me-S-S-Me, and 48.3 kcal/mol for Ph-S-S-Ph.[51] These values and trends roughly agree (within 2-5 kcal/mol) with our computational results of 59.39 kcal/mol, 59.69 kcal/mol, 59.48 kcal/mol, 58.04 kcal/mol, and 45.65 kcal/mol, respectively. Further, all previous computations also

find the S-S bond in Ph-S-S-Ph to be significantly weaker than its C-S bond and the S-S bonds of other disulfides. DFT with different functionals other than BMK gave a Se-Se BDE of 51.8 kcal/mol for Me-Se-Se-Me, which compares well with our value of 51.94 kcal/mol.[52,53]

Assessing dichalcogenide precursor reactivity from C-S BDEs. As shown in Table 1 and Figure 2, C-S bond energies progressively increase across the following series: Allyl-S-S-Allyl < Bn-S-S-Bn < tBu-S-S-tBu < iPr-S-S-iPr < Et-S-S-Et < Me-S-S-Me < Ph-S-S-Ph. In contrast, S-S bond energies remain roughly similar along most of the same series from Allyl-S-S-Allyl through Me-S-S-Me, but significantly drop (by about one third) for Ph-S-S-Ph. These trends greatly help understand our experimental observations. Both of the C-S bonds as well as the S-S bond must break in order to form nanocrystalline CdS. Because the strength of the S-S bond remains fairly constant among most disulfides, *the key factor that mainly determines the overall chemical reactivity of disulfide precursors is the strength of the C-S bond* (Figure 2a, Chart 1).

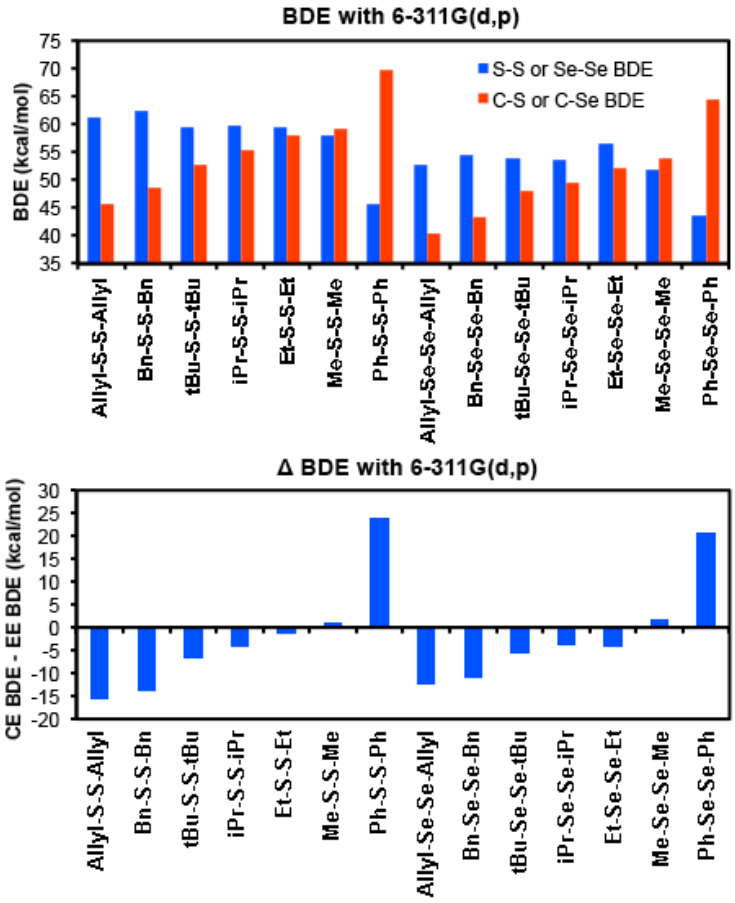

Figure 2. Bond dissociation (homolysis) energies (BDEs) calculated using density functional theory (DFT) with the Boese-Martin Kinetics (BMK) functional in GAMESS. Full computational results, including bond distances and dihedral angles are available in the Supporting Information.

Chart 1 (E = S or Se)

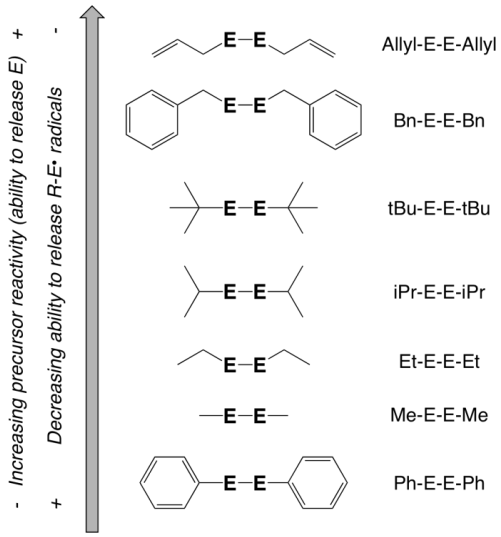

To illustrate, Allyl-S-S-Allyl and Bn-S-S-Bn have the weakest C-S bonds (45.71 kcal/mol and 48.50 kcal/mol, respectively) and are therefore the most reactive precursors in the series (Chart 1); they quickly (5-10 min) react with $Cd(oleate)_2$ to form large, non-quantum confined spherical CdS nanocrystals (Figure 2a, b). After 40 min, Allyl-S-S-Allyl and Bn-S-S-Bn lead to CdS particle sizes of 9.4 nm ± 1.3 nm and 4.2 nm ± 0.6 nm, respectively. In comparison, tBu-S-S-tBu and iPr-S-S-iPr have intermediate C-S bond strengths (52.81 kcal/mol and 55.45 kcal/mol, respectively) and are more mildly reactive; they react less quickly (5-40 min) with $Cd(oleate)_2$ to form small, quantum confined spherical CdS nanocrystals (Figure 2c, d). After 40 min, tBu-S-S-tBu and iPr-S-S-iPr lead to CdS particle sizes of 2.2 nm ± 0.2 nm and 1.8 nm ± 0.3 nm, respectively. For reference, the Bohr radius reported for CdS is between 2.5-3.0 nm.[54-56]

Further increasing the C-S bond strength and with it, decreasing chemical precursor reactivity, results in slower reaction and the selective formation of anisotropic structures. Et-S-S-Et and Me-S-S-Me have strong C-S bonds (58.13 kcal/mol and 59.03 kcal/mol, respectively) and are only weakly reactive; they react very slowly (20-40 min) and selectively with $Cd(oleate)_2$ to grow multipod and tetrapod structures (Figure 2e, f). After 40 min, Et-S-S-Et and Me-S-S-Me lead to CdS pods and tetrapods, respectively. For Et-S-S-Et, the average pod length and diameter are 10.3 ± 2.8 nm and 5.1 ± 0.6 nm, respectively. For Me-S-S-Me, the average pod length and diameter are 19.5 ± 2.9 nm and 5.5 ± 0.5 nm, respectively. At the end of the series and in stark contrast to all other dichalcogenides we tested, Ph-S-S-Ph has the strongest C-S bond (69.75 kcal/mol) and is unreactive (Chart 1); Ph-S-S-Ph alone (by itself) does not react with $Cd(oleate)_2$ under identical conditions to those used above for the other precursors (Figure 2g).

Compared to the rest of the dichalcogenide precursors we used, Ph-S-S-Ph is different not only because it contains the strongest C-S bond (69.75 kcal/mol), but also because it contains the weakest S-S bond (45.65 kcal/mol). On the contrary, for most of the other dichalcogenides in the series, the calculated S-S bond is either stronger than or as strong as the calculated C-S bonds (Table 1, Figure 2b). Examination of the highest occupied (HOMO) and lowest unoccupied (LUMO) molecular orbital diagrams of diphenyl disulfide (Ph-S-S-Ph) reveals a strong overlap between the π orbital on the chalcogen atoms and the π orbital of the adjacent phenyl carbon (Figure 3). This π-π overlap lends partial double bond character to the C-S bond, increasing the C-S bond strength (making it harder to break), and decreasing the C-S bond length (C-S 1.8085 Å for Ph-S-S-Ph vs. C-S 1.8494-1.8721 Å for other disulfides). Other dialkyl dichalcogenides, such as diethyl disulfide (Et-S-S-Et) do not possess such overlap (Figure 3). Based on these differences, we hypothesized that the formation of anisotropic particles may arise from the relative ease (and rate) of C-S vs. S-S bond breaking.

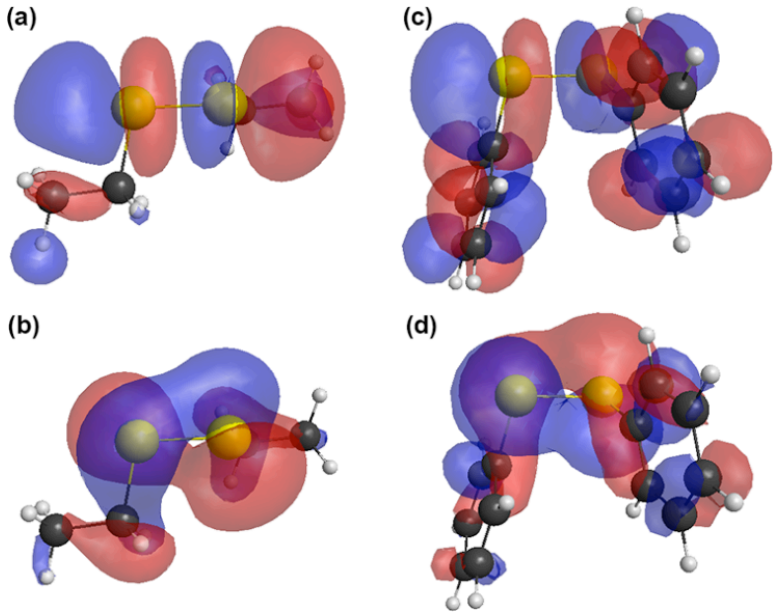

Figure 3. Lowest unoccupied (LUMO, top) and highest occupied (HOMO, bottom) molecular orbitals for Et-S-S-Et (a, b) and Ph-S-S-Ph (c, d) plotted with a contour value of 0.02. Calculated using density functional theory (DFT) with the Boese-Martin Kinetics

(BMK) functional in GAMESS. Full computational results, including bond distances and dihedral angles are available in the Supporting Information.

Understanding the formation of anisotropic structures: Molecular origin of nanoscale anisotropy. For Allyl-S-S-Allyl, Bn-S-S-Bn, tBu-S-S-tBu and iPr-S-S-iPr, the C-S bonds are weaker than the S-S bond by at least 5 kcal/mol or more (Table 1, Figure 2b); therefore, by the time the C-S bond breaks in these precursors, the S-S bond has already broken, resulting in the release of S equivalents that can proceed to react with $Cd(oleate)_2$ to form spheroidal (0D) nanocrystals. In contrast, for Et-S-S-Et and Me-S-S-Me the C-S and S-S bonds are very similar in energy (only ca. 1.35-0.99 kcal/mol apart) (Table 1, Figure 2b); therefore, the C-S and S-S bonds break with similar ease and at roughly similar or comparable rates, resulting in the concomitant release of both S, and R-S• radicals (Scheme 2). We expect thiol radicals of the form R-S• to act as excellent ligands due to their high affinity for soft cations and metal surfaces, for example by binding at so called "dangling bonds" or "surface traps".[57] The formation of radicals in these reactions is feasible given the high temperature (250°C), long time (40 min) and non-polar medium (octadecene and long chain surfactants) used here. Such harsh conditions are normally conducive to bond homolysis and radical chemistry. *In situ* generated R-S• radicals can act as capping ligands on the CdS surface, passivating the nanocrystals against further growth. Stabilizing and increasing the solution-phase lifetime of small, high-energy surface CdS nuclei could lead slower and more selective nanocrystal growth, resulting in the formation of anisotropic structures such as the pods and tetrapods observed with Et-S-S-Et and Me-S-S-Me (Figure 1e, f). In fact, in the presence of excess O_2, a naturally occuring diradical, $Cd(oleate)_2$ and NaHSe react very slowly and selectively to produce anisotropic CdSe structures (nanowires).[58]

The above situation reverses for the Ph-S-S-Ph precursor, where the calculated C-S bond is much stronger than the calculated S-S bond by 24.11 kcal/mol (Table 1, Figure 2b). This explains the apparent lack of reactivity of Ph-S-S-Ph: The S-S bond breaks very easily but the C-S bond does not, resulting in the facile release of R-S• radicals but not of S (Scheme 2). In fact, even though by itself it does not appear to react with $Cd(oleate)_2$, we reasoned that Ph-S-S-Ph should be extremely efficient at generating R-S• radicals. Because such thiol radicals can serve as surface-passivating ligands, we hypothesized that repeating CdS forming reactions using a mixture of the apparently 'unreactive' Ph-S-S-Ph with a reactive dichalcogenide such as tBu-S-S-tBu or iPr-S-S-iPr should induce the formation of anisotropic structures. As noted above, reacting $Cd(oleate)_2$ with tBu-S-S-tBu or iPr-S-S-iPr normally results in CdS dots (Figure 1b, c). However, mixing any of these two precursors with Ph-S-S-Ph could mimic the situation where a very slowly reacting (and selective) precursor such as Et-S-S-Et or Me-S-S-Me is used; more specifically, tBu-S-S-tBu or iPr-S-S-iPr would serve as a source of S, while Ph-S-S-Ph would serve as a source of surface-stabilizing R-S• radicals.

Inducing anisotropy: Testing the role of in situ generated thiol radicals. Figure 4 shows representative data confirming this prediction: While Ph-S-S-Ph alone is unreactive against $Cd(oleate)_2$, and Bn-S-S-Bn alone leads to quick formation of CdS nanocrystals (Figure 4a, b), a 1:1 mixture of Bn-S-S-Bn and Ph-S-S-Ph leads to the sole, highly-selective formation of CdS rods (Figure 4c). In turn, while tBu-S-S-tBu alone leads to quick CdS dot formation (Figure 4d), a 1:1 mixture of tBu-S-S-tBu and Ph-S-S-Ph leads to highly selective formation of CdS tetrapods (Figure 4e). Similarly, while iPr-S-S-iPr alone leads to quick CdS dot formation (Figure 4f), a 1:1 mixture of iPr-S-S-iPr and Ph-S-S-Ph leads to highly

selective formation of CdS tetrapods. These reactions cleanly and reproducibly produce anisotropic CdS structures (only rods or tetrapods), without the need for any of the widespread and commonly used size- and/or shape-selective purification protocols. In addition, pod branching depends on the ratio of precursors used (for example, the amount of tBu-S-S-tBu compared to that of Ph-S-S-Ph, see Supporting Information).

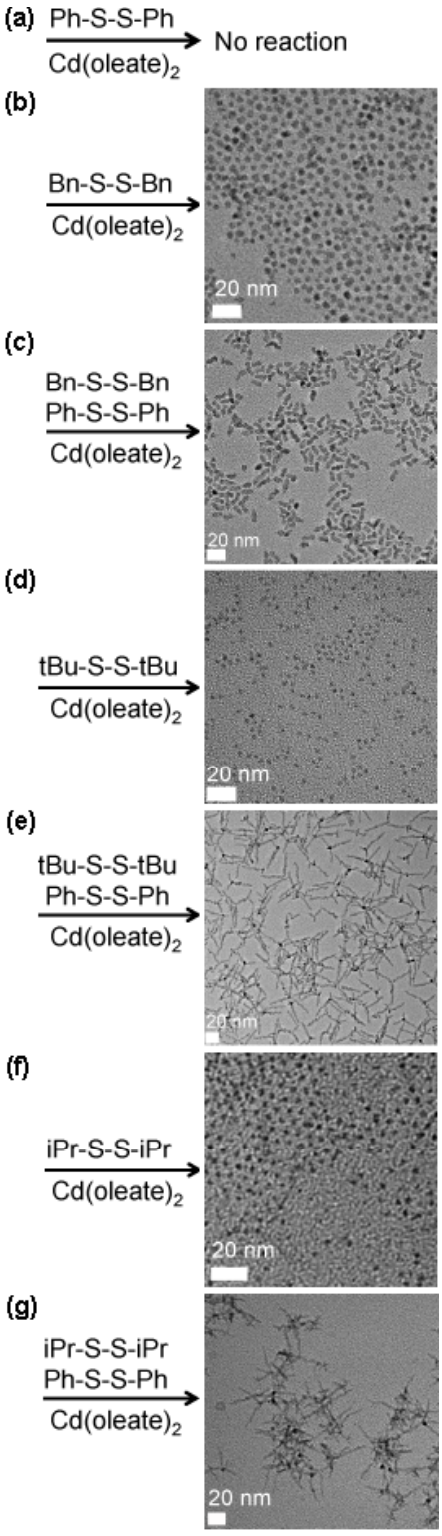

Figure 4. Under identical conditions (0.40 mol $Cd(oleate)_2$, 1.1 equiv. R-S-S-R, 20 equiv. oleic acid, 20 equiv. oleyl amine, 4.6 mL ODE, 250°C): Ph-S-S-Ph is unreactive (a); Bn-S-S-Bn produces CdS dots while a 1:1 mixture of Bn-S-S-Bn and Ph-S-S-Ph produces CdS rods (c); tBu-S-S-tBu produces CdS dots (d) while a 1:1 mixture of tBu-S-S-tBu and Ph-S-S-Ph

produces CdS tetrapods (e); iPr-S-S-iPr produces CdS dots (f) while a 1:1 mixture of iPr-S-S-iPr and Ph-S-S-Ph produces CdS tetrapods (g).

These results strongly support, and are consistent with our hypothesis above that *in situ* generated thiol radicals (R-S• radicals) serve as efficient surface-passivating ligands, increasing the lifetime of small CdS nuclei long enough to allow for slow (and selective) heterogeneous (epitaxial) growth of new CdS (pods). Dichalcogenide precursors with intermediate S-S and C-S bond strengths such as Et-S-S-Et and Me-S-S-Me are good at generating R-S• radicals, and they are also mild (slowly releasing) sources of S; therefore, these precursors are ideal for selective anisotropic growth (Figure 1e, f). With a much weaker S-S bond, the ability to generate R-S• radicals is even higher for Ph-S-S-Ph, but this precursor has a prohibitively strong C-S bond and is unable to serve as a source of S (Figure 1g and 4a); however, when mixed with other precursors that are good S sources such as Bn-S-S-Bn, tBu-S-S-tBu or iPr-S-S-iPr, Ph-S-S-Ph allows the generation of anisotropic structures such as rods and tetrapods where usually only dots would form (Figure 4c, e, g). In these mixed precursor experiments, the degree of anisotropy is a direct result of an exquisite interplay between the ability of Ph-S-S-Ph to give off surface-stabilizing R-S• radicals, and the chemical reactivity of a second precursor (namely, the latter's ability to give off S as measured by its relative C-S BDE). We are currently pursuing further mechanistic and spectroscopic studies that will help to better delineate the effect of *in-situ* generated thiol radicals on the rate of growth, shape selectivity, and overall outcome of colloidal nanocrystal preparations, and this will be the topic of a separate paper in the future.

Other effects of dichalcogenide reactivity: Understanding nucleation, growth and ripening. Our calculations and experimental observations also help understand the relative rates of nucleation, growth and ripening of CdS nanocrystals made with different

dichalcogenides (Figure 5). As judged from the position of the first 1S absorption peak (Figure 5a),[59-62] Bn-S-S-Bn (C-S BDE 48.50 kcal/mol) reacts with $Cd(oleate)_2$ to form larger CdS nanocrystals than tBu-S-S-tBu (C-S BDE 52.81 kcal/mol) or iPr-S-S-iPr (C-S BDE 55.45 kcal/mol). Interestingly, increasing the initial dichalcogenide concentration also results in an increase in the size of the CdS nanocrystals (iPr-S-S-iPr (×2) vs. iPr-S-S-iPr in Figure 5a). These observations suggest that *the rate of nanocrystal growth* (heterogeneous nucleation of new CdS material epitaxially on existing CdS particles)[63] *is directly dependent on dichalcogenide reactivity and concentration*. Dividing the CdS particle size (derived from the position of the 1S peak) by its size-specific absorption coefficient or "cross section" (ε) is proportional to the number of CdS particles present in the reaction at any given time (Figure 5b).[68-71] Interestingly, reaction of $Cd(oleate)_2$ with Bn-S-S-Bn (C-S BDE 48.50 kcal/mol) initially forms ca. twice as many initial nuclei as tBu-S-S-tBu (C-S BDE 52.81 kcal/mol) and *ca.* seven times as many nuclei as iPr-S-S-iPr (C-S BDE 55.45 kcal/mol) (short reaction times $\leqslant$ 5 min, Figure 5b). However, increasing the initial dichalcogenide concentration does not affect the number of initially formed CdS nuclei (iPr-S-S-iPr (×2) vs. iPr-S-S-iPr in Figure 5b). Therefore, *the rate of nanocrystal nucleation* (homogeneous nucleation of new CdS nuclei) *is extremely sensitive to, and directly dependent on, the reactivity of the dichalcogenide precursor used, but not its concentration*. Once the initial nucleation event has occurred, the change in the number of CdS particles over time (i.e., ripening) does not appear to be directly affected by precursor reactivity, but rather appears to be a simple consequence of the initial CdS particle size (Figure 5b).

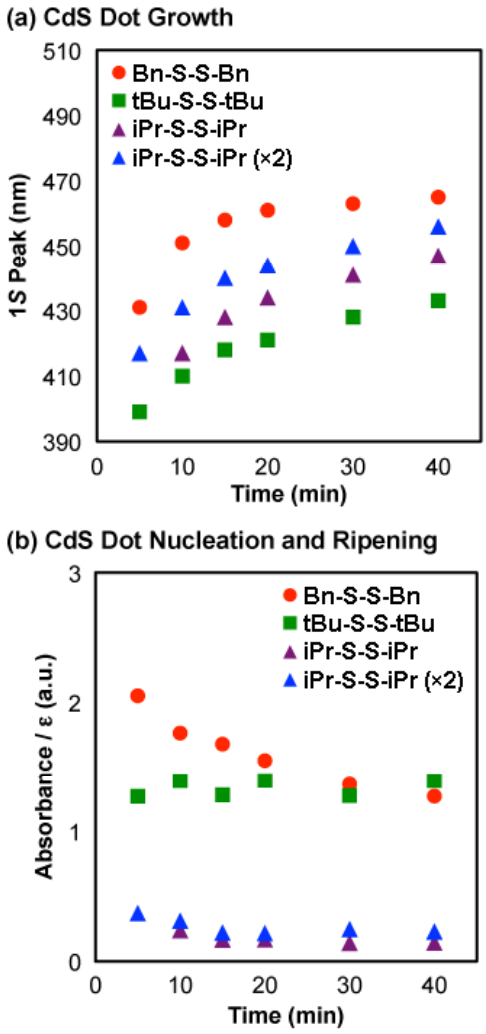

Figure 5. Time evolution of particle size (growth, a) and number of nuclei and ripening (b) of CdS nanocrystals produced with different dialkyl dichalcogenide precursors under similar reaction conditions (0.40 mol $Cd(oleate)_2$, 1.1 equiv. R-S-S-R, 20 equiv. oleic acid, 20 equiv. oleyl amine, 4.6 mL ODE, 250°C).

Comparing diselenide with disulfide precursors. The diselenide precursors reacted more quickly than the analogous disulfide precursors. We previously observed similar behavior in trialkylphosphine-chalcogenide precursors (R_3P=E, E = Se vs. S),[14-16] and we attribute this difference to the fact that Se forms weaker and longer (C-E and E-E) bonds compared to S (see Supporting Information available). Et-Se-Se-Et has weak C-Se bonds (52.01 kcal/mol) and reacts quickly with $Cd(oleate)_2$ to form CdSe quantum dots in < 2 min; these become non-quantum confined CdSe nanocrystals with a particle size of 6.6 nm ± 0.6

nm after 10 min (Figure 6a). For reference, the Bohr radius reported for CdSe is *ca.* 5.4 nm.[42] Me-Se-Se-Me has stronger C-Se bonds (53.76 kcal/mol) and reacts more slowly and selectively with $Cd(oleate)_2$ to form CdSe multipods; these show significant clustering after 5 min (Figure 6b). Ph-Se-Se-Ph has even stronger C-Se bonds (64.44 kcal/mol) and barely reacts with $Cd(oleate)_2$ to form very small CdSe quantum dots (Figure 6c). We attribute the difference between Ph-S-S-Ph (unreactive) and Ph-Se-Se-Ph (marginally reactive) to the difference in C-E bond dissociation energies between these two precursors (C-S BDE 69.75 kcal/mol in Ph-S-S-Ph vs. C-Se BDE 64.44 kcal/mol in Ph-Se-Se-Ph) (Table 1). Thus, although more reactive, the diselenide (R-Se-Se-R) precursors show similar reactivity patterns as those observed for the disulfide (R-S-S-R) precursors above.

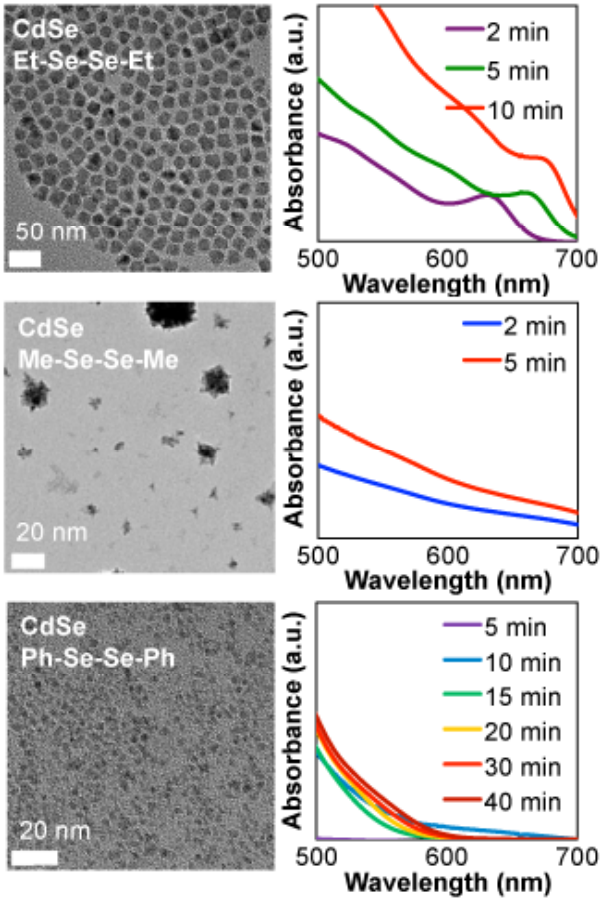

Figure 6. Representative TEM images (left panel) and time evolution of UV-Vis absorption spectra (right panel) of CdS nanocrystals obtained with (a) diethyl (10 min), (b) dimethyl (5 min), and (c) diphenyl disulfide (40 min) precursors under identical conditions (0.40 mol $Cd(oleate)_2$, 1.1 equiv. R-Se-Se-R, 20 equiv. oleic acid, 20 equiv. oleylamine, 4.6 mL ODE, 250°C).

Conclusions

By studying a variety of commercially available dichalcogenides and the outcome of their solution-phase reaction with a cadmium-oleate complex under identical conditions, we have demonstrated that the formation and degree of anisotropy of different nanocrystalline products can be traced back to the precise molecular structure, bonding energetics, and chemical reactivity of the different dichalcogenides used. Using DFT, we showed that the main factor that determines overall dichalcogenide precursor reactivity is the carbon-chalcogen (C-S or C-Se) bond dissociation energy, while the chalcogen-chalcogen (S-S or Se-Se) bond dissociation energy remains more or less constant across a series of dichalcogenides (disulfides or diselenides). The only exception to this trend are diphenyl dichalcogenides, which exhibit the weakest chalcogen-chalcogen bond and the strongest carbon-chalcogen bond due to strong π orbital interaction between the first carbon atom in the phenyl ring and the adjacent chalcogen atom. The presence of this strong C-S bonding interaction causes Ph-S-S-Ph to appear unreactive when used alone. Conversely, Allyl-S-S-Allyl has the weakest C-S bond, and reacts quickly to produce large aggregated CdS nanocrystals. Similar trends in bond dissociation energies and reactivity hold for the diselenide precursors, although their longer and weaker bonds lead to increased reactivity and more aggregated particles compared to disulfide precursors.

To understand the formation of anisotropic structures from disulfides containing roughly equal C-S and S-S bond strengths (Et-S-S-Et or Me-S-S-Me), we carried out

reactions employing 1:1 mixtures of a thiol radical source (Ph-S-S-Ph) and a sulfur monomer source (Bn-S-S-Bn, tBu-S-S-tBu, or iPr-S-S-iPr). Ph-S-S-Ph by itself yielded no nanocrystalline products and the sulfur sources alone yielded only spherical nanocrystals. However the mixed precursor experiments resulted in the exclusive formation of anisotropic structures (rods or tetrapods). Our present hypothesis is that the disulfide bond of Ph-S-S-Ph homolyzes to produce PhS• radicals which passivate and stabilize small zinc blende CdS nuclei. The cadmium and the second sulfur (Bn-S-S-Bn, tBu-S-S-tBu, or iPr-S-S-iPr) precursors then slowly react to selectively grow wurtzite arms on the {111} facets of the zinc blende cores. Our computations shed light on the experimentally observed rates of nucleation, growth and ripening of CdS nanocrystals. The rates of CdS nanocrystal nucleation and growth are directly dependent on dichalcogenide chemical reactivity, or inversely proportional to C-S bond strength. Increasing the initial dichalcogenide concentration increases CdS nanocrystal size, but does not affect the number of CdS particles already present after the initial nucleation stage. This implies that the observed sizes and morphology are not a function of precursor concentration, but only its characteristic reactivity. By applying our understanding of the chemistry of molecular precursors, we may begin to rationalize and predict desirable nanocrystalline properties such as morphology, composition and optoelectronic properties. This “bottom-up” approach to controllable and predictable nanocrystal synthesis allows for the preparation of a diverse array of morphologies based on fundamental, tangible and measurable molecular properties such as bond energies. We believe this and similar efforts will lead to the reliable syntheses of colloidal nanomaterials for customized applications.

Experimental Section

Materials. Cadmium oxide (CdO, 99.998%) and oleic acid (90%) were purchased from Alfa Aesar; diallyl disulfide (Allyl-S-S-Allyl, 80%), dibenzyl disulfide (Bn-S-S-Bn, 98%), ditertiarybutyl disulfide (tBu-S-S-tBu, 97%), diisopropyl disulfide (iPr-S-S-iPr, 96%), diethyl disulfide (Et-S-S-Et, 99%), dimethyl disulfide (Me-S-S-Me, 99%), and dimethyl diselenide (Me-Se-Se-Me, 96%) from Sigma-Aldrich; diphenyl disulfide (Ph-S-S-Ph, 99%), 1-octadecene (ODE, 90%), and oleylamine (80-90%) from Acros; diethyl diselenide (Et-Se-Se-Et) and diphenyl diselenide (Ph-Se-Se-Ph, 98%) from Strem.

Synthesis. Dichalcogenide addition solution. Inside a glove box filled with dry N_2, the dichalcogenide precursor (0.42 mmol) (61.0 mg Allyl-S-S-Allyl, 104 mg Bn-S-S-Bn, 75.0 mg tBu-S-S-tBu, 63.1 mg iPr-S-S-iPr, 51.0 mg Et-S-S-Et, 39.6 mg Me-S-S-Me, 91.0 mg Et-Se-Se-Et, 79.0 mg Me-Se-Se-Me, or 131 mg Ph-Se-Se-Ph) was thoroughly dissolved in ODE (1.00 g, 1.27 mL) to afford a homogeneous mixture. Cadmium chalcogenide particles. Inside a three-neck-flask, CdO (51.2 mg, 0.40 mmol), oleic acid (2.24 g, 8.00 mmol), oleylamine (2.14 g, 8.00 mmol) and ODE (2.62 g, 3.32 mL) were degassed under vacuum at 80°C for 30 min, refilled with Ar, and heated to 180°C for 10 min until the mixture became a homogeneous, optically clear solution. The solution was cooled to 80°C, degassed under vacuum at 80°C for 30 min, refilled with Ar, and heated to 250°C. After 5 min, the dichalcogenide addition solution (above) was quickly injected. Aliquots (0.10 mL) were taken at different times, added to the same amount of toluene (3 mL) every time, and analyzed by UV-Vis absorption and PL. After 40 min (disulfides) or 5-40 min (diselenides, see below), the mixture was allowed to cool to room temperature (R.T.). Nanocrystals were

isolated and purified twice by washing with a 1:2 v/v acetone-methanol mixture and centrifugation at 4900 rpm for 5 min.

Optical Characterization. Absorption spectra were measured with a photodiode array Agilent 8453 UV-Vis spectrophotometer. Steady-state PL spectra were measured with a Horiba-Jobin Yvon Nanolog scanning spectrofluorometer equipped with a photomultiplier detector.

Structural Characterization. Powder X-ray diffraction (XRD) was measured using Cu Kα radiation on a Scintag XDS-2000 diffractometer. Transmission Electron Microscopy (TEM) was conducted on carbon-coated copper grids using a FEI Technai G2 F20 field emission scanning transmission electron microscope (STEM) at 200 kV (point-to-point resolution <0.25 nm, line-to-line resolution <0.10 nm). Particle dimensions were measured manually and/or with ImageJ for >50-100 particles. Averages are reported ± one standard deviation.

Computational Methods. Bond dissociation energies (BDEs) were calculated using GAMESS[64,65] at the DFT[66] level of theory with the BMK (Boese-Martin Kinetics) functional,[67] which has been shown to provide accuracy near that of high-precision complete basis set (CBS) methods.[68,69] Geometries were optimized using the 6-31G(d) basis set[70] followed by single point calculations with the 6-311G(d,p) basis set[77] to determine BDEs.[72] Frequency calculations were performed to obtain zero point energies and enthalpies at 273 K and to ensure that the Hessian matrices of the optimized geometries contained no negative eigenvalues.[73]

Acknowledgement

J. V. thanks Iowa State University for startup funds. S. R. A. thanks ISU's Graduate College for a George Washington Carver Doctoral Fellowship. S. R. A. and J. V. thank Hua-Jun Fan, Jakoah Brgoch, Theresa Windus and Mark Gordon for helpful discussions.

References

[1] Norako, M. E.; Franzman, M. A.; Brutchey, R. L. *Chem. Mater.* **2009**, *21*, 4299–4304.

[2] Norako, M. E.; Brutchey, R. L. *Chem. Mater.* **2010**, *22*, 1613–1615.

[3] Norako, M. E.; Greaney, M. J.; Brutchey, R. L. *J. Am. Chem. Soc.* **2012**, *134*, 23–26.

[4] Franzman, M. A.; Brutchey, R. L. *Chem. Mater.* **2009**, *21*, 1790–1792.

[5] Li, W.; Shavel, A.; Guzman, R.; Rubio-Garcia, J.; Flox, C.; Fan, J.; Cadavid, D.; Ibáñez, M.; Arbiol, J.; Morante, J. R. et al. *Chem. Commun.* **2011**, *47*, 10332–10334.

[6] Franzman, M. A.; Schlenker, C. W.; Thompson, M. E.; Brutchey, R. L. *J. Am. Chem. Soc.* **2010**, *132*, 4060–4061.

[7] Webber, D. H.; Brutchey, R. L. *Inorg. Chem.* **2011**, *50*, 723–725.

[8] Buckley, J. J.; Rabuffetti, F. A.; Hinton, H. L.; Brutchey, R. L. *Chem. Mater.* **2012**, *24*, 3514−3516.

[9] Webber, D. H.; Brutchey, R. L. *Chem. Commun.* **2009**, 5701–5703.

[10] Kang, S.-K.; Jia, L.; Li, X.; Yin, Y.; Li, L.; Guo, Y.-G.; Mu, J. *Colloids Surf. A: Phys. Eng. Aspects* **2012**, *406*, 1–5.

[11] Wang, J.-J.; Xue, D.-J.; Guo, Y.-G.; Hu, J.-S.; Wan, L.-J. *J. Am. Chem. Soc.* **2011**, *133*, 18558–18561.

[12] Wang, J.-J.; Wang, Y.-Q.; Cao, F.-F.; Guo, G.-Y.; Wan, L.-J. *J. Am. Chem. Soc.* **2010**, *132*, 12218–12221.

[13] Schlecht, S.; Budde, M.; Kienle, L. *Inorg. Chem.* **2002**, *41*, 6001–6005.

[14] Ruberu, T. P. A.; Vela, J. *ACS Nano* **2011**, *5*, 5775–5784.

[15] Alemseghed, M. G.; Ruberu, T. P. A.; Vela, J. *Chem. Mater.* **2011**, *23*, 3571–3579.

[16] Ruberu, T. P. A.; Albright, H. R.; Callis, B.; Ward, B.; Cisneros, J.; Fan, H.-J.; Vela, J. *ACS Nano* **2012**, *6*, 5348–5359.

[17] Ko, W. Y. L.; Bagaria, H. G.; Asokan, S.; Lina, K. J.; Wong, M. S. *J. Mater. Chem.* **2010**, *20*, 2474–2478.

[18] Wang, W.; Geng, Y.; Qian, Y.; Ji, M.; Liu, X. *Adv. Mater.* **1998**, *10*, 1479–1481.

[19] Xi, L.; Chua, K. H.; Zhao, Y.; Zhang, J.; Xiong, Q.; Lam, Y. M. *RSC Advances* **2012**, *2*, 5243–5253.

[20] Shen, H.; Wang, H.; Chen, X.; Niu, J. Z.; Xu, W.; Li, X. M.; Jiang, X.-D.; Du, Z.; Li, L. S. *Chem. Mater.* **2010**, *22*, 4756–4761.

[21] Pang, Q.; Zhao, L.; Cai, Y.; Nguyen, D. P.; Regnault, N.; Wang, N.; Yang, S.; Ge, W.; Ferreira, R.; Bastard, G. et al. *Chem. Mater.* **2005**, *17*, 5263–5267.

[22] Yang, J.; Xue, C.; Yu, S. H.; Zeng, J. H.; Qian, Y. T. *Angew. Chem. Int. Ed.* **2002**, *41*, 4697-4700.

[23] Govan, J. E.; Jan, E.; Qurejeta, A.; Kotov, N. A.; Gun'ko, Y. K. *Chem. Commun.* **2010**, *46*, 6072–6074.

[24] Asokan, S.; Krueger, K. M.; Colvin, V. L.; Wong, M. S. *Small* **2007**, *3*, 1164−1169.

[25] Manna, L.; Scher, E. C.; Alivisatos, A. P. *J. Am. Chem. Soc.* **2000**, *122*, 12700−12706.

[26] Wang, F.; Buhro, W. E. *J. Am. Chem. Soc.* **2012**, *134*, 5369−5380.

[27] Liu, H.; Tao, H.; Yang, T.; Kong, L.; Qin, D.; Chen, J. *Nanotechnology* **2011**, *22*, 045604.

[28] Huang, J.; Kovalenko, M. V.; Talapin, D. V. *J. Am. Chem. Soc.* **2010**, *132*, 15866–15868.

[29] Fiore, A.; Mastria, R.; Lupo, M. G.; Lanzani, G.; Giannini, C.; Carlino, E.; Morello, G.; De Giorgi, M.; Li, Y.; Cingolani, R.; Manna, L. *J. Am. Chem. Soc.* **2009**, *131*, 2274−2282.

[30] Talapin, D. V.; Nelson, J. H.; Shevchenko, E. V.; Aloni, S.; Sadtler, B.; Alivisatos, A. P. *Nano Lett.* **2007**, *7*, 2951–2959.

[31] Peng, X.; Manna, L.; Yang, W.; Wickham, J.; Scher, E.; Kadavanich, A.; Alivisatos, A. P. *Nature* **2000**, *404*, 59–61.

[32] Peng, Z. A.; Peng, X. *J. Am. Chem. Soc.* **2002**, *124*, 3343−3353.

[33] Xie, R.; Kolb, U.; Basche, T. *Small* **2006**, *2*, 1454−1457.

[34] Lim, J.; Bae, W. K.; Park, K. U.; Zur Borg, L.; Zentel, R.; Lee, S.; Char, K. *Chem. Mater.* **2013**, *25*, 1443-1449.

[35] Zhang, W.; Jin, C.; Yang, Y.; Zhong, X. *Inorg. Chem.* **2012**, *51*, 531−535.

[36] Lutich, A. A.; Mauser, C.; Da Como, E.; Huang, J.; Vaneski, A.; Talapin, D. V.; Rogach, A. L.; Feldmann, J. *Nano Lett.* **2010**, *10*, 4646–4650.

[37] Choi, C. L.; Li, H.; Olson, A. C. K.; Jain, P. K.; Sivasankar, S.; Alivisatos, A. P. *Nano Lett.* **2011**, *11*, 2358–2362.

[38] Lee, D. C.; Robel, I.; Pietryga, J. M.; Klimov, V. I. *J. Am. Chem. Soc.* **2010**, *132*, 9960–9962.

[39] Bealing, C. R.; Baumgardner, W. J.; Choi, J. J.; Hanrath, T.; Hennig, R. G. *ACS Nano* **2012**, *6*, 2118–2127.

[40] Kumar, S.; Nann, T. *Small* **2006**, *2*, 316–329.

[41] Manna, L.; Milliron, D. J.; Meisel, A.; Scher, E. C.; Alivisatos, A. P. *Nature Mater.* **2003**, *2*, 382–385.

[42] Nourbakhsh, S.; Liao, C. L.; Ng, Y. G. *J. Chem. Phys.* **1990**, *92*, 6587–6593.

[43] McMillen, D. F.; Golden, D. M. Ann. *Rev. Phys. Chem.* **1982**, *33*, 493–532.

[44] Luo, Y.-R. *Comprehensive Handbook of Chemical Bond Energies*; CRC Press: Boca Raton, FL: **2007**; pp. 425–454.

[45] Benson, S. W. *Chem. Rev.* **1978**, *78*, 23–35.

[46] Płaza, S.; Gruziński, R. *Wear* **1996**, *194*, 212–218.

[47] Mortimer, C. T.; Waterhouse, J. *J. Chem. Thermodyn.* **1980**, *12*, 961–965.

[48] Arshadi, M. R.; Shabrang, M. *J. Chem. Soc. Perkin Trans. 2* **1973**, *2*, 1732–1734.

[49] Benassi, R.; Taddei, F. *J. Comput. Chem.* **2000**, *21*, 1405–1418.

[50] Zou, L.-F.; Fu, Y.; Shen, K.; Guo, Q.-X. *THEOCHEM* **2007**, *807*, 87–92.

[51] Zou, L.-F.; Shen, K.; Fu, Y.; Guo, Q.-X. *J. Phys. Org. Chem*. **2007**, *20*, 754–763.

[52] Heverly-Coulson, G. S.; Boyd, R. J. *J. Phys. Chem. A* **2011**, *115*, 4827–4831.

[53] Gámez, J. A.; Yáñez, M. *J. Chem. Theory Comp.* **2010**, *6*, 3102–3112.

[54] Yoffe, A. D. *Adv. Phys.* **2002**, *51*, 799–890.

[55] Wang, Y.; Herron, N. *J. Phys. Chem.* **1991**, *95*, 525–532.

[56] Fonoberov, V. A.; Pokatilov, E. P.; Mateevici, A. *Phys. Rev. B* **2002**, *66*, 085310.

[57] Smith, A. M.; Nie, S. *Acc. Chem. Res.* **2010**, *43*, 190−200.

[58] Doll, J. D.; Hu, B.; Papadimitrakopoulos, F. *Chem. Mater.* **2012**, *24*, 4043−4050.

[59] Yu, W. W.; Qu, L.; Guo, W.; Peng, X. *Chem. Mater.* **2003**, *15*, 2854–2860; 2004, 16, 560.

[60] Jasieniak, J.; Smith, L.; van Embden, J.; Mulvaney, P.; Califano, M. *J. Phys. Chem. C* **2009**, *113*, 19468–19474.

[61] Capek, R. K.; Moreels, I.; Lambert, K.; De Muynck, D.; Zhao, Q.; Van Tomme, A.; Vanhaecke, F.; Hens, Z. *J. Phys. Chem. C* **2010**, *114*, 6371–6376.

[62] Leatherdale, C. A.; Woo, W.-K.; Mikulec, F. V.; Bawendi, M. G. *J. Phys. Chem. B* **2002**, *106*, 7619–7622.

[63] Guo, Y.; Marchuk, K.; Sampat, S.; Abraham, R.; Fang, N.; Malko, A.; Vela, J. *J. Phys. Chem. C* **2012**, *116*, 2791–2800.

[64] Schmidt, M. W.; Baldridge, K. K.; Boatz, J. A.; Elbert, S. T.; Gordon, M. S.; Jensen, J. S.; Koseki, S.; Matsunaga, N.; Nguyen, K. A.; Su, S. et al. *J. Comput. Chem.* **1993**, *14*, 1347–1363.

[65] Gordon, M. S.; Schmidt, M. W. Advances in Electronic Structure Theory: GAMESS a Decade Later. *In Theory and Applications of Computational Chemistry: The First Forty Years*; Dykstra, C. E., Frenking, G., Kim, K. S., Scuseria, G. E., Eds.; Elsevier Science: Amsterdam, **2005**; p 1167.

[66] Hehre, W. J.; Ditchfield, R.; Pople, J. A. *J. Chem. Phys.* **1972**, *56*, 2257–2261.

[67] Boese, A. D.; Martin, J. M. L. Development of Density Functionals for Thermochemical Kinetics. *J. Chem. Phys.* **2004**, *121*, 3405–3416.

[68] Denk, M. K. *Eur. J. Inorg. Chem.* **2009**, 1358–1368.

[69] Bode, B. M.; Gordon, M. S. *J. Mol. Graphics Model.* **1998**, *16*, 133.

[70] Ditchfield, R.; Hehre, W. J.; Pople, J. A. *J. Chem. Phys.* **1971**, *54*, 724 − 728.

[71] Krishnan, R.; Binkley, J. S.; Seeger, R.; Pople, J. A. *J. Chem. Phys.* **1980**, *72*, 650 – 654.

[72] Mitin, A. V.; Baker, J.; Pulay, P. *J. Chem. Phys.* **2003**, *118*, 7775–7782.

[73] Roothaan, C. C. J. *Rev. Mod. Phys.* **1951**, *23*, 69–89.

Supporting Information

Table S1. Results of DFT calculations on dialkyl dichalcogenide bond energies and structural parameters.

Precursor(s) R-E-E-R	C-E BDE (kcal/mol)	E-E BDE (kcal/mol)	(C-E)-(E-E) (kcal/mol)	C-E bond length (Å)	E-E bond length (Å)	C-E-E-C dihedral angle (deg)
Disulfides (R-S-S-R)						
Allyl-S-S-Allyl	45.71	61.33	-15.62	1.8721	2.0926	89.28
Bn-S-S-Bn	48.50	62.45	-13.94	1.8732	2.0925	87.65
tBu-S-S-tBu	52.81	59.39	-6.59	1.8900	2.0961	110.88
iPr-S-S-iPr	55.45	59.69	-4.24	1.8744	2.0968	111.51
Et-S-S-Et	58.13	59.48	-1.35	1.8606	2.0912	86.37
Me-S-S-Me	59.03	58.04	0.99	1.8494	2.0930	84.93
Ph-S-S-Ph	69.75	45.65	24.11	1.8085	2.1144	83.15
Diselenides (R-Se-Se-R)						
Allyl-Se-Se-Allyl	40.37	52.82	-12.45	1.9897	2.3359	91.24
Bn-Se-Se-Bn	43.26	54.43	-11.16	1.9878	2.3346	84.67
tBu-Se-Se-tBu	48.14	53.96	-5.83	1.9891	2.3380	107.52
iPr-Se-Se-iPr	49.57	53.49	-3.92	2.0073	2.3364	107.02
Et-Se-Se-Et	52.01	56.41	-4.40	1.9762	2.3341	88.49
Me-Se-Se-Me	53.76	51.94	1.82	1.9641	2.3351	86.82
Ph-Se-Se-Ph	64.44	43.63	20.80	1.9238	2.3582	82.74

CHAPTER 6

GENERAL CONCLUSIONS

By developing a fine balance between homogeneous and heterogeneous nucleation, this work improved the synthesis, characterization and application of core/shell, nanorod, and tetrapod nanoarchitectures.

We carried out a thorough investigation of thick-shelled CdSe/nCdS($n \geq 10$) nanocrystal synthesis using short and accessible 15 min wait times between SILAR injections. We explored added amine, amine type, CdSe core, and precursor concentration, Cd:S ratio, annealing time, and injection-rate effects on the synthesis of these materials. Successful thick-shell growth presents unique challenges compared with core/shells with thin shells. We found that added secondary amine and low-core and precursor concentrations introduced at slow injection rates result in core/shells with desired shell thickness and particle size. The presented method works well for small CdSe (1.9 nm) and large CdSe (4.7 nm) cores. Under 400 nm laser excitation, core/shells derived from small CdSe (1.9 nm) cores have longer PL lifetimes and more pronounced blinking at the single-particle level compared with those derived from large CdSe (4.7 nm) cores. This optical behavior agrees well with recently published theoretical aspects and experimental spectroscopy.

Having a reliable, highly reproducible method for the synthesis of non-blinking, giant CdSe/CdS nanocrystals at hand, we further studied their application using total internal reflection fluorescence microscopy and stimulated emission depletion microscopy. Attaching non-blinking QDs to microtubles, we studied the gliding and self-rotating of microtubules under the presence of motor protein-kinesin. STED is an imaging method capable of providing data that are below the diffraction limit. Compared with organic flurophores,

core/shell quantum dots are ideal targets for this type of technique because of their remarkable photostability. When time-gated, this technique provides images of non-blinking CdSe/CdS quantum dots (average size 13±2 nm) at 40±10 nm spatial resolution.

Growth of a CdS or ZnS shell greatly enhances the near-infrared (NIR) photoluminescence intensity and improves the NIR photoluminescence stability of Ge nanocrystals. In general, all Ge/II-VI heterostrucutures showed one-to-three orders of magnitude more intense NIR emission compared to the original Ge cores. All the Ge/CdS and Ge/ZnS nanocrystals retained their NIR photoluminescence after several months. Ge/4.9CdS showed the highest NIR quantum yield and longest PL lifetime. Although there is clearly room for improvement, the achieved PL level is already three thousand times brighter than the most emissive Ge cores we were able to make using literature procedures. Additional CdS shell growth caused a decrease in quantum yield, possibly due to the introduction of defects due to strain effects. Ge/II-VI nanocrystals easily transfer from organic to aqueous phase upon thiol ligand exchange. We expect that these results will extend the arsenal of quantum dot fluorophores available, particularly near-IR active quantum dots, for fundamental optoelectronic studies as well as for biological imaging and tracking, telecommunications, and energy conversion applications.

In addition to core/shell heterostructures, we also discussed the formation of anisotropic nanorods and tetrapods via dichalcogenide precursors. By studying a variety of commercially available dichalcogenides and the outcome of their solution-phase reaction with a cadmium oleate complex under identical conditions, we demonstrated that the formation and degree of anisotropy of different nano-crystalline products can be traced back to the precise molecular structure, bonding energetics, and chemical reactivity of the different

dichalcogenides used. We attributed the formation of anisotropic nanorods and tetrapods to different bond dissociation energies of the different dichalcogenide precursors. If RS• radicals were produced, these thiol radicals can passivate and stabilize small zinc blende CdS nuclei, then slowly and selectively grow wurtzite arms on the {111} facets of the initial zinc blende cores. Our computations shed light on the experimentally observed rates of nucleation, growth, and ripening of CdS nanocrystals. The rates of CdS nanocrystal nucleation and growth are directly dependent on dichalcogenide reactivity. By applying our understanding of the chemistry of the molecular precursors, we may begin to rationalize and predict desirable nanoparticle properties. This "bottom-up" approach to controllable and predictable nanocrystal synthesis allows for the preparation of a diverse array of morphologies based on fundamental, tangible, and measurable molecular properties such as bond energies. We believe this and similar efforts will lead to the reliable syntheses of colloidal nanomaterials for customized applications.